Large Magneto-functional responses in transition metal-based alloys: Protocol dependence across martensitic phase transition

A thesis submitted for the award of the degree of

Doctor of Philosophy (Sciences)

in

Physics (Experimental)

by

Saheli Samanta

Department of Physics

University of Calcutta

Kolkata, India

January, 2023

Dedicated to Ma Santoshi and my Parents …

"This is my belief: that through difficulties

and problems God gives us the opportunity to grow.

So when your hopes and dreams and goals are dashed, search among the wreckage,

you may find a golden opportunity hidden in the ruins"

- Dr. A.P.J. Abdul Kalam

Acknowledgement:

It has been five memorable years of my journey here at S. N. Bose National Centre for Basic Sciences (SNBNCBS), and thesis submission is knocking at my door. I would like to seize this opportunity to acknowledge and thank the people without whom this thesis would not have been possible.

First and foremost, I would like to express my deepest gratitude to my thesis supervisor *Prof. Kalyan Mandal* for his heartening guidance, continuous motivation, and most importantly invaluable instructions for my research career. His encouragement through the fluctuation during these years was the major impetus for me to forge ahead. I've truly learnt from him the basic knowledge of research and designing a proper plan in a scientific approach. In the last three years, he has enriched me with self-confidence and optimism that has done wonders in my research field.

I owe much to my teachers in the early of my study in science. At first, I am privileged to have the best science teacher like my father (*Gopinath Samanta*) during my school days who not only ignited my interest in science but also taught me the basic morality and ethics of life. I remember one thing that he taught me "*charity begins at home*." Since my earlier, I am close to my Maa who deserves the best teacher of my life. Particularly she taught me the rest of the other subjects up to madhyamik. I am also thankful to my Life science teacher *Madhu Babu* (*Madhu Mahesh*) who inspired me to be a true researcher. I endow my respect to my favorite Gouri Mam (Gauri Ray) who vividly guided and loved me during my teenage.

I would like to thank to my college Madam *Putul* mam (Prof. *Putul Samanta*) for her student-friendly behaviour. My heartiest respect to Prof. *Mrityunjay Das*, Dr. *Avijit Kr. Gupta*, Dr. *Bidyut Samanta*, and Prof. *Paresh Chandra Jana* to have such good teachers in my physics academic journey.

I am grateful to S.N Bose National Centre for Basic Sciences (Kolkata) for gifting me such a wonderful greenish campus and effective instrumental facilities. I endow my respect to Prof. *Arup Kumar Raychaudhuri* (AKR) who first taught me how to build a device using basic physics and thoroughly addressed my queries and thereby

introduced me to a systematic approach for seeking an answer during my Technical Research Centre (TRC) project. I extremely grateful to Dr. *Barnali Ghosh*, Dr. *Manik Pradhan*, Dr. *Ranjit Biswas*, and Dr. *Soumen Mandal* as well. During my TRC journey, initially, I am thankful to all the TRC members including *Sayani, Snehamoyee, Ayan Da, Lopa* and specially *Soumitra Da* who has always shared his knowledge, motivated me to do better, and helped me professionally to working place.

I wish to express special gratitude to my senior *Subrata Da* who taught me research ethics from the beginning of my research journey. His contribution on the sample preparation, data analysis, and few measurement procedures was very supportive to me. Specially, he enlightened me a trick for finding of new system related to my thesis work. He behaves to me as a genuine senior researcher.

One of my batchmate *Sudipta* taught me transport properties measurement and trigger me to do better in the scientific community. A scientific discussion session with *Jayee Di* and *Sridhar* boosts me up. Without them, I could not finish my research work.

I must thank to other labmates of magnetism laboratories: *Rupali Di, Souvanik Da, Mahebub Da, Keshab Da*, *Indranil Da*, *Dipika Di, Dipanjan Da, Priyanka Di, Anupam, Swarnali, Sohom, Ishita,* and *Sourav* for sharing a healthy lab environment. They are very much pretty for their research work.

I would like to acknowledge all the technical stuff including *Urmi Di, Jay Da, Debarghya da, and Sourav Da* for their friendliness behaviour during experimental measurements.

Apart from my lab mates, I have spent a delightful moment at S. N. Bose Institute with some singers-cum-researchers *Sarowar Da, Sovon Da, Suchismita Di, Parusattam, Kaustab, Riju, Sayan* and *Kankona*.

Finally, I express my deepest gratitude to my parents. All my achievements belong to my Maa and Bapi who had to go through a lot of sacrifices to make me and give me moral supports, caring and love. A warm thanks deserve to my friend cum dada *Victor Da* to be available always, particularly in my wax and wane moment. At last, I want to give my gratitude to my almighty Goddess for blessing me in the ups and downs of my life all through this adventure journey.

List of Abbreviations:

A_f	: Austenite finish temperature
AFM	: Antiferromagnetic
AMR	: anisotropy magnetoresistance
A_S	: Austenite start temperature
DSC	: Differential Scanning Calorimetry
DOS	: Density of state
ΔH	: Magnetic field change
ΔS_M	: Isothermal magnetic entropy change
ΔT_{ad}	: Adiabatic temperature change
ΔT_{hys}	: Thermal hysteresis
ΔT_{int}	: Transformation interval
EAF	: Electric-arc-furnace
EB	: Exchange Bias
EDAX	: Energy dispersive X-ray analysis
EDS	: Energy dispersive spectroscopy
ETO	: Electrical transport option
FC	: Field-cold
FESEM	: Field emission scanning electron microscope
FM	: Ferromagnetic
FIRMT	: Field induced-reverse martensitic transformation
FOMST	: First-order-magnetostructural transformation
FOPT	: First-order phase transition
FWHM	: Full width at half maxima
G_A	: Gibbs free energy of the austenite phase
G_M	: Gibbs free energy of the austenite phase
H_C	: Coercivity
H_E	: Exchange bias field

HL	: Hysteresis loss
IMCE	: Inverse magnetocaloric effect
MCE	: Magnetocaloric effect
M_f	: Martensitic finish temperature
MR	: Magnetoresistance
MRAM	: Magnetoresistive random access memory
M_S	: Martensitic start temperature
MSME	: Magnetic shape memory effect
PPMS	: Physical Property Measurement Systems
RCP	: Relative Cooling power
RE	: Rare-earth
RT	: Room-temperature
SEM	: Scanning electron microscope
SMA	: Shape memory alloy
SOPT	: Second-order phase transition
SOMT	: Second-order martensitic transition
T_A	: Martensitic to austenite transition temperature
T_C	: Curie temperature
TEC	: Average magnetic entropy change
T_{irr}	: Irreversible temperature
T_M	: Austenite to martensitic transition temperature
T_N	: Neel temperature
T_p	: Peak temperature
U	: Transformation stretch matrix
VSM	: Vibrating Sample Magnetometer
XRD	: X-ray diffractometer
ZFC	: Zero-field cooled

List of Symbols:

a	: lattice constant
C_p	: heat capacity
d	: inter-planner spacing
e	: Electronics charge (e= 1.602 $\times 10^{-19}$C)
e/a	: valance electron concentration ratio
g	: gyromagnetic ratio
G	: Gibbs's free energy
H	: magnetic field
I	: current
k_B	: Boltzmann constant
t_0	: measurement coefficient
M	: Magnetization
λ	: Wavelength
μ_B	: Bohr magneton
μ_0	: Permeability of free space ($4\pi \times 10^{-7}$H/N)
5-M	: Five-modulated-monoclinic
α	: Pre-selection angle
R	: Resistance
ρ	: Electrical resistivity
S	: Entropy
T	: Temperature
t	: Time
θ	: Angle

List of Publications:

[1] **Saheli Samanta**, Subrata Ghosh, and Kalyan Mandal**,** "Observation of giant exchange bias effect in Ni-Mn-Ti all *d*-metal Heusler alloy" ***J.Phys.Condens. Matter 34 105801 (6pp)*** **(2022).**

[2] **Saheli Samanta,** Subrata Ghosh, Sudipta Chatterjee, and Kalyan Mandal, "Large magnetocaloric properties and magnetoresistance in Fe-Co doped $Ni_{50-x}(FeCo)_xMn_{37}Ti_{13}$ all-*d*-metal Ni-Mn-Ti Heusler alloys" **Journal of Alloys and Compounds 910, 164929 (2022).**

[3] **Saheli Samanta,** Sudipta Chatterjee, Subrata Ghosh, and Kalyan Mandal, "Large reversible magnetocaloric effect and magnetoresistance by improving crystallographic compatibility condition in Ni(Co)-Mn-Ti all-*d*-metal Heusler alloys" **Physical Review Material, 6,094411 (2022)**.

[4] Subrata Ghosh, **Saheli Samanta**, Jayee Sinha, and Kalyan Mandal, "Measurement Protocols dependent Giant Magnetocaloric Effect in MnNiSi-based system" **Appl.Phys.Lett,119, 183901(2021).**

[5] Subrata Ghosh, **Saheli Samanta,** J. Sridhar Mohanty, Jayee Sinha and Kalyan Mandal, "Giant room temperature magnetocaloric response in $(MnNiSi)_{1-x}(FeNiGa)_x$ system" ***Journal of Applied Physics 132, 045001*** **(2022).**

[6] **Saheli Samanta**, Sudipta Chatterjee, and Kalyan Mandal, "Giant reversible magneto-responsive properties driven by phase-fraction-assisted Martensitic Transformation in Cu alloyed all-d-metal Ni-Co-Mn-Ti Heusler alloys" (Under preparation)

[7] Sudipta Chatterjee, Jyotirmay Sau, Subrata Ghosh, **Saheli Samanta**, Manoranjan Kumar, Barnali Ghosh, and Kalyan Mandal, "Anomalous Hall effect in topological weyl and nodal-line semimetal Heusler compound Co_2VAl" ***J.Phys.Condens. Matter*** 35 (2023) 035601 (9pp).

[8] Sudipta Chatterjee, **Saheli Samanta**, Barnali Ghosh, and Kalyan Mandal “Anomalous transport properties in ferromagnetic Heusler compound Co2MnGe: An experimental realization of half-metallic ferromagnetism” (Under Review)

[9] Sudipta Chatterjee, Jyotirmay Sau, **Saheli Samanta**, Barnali Ghosh, Nitesh Kumar, Manoranjan Kumar, and Kalyan Mandal "Berry phase driven large intrinsic anomalous Hall effect in topological semimetallic Heusler compound Co2CrGa due to nodal-line and triple point fermion" (Under Review)

List of attended conference:

International:

[1] " MMM-INTERMAG – "Large plateau like Magnetic entropy change in Sn doped Ni Co Mn Ti all-d-metal Heusler alloy " (oral presentation, published in abstract book) January 10 –14, 2022, New Orleans, LA.

National:

[2] " QMAT, –Tuning magnetic and magnetocaloric properties in Co-doped Ni-Mn-Ti all-d-metal Heusler alloy (Talk) 2020 September 7 –11, 2020, S.N Bose National Centre for Basic Sciences.

Table of Contents

Chapter 1 Introduction

This introductory Chapter consists of a basic principle of the magnetocaloric effect and its related thermodynamics. We provide a short literature survey of the development of new and superior materials and the study of their various physical and application-related properties. This chapter also includes the motivation for the work undertaken in the thesis.

1 Introduction

1.1 Preface

Energy-functional materials have always been a considerable interest to the fundamental and material science, as well as engineering community due to their various physical properties and applications in a large scale. From bulk to nano structure, their evolution has grown rapidly. Generally, these kinds of materials exhibit some specific function by external stimuli such as temperature, magnetic field, mechanical force, electric current, stress and so on. Among them, magnetic materials play a vital role on improving the efficiency and performance of device in magnetic power generation, conversion, conditioning, and transportation. The use of energy in different section like the commercial sector, refrigerator, and air conditioner, accounts for a huge fraction of electricity use. Therefore, the total consumption of electricity by the entire world population is approximately 16.38 trillion kW.h [1]. For instance, most refrigeration systems and air conditioners still use the global warming volatile or ozone depleting liquid refrigerant materials. These refrigerants contain hazardous gases like chlorofluorocarbons (CFCs), hydrochlorofluorocarbons (HCFCs) that are suspected to deplete the ozone layer of the atmosphere [2]. These greenhouse gases have global warming potential thousands of times greater than CO_2.

Therefore, this issue can be mitigated if caloric effects in solid materials are entirely utilised in renewable energy resources as well as in technologies. Renewable energy resources are related to the conversion of solar energy, wind, hydropower, biomass, and geothermal energy into electric power [1,3–6].

Magnetic refrigeration which works on the principle of magnetocaloric effect (MCE), has tremendous potential over the conventional vapor compressor refrigerators. Conventional vapor compressor refrigerators are heavy, bulky, energy inefficient and being echo-harmful system, whereas magnetic refrigeration is expected to be potentially applicable in solid-state-based modern refrigeration devices due to its environment-friendly nature [7–10]. The energy efficiency of a magnetic refrigerator is enhanced up to 30% higher than that of convention gas compressor refrigerator [1,7].

The study of magnetic refrigeration based on MCE, was first discovered on 1881 by German physicist Emil Warburg who observed the temperature change in Fe under the application of magnetic field [11]. In 1905, Langevin predicted that a paramagnet can change its temperature when being magnetized and demagnetized. Later, Weiss and Piccard observed experimentally a thermal response of Ni around its Curie temperature (T_C) under magnetic field in 1917 [12]. Subsequently, Debye in 1926 [13], and Giauque in 1927 [14], independently proposed the method using adiabatic demagnetization to reach a ultra-low temperature. Using this approach, in 1933, Giauque and MacDugall carried out an experiment on paramagnetic $Gd_2(SO_4)_{3.8}H_2O$ salt as a magnetic refrigerant and they attained to reach a millikelvin temperature, 0.25 K [15]. Indeed, Giauque received "The Nobel Prize in Chemistry" 1949 for his contribution in the "Concerning the behaviour of substance at extremely low temperature". The next milestone for room-temperature (RT) magnetic refrigeration working was reached by Brown, in 1976 [16]. After that, Gd, a benchmark material with outstanding properties, was discovered as the most active magnetic refrigerant at RT magnetic refrigeration [17]. As breakthrough occurred in 1997, Pecharsky and Gschneidner discovered that giant MCE of $Gd_5(Si_2Ge_2)$ alloy was two times larger than Gd [18]. Since then, lot of investigation has been performed by several researcher group on various rare-earth-based materials [19,20,29–34,21–28]. Although the rare-earth elements with large saturation magnetization have been investigated intensively as large magnetocaloric materials, the expensive of the raw materials and their availability are the main key issues for the commercial applications. In this context, transition metal-based alloys have been explored as a promising magnetic refrigerant material with giant magnetocaloric properties near room temperature to make the magnetic refrigeration cost-effective [35,36,45–54,37–44].

1.2 Thermodynamics of magnetocaloric effect

The change in temperature of a magnetic material upon application or removal of magnetic field is known as MCE [7,9]. The magnitude of MCE is usually characterized as adiabatic temperature change (ΔT_{ad}) and isothermal magnetic entropy change (ΔS_M). The magnetocaloric material which exhibits large temperature change under relatively small magnetic field is the most crucial requirement for a Magnetic Refrigeration device. MCE is an intrinsic property to all magnetic materials. Magnetic material has two sources of internal energies. One is the phonon excitations which are connected to the lattice degree of freedom and another is the magnetic excitation, related with spin degrees of freedom. These two degrees

of freedom are coupled to each other by spin-lattice coupling that regulate free energy transfer within mili-second time scale.

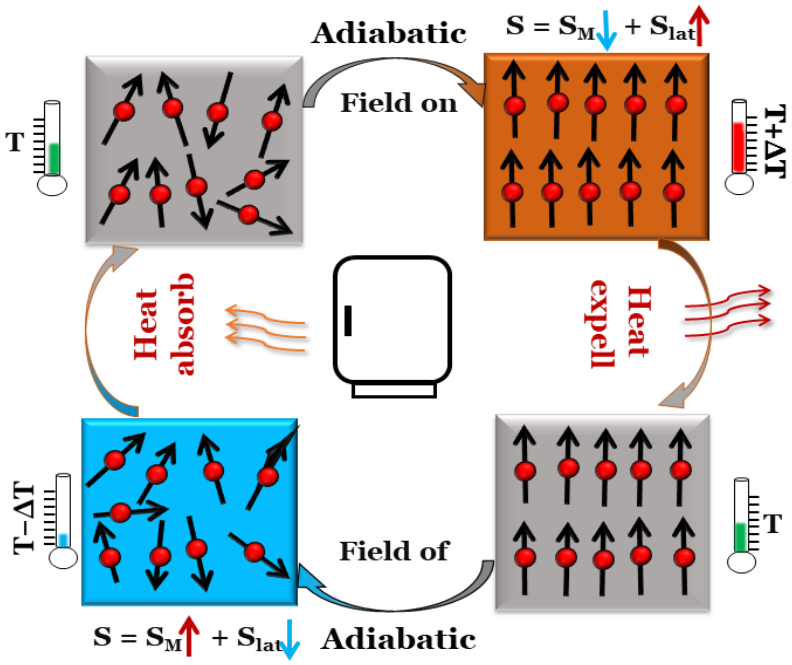

Figure 1.1: Schematic of a simple Magnetic Refrigeration cycle. Here white-grey, orange, and blue colors depict the material in ambient, high and low temperature region, respectively.

The fundamental principle of MCE and magnetic refrigeration cycle is schematized in **Fig. 1.1**, in which the magnetic moment of the material is initially oriented in a random way.

The total entropy of the magnetic material at constant pressure is as a function of both magnetic field (H) and absolute temperature (T) and is expressed as follows [55],

$$S(T,H) = S_{\mathrm{M}}(T,H) + S_{lat}(T) + S_{el}(T) \qquad \textbf{(1.1)}$$

where, $S_{\mathrm{M}}(T,H)$ is concerned to the magnetic entropy caused by the ordering of magnetic spin. $S_{lat}(T)$ is the lattice entropy, originates from the vibration of crystal lattice and $S_{el}(T)$ is electronic entropy of the material's free electrons.

When the material is subjected adiabatically to external magnetic field, due to the alignment of magnetic spins in the direction of the magnetic field, magnetic entropy reduces as the entropy is a measure of disorder of a thermodynamic system; a higher order is related to a lower entropy and vice versa. As the process is conducted adiabatically, the total entropy of the material remains constant. Therefore, to compensate the reduction in magnetic entropy, the lattice

entropy increases, resulting in an increase in temperature of the material. This heat is expelled from the material to the environment through heat transfer. In a similar manner, upon removal of the field, due to the spin fluctuation, magnetic entropy rises, leading to the decrease in the material's temperature. Then, heat from the environment is absorbed by the material to come back to the initial temperature through heat transfer medium.

The total entropy (*S*-*T* diagram) of a ferromagnetic material with increasing temperature for two constant magnetic fields (H = 0, H_0 and H ≠0, H_1) is illustrated in **Fig. 1.2**. Based on the figure to understand the thermodynamics of MCE, two relevant processes are shown in the diagram. One, the application of a magnetic field under adiabatic condition causes heating of the material by $\Delta T_{ad}(T, \Delta H) = T_1 - T_0$, which is indicated as the horizontal line. Secondly, when the magnetic field is applied in an isothermal condition (*T* = constant), the total entropy decreases due to decrease in magnetic contribution. Therefore, the isothermal magnetic entropy change is marked as the vertical line and can be found as $\Delta S_M(T, \Delta H) = S_M(T_0, H_0) - S_M(T_0, H_1)$. Both ΔT_{ad} and ΔS_M are function of initial temperature (T_0) and the magnetic field change ($\Delta H = H_1 - H_0$).

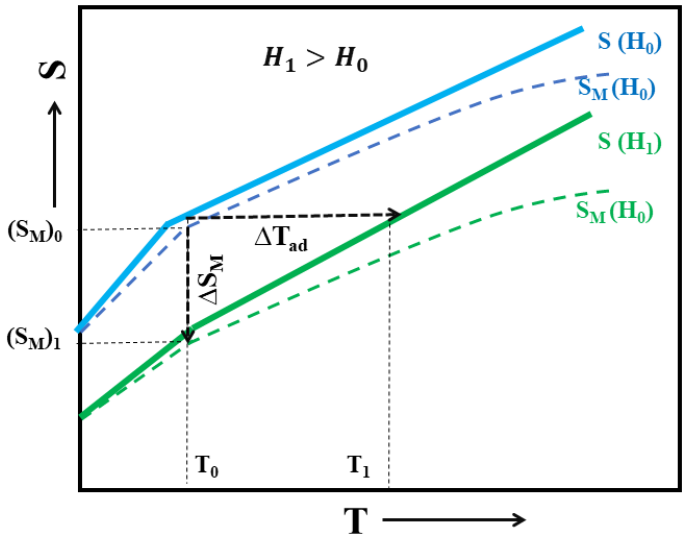

Figure 1.2: Schematic illustration of the total entropy as a function of temperature for a ferromagnetic sample under zero and a non-zero magnetic field. Isothermal magnetic entropy change and adiabatic temperature change are indicated.

1.2.1 Maxwell relation for MCE

If we consider the ferromagnetic sample as a thermodynamic system, then the total Gibbs free energy (G) as a function of volume V, magnetic field H, and pressure P at temperature T can be written as,

$$\mathrm{d}G = V\mathrm{d}P - S\mathrm{d}T - \mu_0 M\mathrm{d}H \tag{1.2}$$

where M, μ_0 are magnetization of the material and permeability in the free space, respectively.

Thus, the entropy and magnetization can be evaluated from the above equation as,

$$S = -\left(\frac{\partial G}{\partial T}\right)_{P,H} \text{ and } M = -\frac{1}{\mu_0}\left(\frac{\partial G}{\partial H}\right)_{P,T} \tag{1.3}$$

If we take the partial differentiation of S with respect to H and of M with respect to T, the equality gives the following Maxwell relation,

$$\left(\frac{\partial S}{\partial H}\right)_{P,T} = \mu_0 \left(\frac{\partial M}{\partial T}\right)_{P,H} \tag{1.4}$$

Let us consider to the isobaric case, i.e., P = constant, $\mathrm{d}P = 0$. The entropy is a function of T and H, the differential form of entropy can be written as,

$$\mathrm{d}S = \left(\frac{\partial S}{\partial T}\right)_{P,H} \mathrm{d}T + \left(\frac{\partial S}{\partial H}\right)_{P,T} \mathrm{d}H \tag{1.5}$$

First, we consider the isothermal process, $\mathrm{d}T = 0$ and using the equation (**1.5**)

$$\mathrm{d}S = \left(\frac{\partial S}{\partial H}\right)_{P,T} \mathrm{d}H = \mu_0 \left(\frac{\partial M}{\partial T}\right)_{P,H} \mathrm{d}H \tag{1.6}$$

The total isothermal magnetic entropy changes due to magnetic field changes from H_1 to H_2, takes the form:

$$\Delta S_{\mathrm{M}}(T, \Delta H) = \mu_0 \int_{H_1}^{H_2} \left(\frac{\partial M}{\partial T}\right)_{P,H} \mathrm{d}H \tag{1.7}$$

Second, an adiabatic process, since there is no heat exchange between system and surrounding ($\delta Q = 0$). Hence, the total entropy of the system is constant i.e. $\mathrm{d}S = \frac{\delta Q}{T} = 0$. Therefore, from equation (**1.5**) we get,

$$\mathrm{d}T = -\mu_0 \left[\left(\frac{\partial S}{\partial T}\right)_{P,H}\right]^{-1} \left(\frac{\partial M}{\partial T}\right)_{P,H} \mathrm{d}H \tag{1.8}$$

We introduce the heat capacity (C) of the sample under constant magnetic field,

$$C_{P,H} = \frac{\mathrm{d}Q}{\mathrm{d}T} = T\left(\frac{\mathrm{d}S}{\mathrm{d}T}\right)_{P.H} \quad \textbf{(1.9)}$$

Therefore, the equation (**1.7**) modifies as,

$$\mathrm{d}T = -\mu_0 \frac{T}{C_{P,H}}\left(\frac{\partial M}{\partial T}\right)_{P,H} \mathrm{d}H \quad \textbf{(1.10)}$$

The total adiabatic temperature changes due to field changes from H_1 to H_2, takes the form:

$$\Delta T_{\mathrm{ad}}(T, \Delta H) = -\mu_0 \int_{H_1}^{H_2} \frac{T}{C_{P,H}}\left(\frac{\partial M}{\partial T}\right)_{P,H} \mathrm{d}H \quad \textbf{(1.11)}$$

Equations (**1.7**) and (**1.11**) are well known as Maxwell's equations. From the both equations (**1.7**) and (**1.11**), the magnetocaloric properties, namely ΔS_{M} and ΔT_{ad} of any magnetic material can be estimated experimentally from temperature dependent magnetization measurement in different magnetic field.

1.2.2 Criteria for getting large MCE parameters

The criteria for achieving larger MCE parameters is required to explore better magnetocaloric systems and standardize them further for potential applications. The Currie-Weiss law under the high temperature and low magnetic field condition is taken into consideration, where M will be uniform throughout the entire material and hence, the susceptibility is given by [56],

$$\chi = \frac{M(T,H)}{H} = \frac{Ng^2\mu_B^2 J(J+1)}{3Ak_B(T-T_C)} \quad \textbf{(1.12)}$$

The symbols, $N, g, \mu_B, J, A, k_B \; and \; T_c$ stand for number of magnetic atoms per unit volume, gyromagnetic ratio, Bohr magneton, total angular momentum quantum number, atomic weight, Boltzmann constant and Currie temperature respectively.

Differentiating the above equation, we get

$$\left(\frac{\partial M(T,H)}{\partial T}\right)_H = -\frac{Ng^2 J(J+1)\mu_B^2}{3Ak_B(T-T_C)^2} \quad \textbf{(1.13)}$$

Using the equation (**1.13**), the equation (**1.7**) and (**1.11**) take form as,

$$\Delta S_{\mathrm{M}}(T, \Delta \mathrm{H}) = -\int_{H_1}^{H_2} \frac{Ng^2 J(J+1)\mu_B^2}{3Ak_B(T-T_C)^2}\, dH \quad \textbf{(1.14)}$$

$$\Delta T_{\mathrm{ad}}(T, \Delta \mathrm{H}) = \int_{H_1}^{H_2} \left(\frac{T}{C(T,H)}\right)_M \frac{Ng^2 J(J+1)\mu_B^2}{3Ak_B(T-T_C)^2}\, dH \quad \textbf{(1.15)}$$

From the above two equations (**1.14**) and (**1.15**), it is clear to state that the materials should have large ΔS_{M} and ΔT_{ad} when $\left(\frac{\partial M}{\partial T}\right)_H$ is large and specific heat of the material is small at the same temperature. This condition is true for paramagnetic sample near zero Kelvin where, magnetic susceptibility diverse and $C(T,H)$ approaches zero. Second, the materials having large J value will be desirable, as both MCE parameters are proportional to J. Another important aspect is to maximize thermal conductivity of the material, as this ensures remarkable temperature change and quick heat exchange. In addition, for room temperature application purposes, T_C of the material should be closed to the working temperature.

1.2.3 *Conventional* and *Inverse* MCE

From the above discussions, it can be understood that the maximum magnitude of MCE parameters of a materials can be expected in the temperature range when phase transition occurs and is associated with the strong change in magnetic states. Thus, depending on the phase transition, MCE can be generally classified into two regions; conventional or direct MCE and inverse MCE. A schematic of the magnetization versus temperature plot and possibility of getting maximum MCE effect across the transition of both types is depicted in **Fig. 1.3**.

Conventional MCE is generally observed in both first and second-order magnetic phase transition materials. For simplicity, we provide the M-T plot in **Fig. 1.3(a)** for second-order materials. When magnetic field is applied, the moment aligns to some extent that leads to a decrease in the magnetic entropy (as discussed in section **1.2**). This decrease in magnetic entropy ΔS_{M} is measured under isothermal conditions. When the process is conducted under adiabatic condition, i.e., total entropy is constant and then, this decrease in magnetic entropy is compensated by the increase in the lattice entropy. Therefore, the external magnetic field results in a heating of the material by ΔT_{ad}.

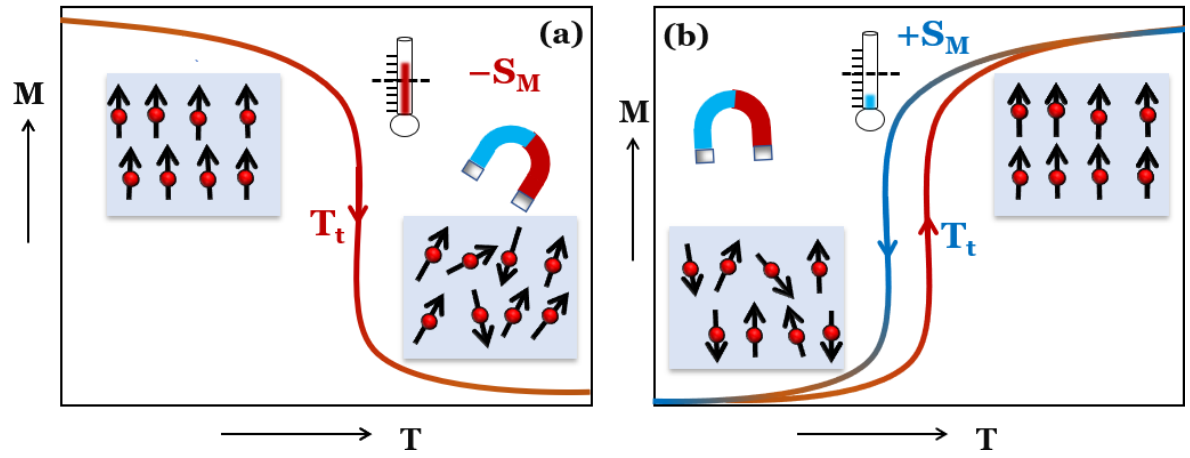

Figure 1.3: Schematic of M-T illustrating (a) the direct (conventional) MCE at 2nd-order transition and (b) inverse MCE at 1st-order transition in the magnetic material, respectively. At high temperatures, material has cubic austenite phase, which changes to low symmetry martensite phase at low temperatures. [T_t represents transition temperature of the respective materials].

Inverse MCE is observed in the first-order phase transition systems like *antiferro-ferro* transitions, and any structural phase transition. In the inverse case, low temperature phase is considered as antiferromagnetic (AFM) or weak magnetic with lower symmetry than that in the high temperature ferromagnetic (FM) phase. As in this case, due to spin ordering of the material, when placed in an external magnetic field adiabatically, magnetic entropy decreases but total magnetic moments due to antiparallel orientation decreased, which dominates over the total spin ordering. Therefore, ΔS_M is raised. As this occurred in the adiabatic environment, that means $\Delta S = 0$, hence lattice entropy decreases, resulting to the lowering in the temperature of the material. In another way, one can say, inverse MCE originates from a structural transition from AFM martensitic to FM austenite phase. Because during structural transition, a large amount of heat is absorbed and this heat are much greater than that of heat released coming from the change of magnetic subsystem.

There are various kind of magnetic materials, with either second-order or first-order, which are used for magnetocaloric cooling. The material having first-order transformation have several advantages of exhibiting giant MCE properties associated with the magneto-structural transition.

1.3 Thermodynamic cycle of magnetic cooling

The refrigeration cycle of magnetic refrigerator is alike to the conventional vapor compression cycle. The only major difference in the use of external stimuli to the working material is hydrostatic pressure for gas refrigeration, whereas magnetic refrigerator uses the magnetic field. In general, magnetic refrigerator operates using combination of various thermodynamic processes such as adiabatic, isothermal and isofield magnetization. Among the thermodynamic cycles, Brayton and Ericsson, cycle are used in room temperature refrigeration [57,58].

1.3.1 Magnetic Ericsson cycle

The Ericsson cycle comprises four thermodynamic processes; two isothermal and two isofield, which is shown by a T-S diagram in Fig. **1.4(a)**. The working principle of Ericsson cycle is as follows:

(1) ***Isothermal magnetization*** **(A-B):** When magnetic field is applied from H_0 to H_1 in the material at the temperature T_{hot} in isothermal condition, then it rejects heat, and the reject heat is transferred to the regenerator fluid.

(2) ***Isofield heat expelling*** **(B-C):** Next, the regenerator absorbs heat from the material under H_1 and drops down the materials temperature (T_{cold}).

(3) ***Isothermal demagnetization*** **(C-D)**: In this process of the demagnetization (from H_1 to H_0) under isothermal condition, material absorbs heat from the load to maintain its previous temperature.

(4) ***Isofield heat absorption*** **(D-A):** Finally, regenerator fluid absorbs heat from the environment. Therefore, this is the cyclic procedure to cool the load.

Indeed, the amount of absorbed and reject heat is not equal. That is why, this cycle is considered as the irreversible process.

1.3.2 *Brayton cycle*

An additional advantage of Brayton cycle is the presence of two adiabatic process instead of two isothermal process. It consists of the two adiabatic and two isothermal processes. A schematic T-S diagram of Brayton cycle is plotted in Fig. **1.4(b)**.

(1) ***Adiabatic magnetization*** **(A-B):** The magnetic material is subjected to a constant magnetic field (H_1) adiabatically and its temperature rises from initial temperature T_1 to $T_1+\Delta T$.

(2) ***Isomagnetic heat expelling*** **(B-C):** This heat is released to the sink through the refrigerant fluid. And the fluid come back to its initial temperature.

(3) ***Adiabatic demagnetization*** **(C-D):** The adiabatic demagnetization causes a reduction of materials temperature (T_1 -ΔT). Then the MCE materials absorbs heat from the refrigerant fluid.

(4) ***Isomagnetic heat absorption*** **(D-A):** Lastly, the MCE material takes up heat from the load and comes back to the initial temperature T_1.

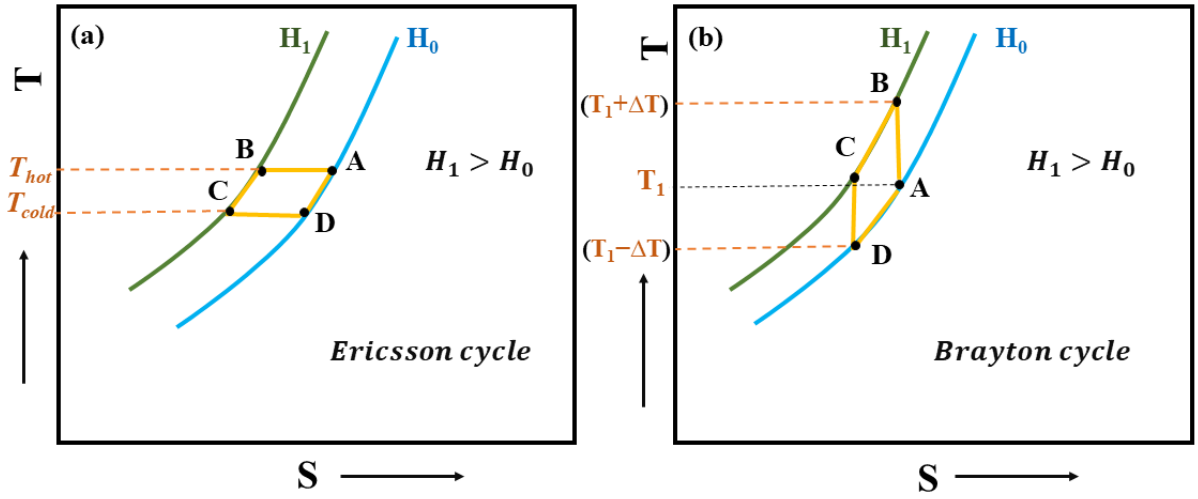

Figure 1.4:T-S diagram of thermodynamic **(a)** Ericson and **(b)** brayton cycle for magnetic refrigeration.

1.4 Experimental technique to obtain MCE

Based on the determination procedure of magnetocaloric parameters, the magnitude of MCE of material is evaluated using direct and indirect methods [34,57,59–61].

1.4.1 Direct MCE

In direct method, the adiabatic temperature change of a magnetic material can be measured [34]. For accurate measurement, the sample must be situated under proper adiabatic condition. Thus, $\Delta T_{ad}(T, \Delta H)$ would be measured as a function of starting temperature [34,62–65]. Noted that the thermal conductivity of the sample should be higher than that of the thermal conductivity of the sample holder for the accurate measurement of the instantaneous temperature change due to field changes.

1.4.2 Indirect MCE

Another easy and common technique for MCE measurement is indirect method. In indirect method, the magnetocaloric parameters are determined following two approaches.

Firstly, the specific heat of the material is measured as a function of temperature in absence and presence of applied magnetic field. Thus, the total entropy of the material can be written in zero field and in non-zero field as [59],

$$S(T,0) = \int_0^T \frac{C(T,0)}{T} dT + S(0,0) \quad \textbf{(1.16)}$$

$$S(T,H) = \int_0^T \frac{C(T,H)}{T} dT + S(0,H) \quad \textbf{(1.17)}$$

where, $S(0,0)$ and $S(0,H)$ are the entropy in zero field and non-zero field at absolute zero and both are same for a condensed system. Hence, subtraction of equation (**1.16**) from equation (**1.17**) results,

$$\Delta S_{\mathrm{M}}(T,\Delta H) = \int_0^T \frac{C(T,H)-C(T,0)}{T} dT \quad \textbf{(1.18)}$$

In other way, indirectly ΔS_{M} can be calculated by measuring the magnetization data isothermally at different temperatures across the transition temperature within a small temperature interval (ΔT) and using the numerical approximation of equation (**1.6**) as,

$$\Delta S_{\mathrm{M}}(T,\Delta H) = \mu_0 \sum_i \frac{\left(M\left(T+\frac{\Delta T}{2},H_i\right)-M\left(T-\frac{\Delta T}{2},H_i\right)\right)}{\Delta T} \Delta H_i \quad \textbf{(1.19)}$$

This method is valid for second-order phase transition materials. But, for first-order phase transition (FOPT) materials, the use of the above equation may give rise overestimated value of the entropy change and creates a spurious peak to the $\Delta S_{\mathrm{M}} - T$ curve across the transition because of field-induced metamagnetic nature. Although the spike-related problem has been solved by different experimental measurement techniques [66].

1.4.3 Relative cooling power

Relative cooling power (RCP) is an important key parameter to quantify the efficiency of magnetic refrigerator. RCP is defined as the amount of heat transfer between hot and cold reservoir during a complete refrigeration cycle and it can be calculated numerically as the area under the $\Delta S_{\mathrm{M}} - T$ curve using the following formula as [57],

$$\mathrm{RCP} = \left|\Delta S_M^{peak}\right| \times \Delta T_{FWHM} \quad \textbf{(1.20)}$$

where, ΔS_M^{peak} is the peak value of ΔS_{M} of $\Delta S_M - T$ curve and ΔT_{FWHM} stands for the temperature span of full width at half maxima of ΔS_M of $\Delta S_{\mathrm{M}} - T$ curve. A potential MCE material should have large RCP value. For this, the material has a large peak ΔS_{M} value as well as $\Delta S_{\mathrm{M}} - T$ curve should be in a broad temperature window.

1.5 Magnetocaloric Materials: Status of the research

Over the last four decades, the magnetocaloric properties of various systems have been intensively investigated as efficient magnetocaloric materials. Mainly, two series of those systems play a major role as much at the fundamental level as in the practical applications. One is rare earth-based materials that are associated with large saturation magnetization originating from localised 4f electrons and are found to exhibit large MCE across the magnetic transition near room temperature. But, due to their high cost, research interest on MCE started to shift towards transition metal-based systems which are more cost-effective than of the first one. In the following section, we have provided a brief review on the investigated magnetocaloric materials so far based on the literature survey and evaluated their temperature dependence magnetic entropy change in terms of a graphical point of view in Fig. **1.5**.

1.5.1 Rare-earth based materials

Rare earth materials show high values of saturation magnetization, coming from the strongly localised 4f electrons. From the pure lanthanide elements, Gd ($7\mu_B$) is considered as a benchmark material for room-temperature magnetic refrigeration, that exhibits large magnetocaloric effect with ΔS_M ~ 10 $Jkg^{-1}K^{-1}$ at T ~ 294 K due to the field changes of ΔH = 50 kOe [34]. Hence, room temperature giant MCE has been investigated in $Gd_5Ge_2Si_2$ (ΔS_M = 20 J kg^{-1} K^{-1} at 276 K), $Gd_5(Si_{1-x}, Ge_x)_4$ materials. The most promising characteristics of these materials is that they undergo a first order structural and magnetic phase transition that give rises giant MCE. The variation of Si:Ge ratio in these compounds retains the giant MCE properties over a wide tunability in the temperature range of the FOPT (from 20 K~280 K) [31,67]. There are several reports showing giant MCE in other rare earth-based materials such as Laves phases RCo_2(R=Dy, Ho, and Er) compounds, $La(FeSi)_{13}$-based materials, $ThCr_2Si_2$-type compounds, ferromagnetic Lanthanum manganite and other RE containing compounds (shown in **Fig. 1.5**) [24–26,34,57,61,68].

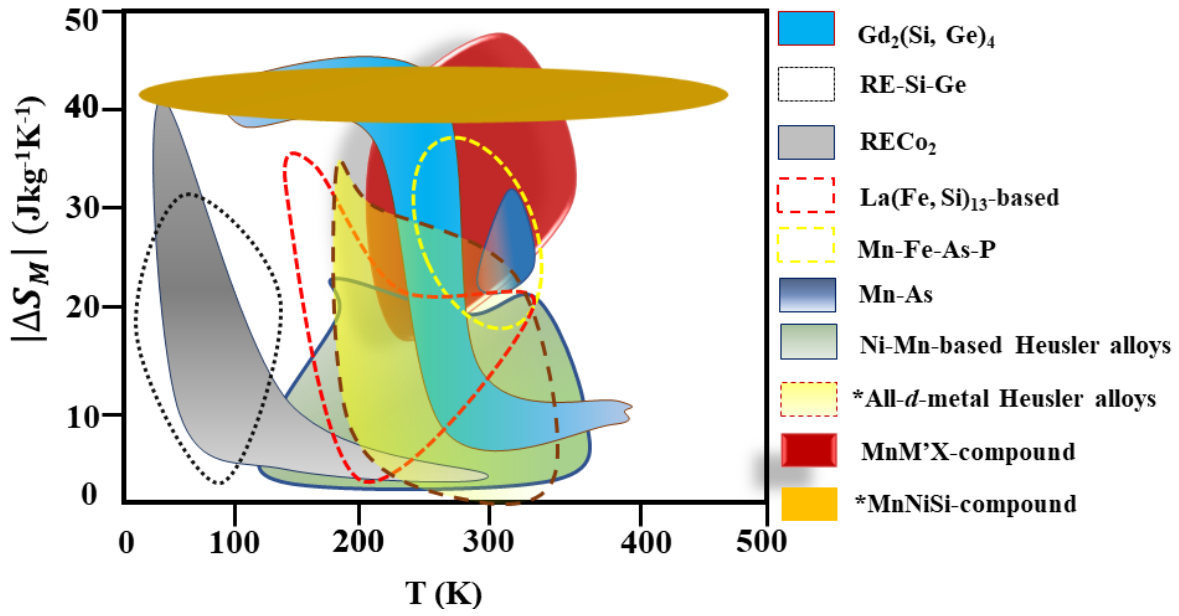

Figure 1.5: A statistical graphic diagram of the maximum peak value of magnetic entropy change as a function of temperature due to the field change 5 T for different class of magnetic materials. [Here RE, M', and X refer to the rare earth, transition element, and p block elements].

1.5.2 MnM'X (M'=Ni, Fe, Co and X = Ge, Si) compounds

From the material cost point of view, rare earth-based materials are highly expensive, that is unfavourable for commercial applications. Along with this, the mechanical properties and chemical stability is also of utmost importance. In this regard, low-cost transition metal-based compounds are best option. In recent years, a hexagonal intermetallic compounds Mn*M'X* M'=Ni, Fe, Co and X = Ge,Si) have been intensively studied as it possesses maximum field-induced entropy change among others promising systems. The general formula of Mn*M'X*; where M'stands for transition metal and X is carbon or boron group elements).

In stoichiometric form, these materials exhibit a first order structural transformation from low-temperature orthorhombic TiNiSi-type structure (Space group: Pnma,62) to high-temperature hexagonal Ni_2In-type structure (Space group: $P6_3/mmc$) in the PM phase, on heating [69–74]. In order to make these systems into desire MCE material, some significant changes need to be introduced. First, FOPT should occur at T_C to establish magnetostructural transition (MST) which is a result of coupling of two transitions. Second, necessary modification is that MST should be lowered in a controllable fashion to near RT.

To achieve this, several strategies such as element substitution, off-stoichiometry, isostructural substitution, heat treatment, or an application of external stimulus like hydrostatic pressure are proposed in order to obtain coupled MST.

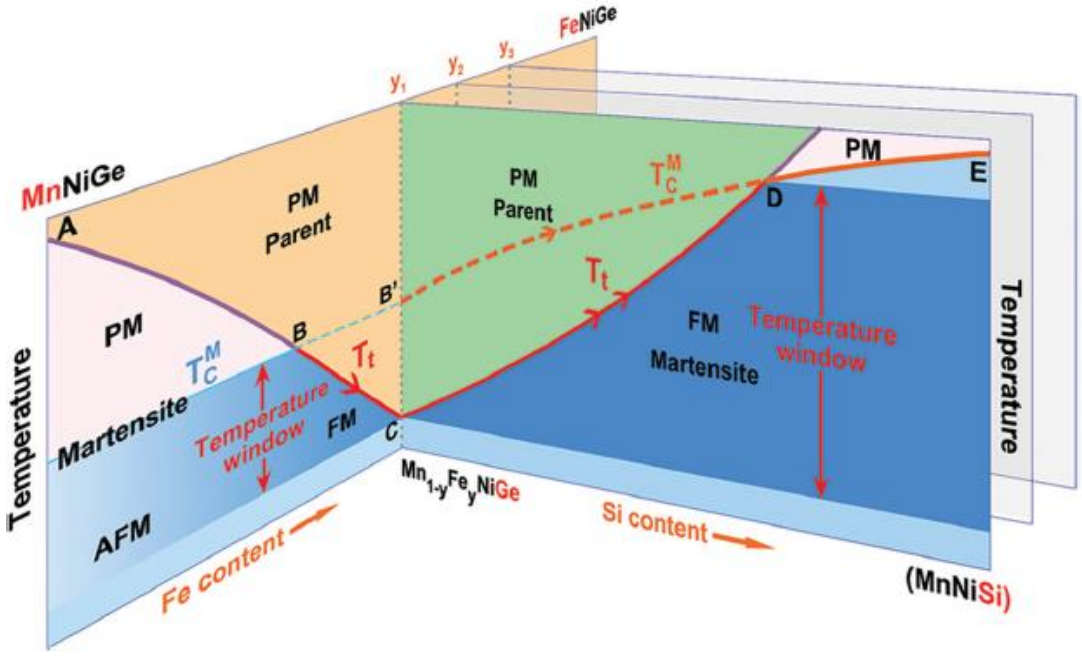

Figure 1.6: A schematic picture of alloy design of (Mn, Fe) Ni (Ge, Si) hexagonal system represented by structural and magnetic phase diagram. [Here, orange and green shaded area represents parent hexagonal phase and light pink and blue area is the orthorhombic martensitic phase and it's Curie-temperature-window (CTW), respectively [75].

The structural and magnetic evolution of these hexagonal systems is elaborated in **Fig. 1.6**. MnNiGe- and MnFeGe- based systems are extensively studied to obtain MST successfully using the above-mentioned principle as their coupled magnetic and structural transition is obtained in CTW region. Stoichiometric MnNiGe [76] exhibits a magnetic transition at a Neel temperature (T_N) of about 346 K and a structural transition at T_M ~470 K, whereas stoichiometric MnCoGe [77] undergoes a magnetic transition at the T_C of about 355 K and structural transitions at T_M ~ 650 K. Fang et al. [78] reported that off-stoichiometric $MnCo_{0.95}Ge_{1.14}$ exhibits first order MST with a large $|\Delta S_M| = 6.4$ J kg^{-1} K^{-1} for $\Delta H = 10$ kOe at peak temperature T = 331 K. In addition to the stoichiometric MnNiSi compound [95] exhibits a giant CTW, in which a highly tunable MST is realized. Therefore, MnNiSi system is taken as our base system.

1.6 Heusler alloys & its structural properties

Our work is devoted to the certain class of multifunctional materials; one of them is Heusler alloy. This Heusler alloy, a long-standing research topic, is named in 1903 after the German metallurgist Friedrich Heusler who synthesised a ferromagnetic Cu_2MnAl alloy using nonmagnetic constituents [79]. The general formula of full and half Heusler compound is X_2YZ, XYZ respectively where, X and Y stand for the transition metal and Z, IIIA-VA group elements [79,80]. From the neutron diffraction measurements, magnetism is found to originate mainly from X and/or Y elements due to the special crystallographic structure. Later, on one hand, they display wide range of various physical phenomena such as magnetic shape memory effect, exchange bias effect, half metallicity and on the other hand, they play an important role in potential applications related to the properties like magnetocaloric effect, elastocaloric effect, giant magnetoresistance, etc. To understand how crystal structure of full Heusler alloys can affect the magnetic exchange interaction and how the interplay between them influences the magnetic properties exhibited in Heusler alloys, we need to study in the light of structural properties. Experimentally, it is observed that the characteristics of full Heusler alloys strongly influenced by the atomic disorder, which can be controlled by heat treatment.

(a) *$L2_1$ structure*

Full-Heusler alloys usually crystallize in the cubic $L2_1$ type structure (space group: $Fm\bar{3}m$) around RT, displayed in Fig. **1.7(a)**. The unit cell consists of four interpenetrating face centred cubic sub-lattices where X atoms occupies the Wyckoff positions A(0, 0, 0) and C(½, ½, ½), Y takes B(¼, ¼, ¼) site, and Z are located at D(¾, ¾, ¾) position. The disorder parameter α is defined as the fraction of either Y or Z atoms whose position in the sublattice is not correct. In this case, α is zero, that means it is completely order structure. It is generally found in Ni_2MnZ (Z=In, Sn, and Sb) Heusler families. In these Heusler families the nature of magnetic coupling is strongly depends on the exchange interaction among magnetic ions. The long-range magnetic ordering is described by localized magnetic moments from Mn atoms, mediated via RKKY indirect exchange interaction [81]. Because Mn magnetic moment is nearly $4\mu_B$, while X atom (Ni, Fe) contributes from 0.2 to $0.4\mu_B$ [82–84]. Therefore, for $L2_1$ structure, the typical interatomic distance between the Mn(B)-Mn(D) site is $\frac{a\sqrt{2}}{2}$, where a is the lattice parameter, favours FM coupling.

The atomic disorder in Heusler alloys is pretty common things that has a strong impact on the electronics structure and physical properties. There are various kind of atomic disorder related to the $L2_1$ structure, which can be controlled by heat treatment. We have described a few of them briefly.

(b) *XA Inverse Heusler structure*

Another important prototype of Heusler compound is inverse XA Heusler structure (space group: $F\bar{4}3m$; $CuHg_2Ti$-type structure) drawn in Fig. **1.7(b)**. In this case, the atom at C site gets interchanged with the atom with B site of the full Heusler alloy. Depending on the atomic occupancy rule, a system crystallises in the regular or inverse Heusler structure. If valance electron of Y atom is higher than the X atom, Y atom occupying the C site and consequently, X is allotted at the B site, then the system crystallise in the inverse Heusler structure [85–87].

(c) *B2 structure*

Another important disorder state is B2-type cubic structure (space group: $Pm\bar{3}m$; CsCl-type structure) where X atom are fixed in their A position but Y and Z are randomly distributed and is shown in Fig. **1.7(c)**. The disorder parameter $\alpha = 0.5$ indicates complete disorder occurring in this type of structure. It is generally found in off-stochiometric ternary compounds, Ni_2MnZ' (Z' = Ga, Al, and Ti). In Ni-Mn-based Heusler alloys, the electronic band structure at Fermi level (E_F) is altered due to strong *p-d* orbital hybridization between X and Z atoms that gives rise to martensitic transition (MT). In the B2 structure, MT can be initiated by *d-d* orbital hybridization between X and Z atoms because Y is randomly positioned in Y and Z atom site. Therefore, in comparison to $L2_1$ structure, the interatomic distance between the Mn(B)-Mn(D) is $\frac{a}{2}$, which is smaller and exhibits energetically favourable AFM magnetic ordering.

(d) *A2 structure*

Lastly in Fig. **1.7(d)**, a completely disorder structure is recognised as A2-type structure (space group: $Im\bar{3}m$) where X, Y, and Z atoms are randomly sited leading to a bcc lattice with reduced symmetry.

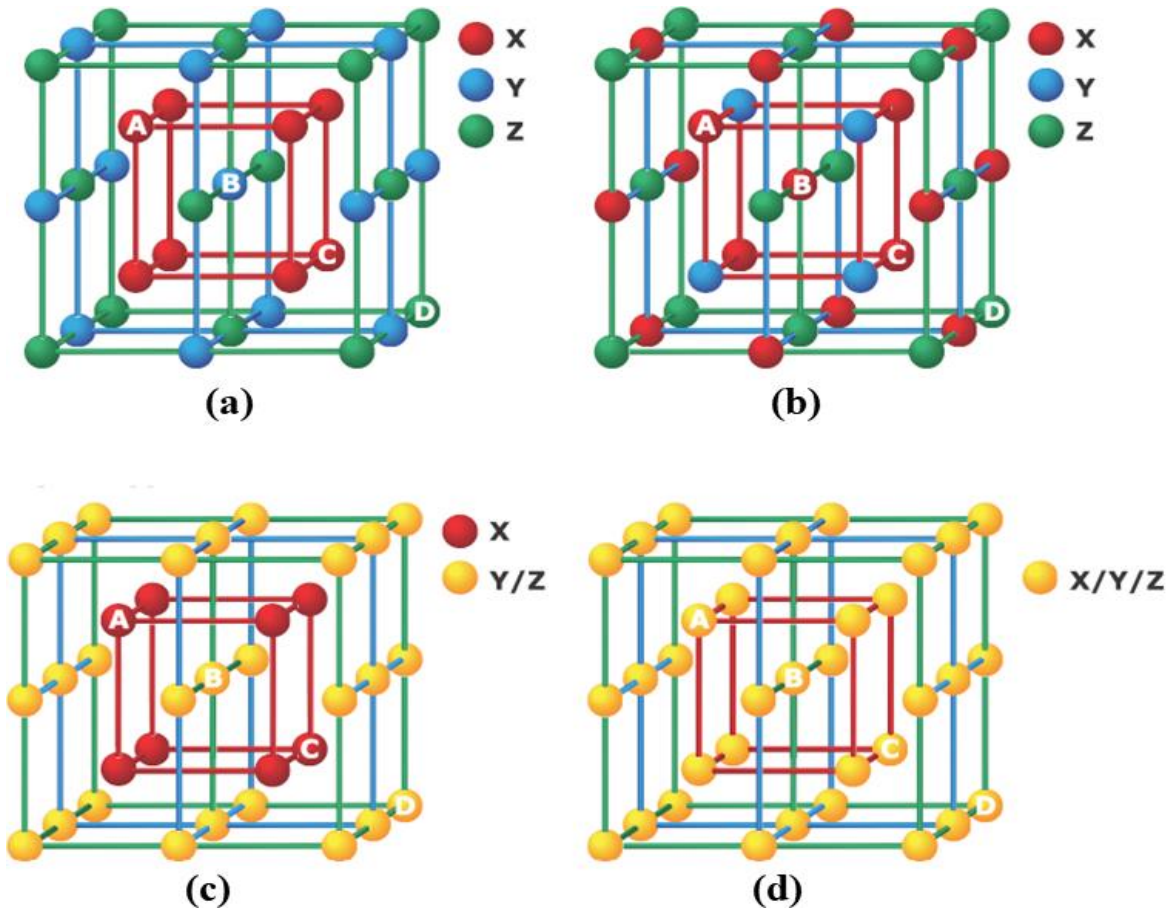

Figure 1.7: Different crystallographic structure of full Heusler alloy. **(a)** order $L2_1$ structure **(b)** inverse XA Heusler structure **(c)** B2-type partially disorder structure, and **(d)** A2-type disorder structure [88].

1.6.1 Martensite transformation in Heusler alloy

Martensitic transformation (MT) is the first-order diffusive or diffusionless solid to solid phase transformation in which atomic movement is less than their interatomic distance [89]. The diffusionless nature of the transformation generates changes in lattice in the unit cell, resulting a lattice distortion in the system. The studies on the martensitic transformation was first observed by Adolf Martens at the end of the 19th century on the microstructure of steels [90]. The low temperature phase is named after name as 'martensite' and the high temperature phase 'austenite' is named after William Chandler Roberts-Austen. A schematic representation of temperature-dependent magnetization curves in the vicinity of MT of Ni-Mn-based Heusler alloy is shown in **Fig. 1.8**.

In this **Fig. 1.8** austenite phase is represented as Cubic lattice and the martensite as monoclinic lattice originating from the distortion of austenite. If the austenite phase is cooled rapidly from the thermodynamic equilibrium temperature, then after a critical temperature

martensitic phase start to form. This critical temperature is known as martensitic start temperature (M_S). Next, their formation finishes after on reaching their martensitic finish temperature (M_f) [91]. Once, the sample is heated in the martensite phase, austenite starts to occur at austenite start temperature (A_S) and finish at austenite finish temperature (A_f). MT temperature is defined as, $T_M = (M_S+M_f)/2$ and the reverse transition temperature is defined as, $T_A=(A_S+A_f)/2$. The difference between T_A and T_M is considered as the hysteresis width (ΔT_{hys}). All the characteristic transitions temperatures are signed in the figure **Fig. 1.8**.

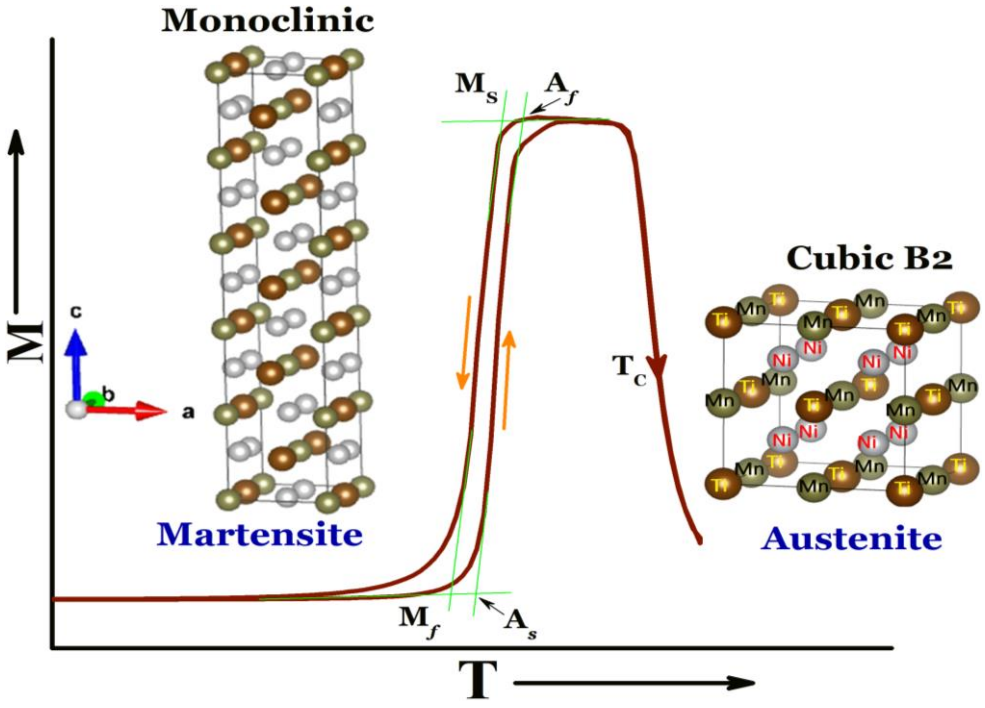

Figure 1.8: Temperature variation of magnetization in the vicinity martensitic transition of Ni-Mn-Ti all-*d*-metal Heusler alloy.

In off-stoichiometry Heusler alloys, this transformation plays a vital role on the change of crystallographic viewpoint and conducts the physical mechanism of the phase transitions. During martensitic transformation, the material is transformed from a high temperature, high symmetry austenite phase to a low temperature, low symmetry martensitic phase with a significant change in crystal structure. Therefore, this mismatch in the crystal lattice between two structures can cause the large elastic strain. Hence, the growth and nucleation mechanism are required to reduce this strain.

Various successful models based on the deformation during MT are described using different mechanism and elaborated that an invariant plane strain occurred in MT, which possess an invariant interface (known as habit plane that is undistorted and unrotated) between the two phases. Considering the elastic strain energy, the deformation of martensite is explained on the basis of geometrical non-linear theory of martensitic transformation, in 1987. This theory can be used in the construction of microstructure of martensite and this microstructure would be result of strain energy minimization and kinetic compatibility. In addition, this theory can also resolved the twin relationship between martensitic variants, volume distortion, and the lattice mismatch (~hysteresis) between two phases with the help of crystallographic calculations [92–95].

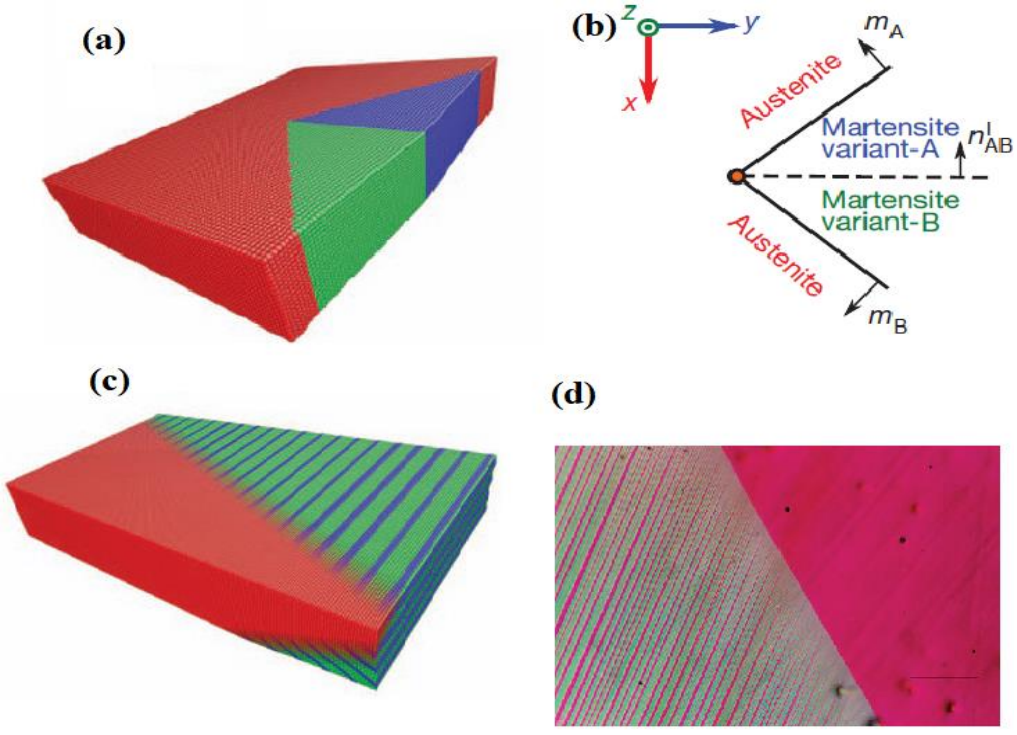

Figure 1.9: (a) Illustration of different twin variants of martensite that forms during transformation. Here red lattice represent austenite phase and other rest color is the variants of martensite phase. (b) In this two-dimensional projections, a triple junction is formed by austenite and other two martensite variants. (c) The transition layer separates the austenite phase from different shape of martensite variants [95]. (d) The final laminated twin martensite microstructure meets at the austenite region [94].

According to the non-linear theory of martensitic, if each pair of twin variants of martensite can form a laminated microstructure in the vicinity of transition, then it meets austenite at a low elastic energy transition layer [95]. In this theory, the deformation of

martensite is considered as F which is composed of two parts: one is unique stretch distortion U and a subsequent pure rigid rotation R. Hence, the deformation gradient can be written as;

$$F=RU$$

This U is a 3×3 homogeneous deformation matrix and it is also known as bain distortion matrix. The determination of U implies the volume change between two phases. Therefore, the geometrical compatibility condition of the material undergoing martensitic transformation is the U = 1 and its middle eigen value λ_2=1.

Figure 1.9 illustrates the starting point of this theory to consider the Bravais lattice of both austenite and martensite phases. Assume, austenite phase has higher symmetry than the martensite. Due to the different in symmetry between two phases, there are multiple number of variants in the martensitic phase over which different representation of point groups are exist. So, the martensitic transformation is occurred when the point group of the martensite phase is the sub group of the point group in austenite phases. If $\mathcal{P}^a$ denotes the point group of austenite phase and $\mathcal{P}^m$ stands for the point group of martensite phase, then the number of possible variants of martensite μ_{def} is determined by the number of possible rotations of the $\mathcal{P}^a$ divided by the number of possible rotations of $\mathcal{P}^m$ and can be written as;

$$\mu_{def} = \frac{\mathcal{P}^a}{\mathcal{P}^m}$$

For example, number of possible rotations in the point group of cubic phase has 24, whereas that in the tetragonal martensite is 8 as well as monoclinic martensite has 2 possible rotations in the point groups. Therefore, the cubic to tetragonal (monoclinic) transformation results 3 (12) variants of martensite, which must have the same eigen values. Hence, a thorough investigation of crystallographic analysis of the microstructural in Ni-Mn-based Heusler alloys is necessary, which can provide the fundamental information of these materials and can help to design the shape memory Heusler alloys using first-order martensitic phase transformations.

1.6.2 Exchange bias in Heusler alloy

In 1956, Meiklejohn and Bean discovered the phenomenon of magnetic exchange anisotropy and a shift of magnetic hysteresis (M-μ_0H) loop along the field axis called exchange bias (EB), while studying Co particles surrounded by AFM CoO oxide [56,57]. When a material is cooled through its Neel temperature under magnetic field, this unidirectional anisotropy forms an easy magnetization axis that arises due to direct exchange coupling at the FM/AFM interface. A

signature of exchange bias phenomenon is schematically shown in **Fig. 1.10**. Since its discovery, EB is an important chapter of advance magnetic device with potential application such as read heads in recording device, spin valve based-magnetoresistive devices, high-density magnetic recording media, magnetoresistive random access memory and so on.

To elaborate on the shift of M-μ_0H loop, a phenomenological model has been taken into consideration for FM/AFM interface. The necessary criteria for the existence of EB is the T_C of FM phase should be higher than the T_N of the AFM phase, $T_C > T_N$.

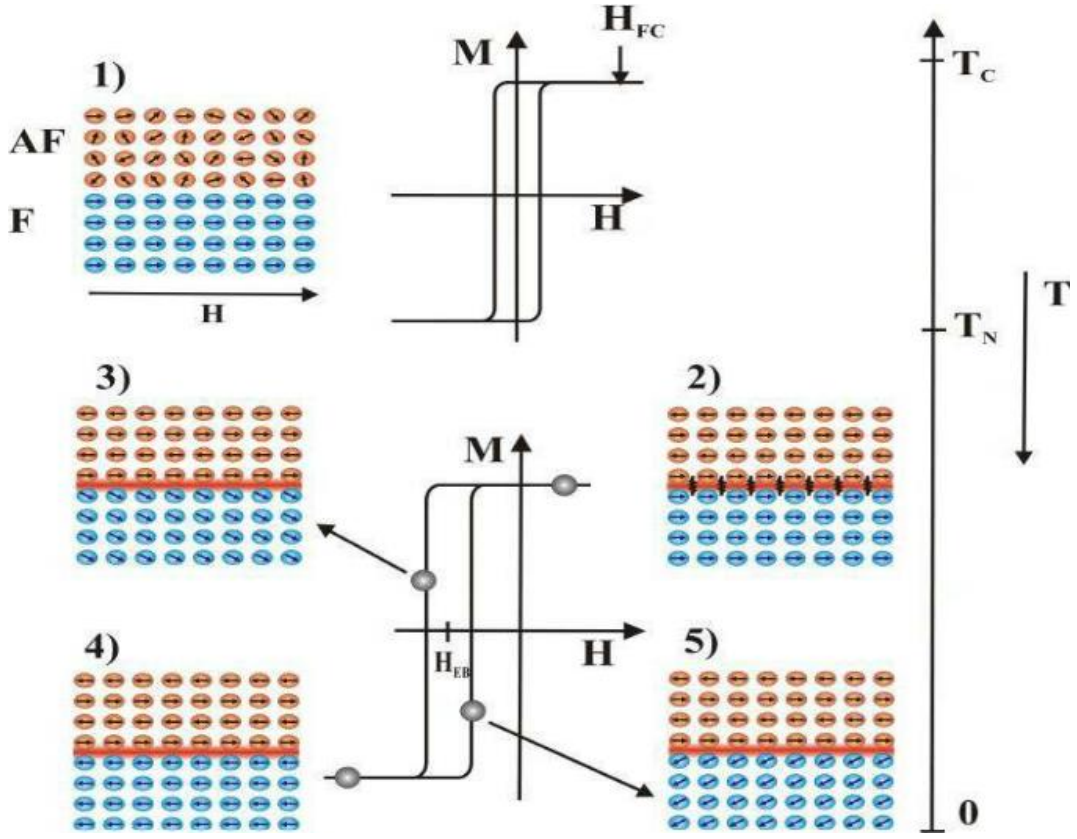

Figure 1.10. The schematic diagram exhibits the phenomenological model of spin configuration for FM/AFM phases (**Source: Internet**)

When the field is applied in the temperature range $T_N < T < T_C$ (see **level 1**), FM spins align with the direction of the applied magnetic field while AFM spins remain randomly oriented. Further cooling $T < T_N$ (**level 2**), due to the interaction at the interface, AFM spins align ferromagnetically at the interface and other AFM spins layer follow AFM order as so produce zero net magnetization. Once the field rotates back in the opposite direction (**level 3**), FM spins start to orient themselves along the field direction but AFM remains unchanged due to their

larger anisotropy energy as well as AFM spins at their interface apply a macroscopic torque on the FM spins to remain them unchanged. As FM has one single stable direction (i.e., unidirectional anisotropy), to overcome this torque an extra amount of field is required to rotate FM spins completely. As a result, a large coercive field (H_C) is obtained (**level 4**). As we reverted back to positive field direction (**level 5**), FM spins rotate back at a smaller field, thereby give rises a horizontal shifting of hysteresis loop from the origin is known as exchange bias field (H_{EB}). The shift along the field axis is generally negative for positive cooling field and it is positive for negative field cooled condition.

The H_{EB} and H_C field is defined as,

$$H_{EB} = -|H_L + H_H|/2 \quad (\mathbf{1.21})$$

$$H_C = |H_L - H_H|/2 \quad (\mathbf{1.22})$$

where, H_L, H_H are the left and right cut-off field respectively at which magnetization becomes zero.

EB is generally observed in the system which is containing AFM-FM interfaces such as in small coated particle, inhomogeneous material and thin film

1.6.2.1 Training effect

There are many interesting properties appearing from experiments that yield various challenges for the exchange bias mechanism. One class of these experiments is rotational hysteresis as a function of the numbers of cycles. A gradual degradation of H_{EB} field is observed upon cycling through consecutive hysteresis loop, known as training effect. The training effect is an important intrinsic property of EB systems. The change of the shape of hysteresis loop and the corresponding decrease of loop shift upon consecutive field cycling after field cooling for a particular temperature is called training effect. It was discovered in 1966, by Paccard et.al in three systems, namely Co-CoO, NiFe-NiFeMn, and NiFe-Cr_2O_3 systems exhibiting FM and AFM coupling [98]. They proposed that the decrease of H_{EB} with increasing loop index n can be satisfied by the following equation,

$$(H_{EB}^1 - H_{EB}^n) \propto 1/\sqrt{n} \quad (\mathbf{1.23})$$

here, n labels the loop index number.

The possible reason of this effect is that the reconfiguration of spin or of the domain of the AFM during consecutive cycling, resulting in fluctuation in the FM/AFM coupling. It has been

observed in various magnetic systems ranging from polycrystalline AFM pinning layers to AFM/FM thin film heterolayers to FM nano domains embedded in an AFM matrix [99,100].

1.6.3 Magnetoresistance in Heusler alloy

A large change in resistivity upon application of external field is termed as magnetoresistance. After the discovery of colossal and giant MR at the end of 20th century, it has been used in a vast application area such as magnetic data storage, reading head of hard disc, and magnetic sensor applications. Recently, Heusler alloys have drawn increasing attention in basic condense matter physics due to their fundamental physical phenomenon in terms of magneto transport properties, topological properties and so on. In these materials, the electrical resistivity arises from two important reasons. One is the scattering of electron by phonon and the scattering from the interaction with spin systems. The electrical resistivity of magnetic material is expressed in the following form,

$$\rho(T) = \rho_o + \rho_{ph}(T) + \rho_{mag}(T) + \rho_{e-e}(T)$$

The term ρ_o, residual resistivity, is the temperature independent, originated from the impurity and defect in the lattice. $\rho_{ph}(T)$ contributes the scattering of electrons from the lattice phonon and $\rho_{mag}(T)$ is the electron-magnon scattering contribution in the magnetic state and last term, $\rho_{e-e}(T)$ denotes the contribution from the electron-electron scattering. Now, the temperature dependence $\rho_{ph}(T)$ term can be defined by $Bloch - Grüneisen$ law:

$$\rho_{ph}(T) = A\{{}^{T}/_{\theta_D}\}^s \int_0^{\theta_D} \frac{x^s e^x}{(e^x - 1)^2} dx \qquad (\mathbf{1.24})$$

For simple metal, at low temperature ($T \ll \theta_D$) s = 5; T^5 for pure electron-phonon scattering and s = 2;T^2 for the case of electron scattering from vibrating impurities.

In magnetic materials, the conduction electron scattering to the magnetic moment also contribute to the total resistivity. The simplest model of such scattering is governed from the exchange interaction between free electrons and localised magnetic moment. The theory of such magnetic scattering was first observed by Kasuya, in which the conduction electron in the s band is scattered by the localised *d*-electrons [101]. In FM materials, at $T>T_C$ the contribution of $\rho_{mag}(T)$ on temperature is independent but at $T< T_C$, it decreases with temperature due to reduction of spin-disorder scattering due to formation of magnetic order [101,102]. However, MR can be calculated using the following formula,

$$MR = \left[\frac{\{\rho(\mu_0 H) - \rho(0)\}}{\rho(0)}\right] \times 100\% \qquad (\mathbf{1.25})$$

where, $\rho(0)$ and $\rho(\mu_0 H)$ is the electrical resistivity under zero and non-zero magnetic field.

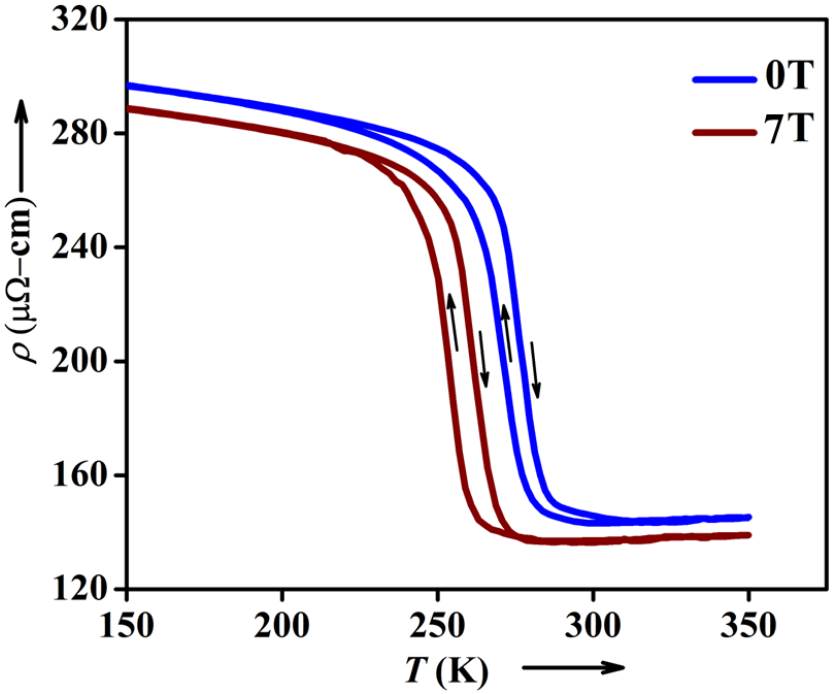

Figure 1.11: Temperature dependent- electrical resistivity for 0T and 7T of Ni(Co)-MnTi all-*d*-Heusler alloy.

The **Fig. 1.11** shows the temperature-dependent-electrical resistivity of the all-*d*-metal Ni(Co)-Mn-Ti Heusler alloy under zero and non-zero magnetic field. The magnetoresistance effect in all-*d*-metal Heusler alloy first studied in 2015 by Wei. et.al [103]. Nevertheless, few researcher caried out the effort with an aim to enhance the magnitude of magnetoresistance. However, on cooling, the transformation from parent austenite phase to the product martensite phase accompanies a significant increase in electrical resistivity. The FOPT causes a large magnetic-field-induced reverse phase transition under the application of external magnetic field, giving rise large negative MR across the transition. In present thesis, we aimed to understand the basic origin and improve magneto-transport properties in Ni-Mn-Ti-based Heusler compounds.

1.7 Motivation and Objective of the Thesis

We have delivered a brief review of some refrigerant materials in the subsection **1.5,** among them, a few systems such as $Gd_5Si_2Ge_2$ [18], $La(Fe,Si)_{13}$-based alloys [25,104] ,and Ni-Mn-based Heusler alloys [105] are found as a promising candidate. All these materials exhibit a field-induced structural transition from AFM or PM to FM phase occurring to a MST which is accompanied with both the change in unit cell volume and sharp magnetization change across the phase transition. However, many fundamental issues of these materials largely restrict the developments in a vast technological application. For example, the significant amount of lattice mismatch in the crystal structure across MT causes large hysteresis that restricts in the potential applications. In addition, the brittleness properties during cycling operation opposes their long term uses in technological applications. Another important issue is the broadening of MT width which addresses strong drawback on the effective use of the materials. Hence the related investigations are greatly required and of significance. Based on such a background, our work emphasizes on novel material design and enhances the magnitude of multifunctional properties, such as MCE, magnetoresistance, and exchange bias from the viewpoint of competition between ferromagnetic and other magnetic interactions, structural, and electronic properties in strongly correlated transition-metal based alloys.

This thesis work is oriented to carry out detail investigations on magneto-responsive properties across their structural transition in MnNiSi-based intermetallic compounds [72,74,106] and Ni-Mn-Ti all-*d*-metal Heusler alloys [103,107,108].

1.8 Organization of the Thesis

The present thesis contains 8 chapters. An overview of all the chapters is summarized as below;

Chapter 1 presents the basic introduction of the theory of magnetocaloric effect and its importance on solid-state cooling refrigeration with thermodynamic cycles. The development of new and superior caloric materials namely, Heusler alloys and Mn*M'X* -based intermetallic compounds and the study of their various physical and application-related properties are discussed. The outline of the thesis has been summarized along with the motivation of the work undertaken in the thesis.

Chapter 2 described the sample preparation, characterization and measurement technique used in the present thesis.

In **Chapter 3**, we delivered an accurate and preferred measurement protocol to determine the MCE response using Maxwell relation in MnNiSi-based systems. We have systematically explored MCE of $(MnNiSi)_{1-x}(FeCoGa)_x$ material with $x = 0.165$ across its MST (~265 K) from various measurement protocols; namely Clausius Clapeyron relation, transformation fraction method, and Maxwell equation. The overall outcomes conclude that the use of Maxwell equation from isothermal magnetization measurement during discontinuous *cooling* and *field increasing mode* would be the preferred protocol to determine magnetocaloric response of these similar types of materials accurately.

In **Chapter 4**, we designed a new caloric material using low-cost, non-toxic, and rare-earth-free elements for room-temperature solid-state-based MR technology. Giant magnetocaloric performances of $(FeNiGa)_x$ ($x = 0.16$, 0.17, and 0.18) doped in $(MnNiSi)_{1-x}$ system is studied. Here, a coupled magnetic and structural transition from paramagnetic hexagonal to ferromagnetic orthorhombic structure at room temperature is observed, leading to a giant magnetocaloric effect. The alloy for $x = 0.17$ is found to exhibit a giant isothermal magnetic entropy change ~63.2 $Jkg^{-1}K^{-1}$ at 305 K due to application of 5T magnetic field.

Chapter 5 deals with the effect of simultaneous substitution of Fe-Co in Ni site on magnetic, structural, magnetocaloric, and magneto-transport properties in all-*d*-metal $Ni_{50-x}(FeCo)_xMn_{37}Ti_{13}$ ($x = 16$, 18, and 20) Heusler alloys. It is interesting to observe that the peak values of magnetic entropy change remain almost insensitive in a wide temperature regime around the room temperature of all the present alloys and the same reflects in the results of magneto-resistance.

Chapter 6 is based on the reversible magnetocaloric effect and magnetoresistance by improving crystallographic compatibility condition in Ni(Co)-Mn-Ti all-*d*-metal Heusler alloys across their first-order MST upon field cycling. In the investigating system, the small hysteresis (~ 4.7 K) of the transformation enables large reversible magnetic entropy changes ~ 17.78 $Jkg^{-1}K^{-1}$, which represents ~91% of the total magnetic entropy change of 19.78 $Jkg^{-1}K^{-1}$ obtained at the first magnetic field ramp. The manipulation of thermal hysteresis through chemical composition tuning, minor hysteresis loop, and crystallographic compatibility has been demonstrated elaborately in order to get reversible magneto-functional properties.

Chapter 7 deals with the phenomenon of exchange bias effect in Ni-Mn-Ti all-*d*-metal Heusler alloy. The observation of giant exchange bias, is attributed to the unidirectional

anisotropy originated due to the FM and AFM interaction at their interface, which has also been justified by time dependence of thermoremanent magnetization, and magnetic memory effect.

Chapter 8 involves the overall summery of the thesis and, possible future works in the related field are discussed.

References:

[1] O. Gutfleisch, M. A. Willard, E. Brück, C. H. Chen, S. G. Sankar, and J. P. Liu, *Magnetic Materials and Devices for the 21st Century: Stronger, Lighter, and More Energy Efficient*, Adv. Mater. **23**, 821 (2011).

[2] A. Cavallini, *Working Fluids for Mechanical Refrigeration — Invited Paper Presented at the 19th International Congress of Refrigeration, The Hague, August 1995*, Int. J. Refrig. **19**, 485 (1996).

[3] J. Mohtasham, *Review Article-Renewable Energies*, Energy Procedia **74**, 1289 (2015).

[4] F. Díaz-González, A. Sumper, O. Gomis-Bellmunt, and R. Villafáfila-Robles, *A Review of Energy Storage Technologies for Wind Power Applications*, Renew. Sustain. Energy Rev. **16**, 2154 (2012).

[5] P. A. Owusu and S. Asumadu-Sarkodie, *A Review of Renewable Energy Sources, Sustainability Issues and Climate Change Mitigation*, Cogent Eng. **3**, (2016).

[6] A. Luque, A. Martí, and C. Stanley, *Understanding Intermediate-Band Solar Cells*, Nat. Photonics **6**, 146 (2012).

[7] K. A. GschneidnerJr, V. K. Pecharsky, and A. O. Tsokol, *Recent Developments in Magnetocaloric Materials*, Reports Prog. Phys. **68**, 1479 (2005).

[8] A. Smith, C. R. H. Bahl, R. Bjørk, K. Engelbrecht, K. K. Nielsen, and N. Pryds, *Materials Challenges for High Performance Magnetocaloric Refrigeration Devices*, Adv. Energy Mater. **2**, 1288 (2012).

[9] L. Mañosa and A. Planes, *Materials with Giant Mechanocaloric Effects: Cooling by Strength*, Adv. Mater. **29**, 1603607 (2017).

[10] O. Gutfleisch, T. Gottschall, M. Fries, D. Benke, I. Radulov, K. P. Skokov, H. Wende, M. Gruner, M. Acet, P. Entel, and M. Farle, *Mastering Hysteresis in Magnetocaloric Materials*, Philos. Trans. R. Soc. A **374**, 20150308 (2016).

[11] E. Warburg, *Magnetische Untersuchungen*, Ann. Phys. **249**, 141 (1881).

[12] M. . Kuz'min and A. . Tishin, *Magnetocaloric Effect. Part 1: An Introduction to Various Aspects of Theory and Practice*, Cryogenics (Guildf). **32**, 545 (1992).

[13] P. Debye, *Einige Bemerkungen Zur Magnetisierung Bei Tiefer Temperatur*, Ann. Phys. **386**, 1154 (1926).

[14] W. F. Giauque, *A THERMODYNAMIC TREATMENT OF CERTAIN MAGNETIC EFFECTS. A PROPOSED METHOD OF PRODUCING TEMPERATURES CONSIDERABLY BELOW 1° ABSOLUTE*, J. Am. Chem. Soc. **49**, 1864 (1927).

[15] W. F. Giauque and D. P. MacDougall, *Attainment of Temperatures Below 1° Absolute by Demagnetization of Gd2(SO4)3.8H2O*, Phys. Rev. **43**, 768 (1933).

[16] G. V. Brown, *Magnetic Heat Pumping near Room Temperature*, J. Appl. Phys. **47**, 3673 (1976).

[17] S. Y. Dan'kov, A. M. Tishin, V. K. Pecharsky, and K. A. Gschneidner, *Magnetic Phase Transitions and the Magnetothermal Properties of Gadolinium*, Phys. Rev. B **57**, 3478 (1998).

[18] V. K. Pecharsky and K. A. Gschneidner, Jr., *Giant Magnetocaloric Effect in Gd5(Si2Ge2)*, Phys. Rev. Lett. **78**, 4494 (1997).

[19] R. D. Shull, V. Provenzano, A. J. Shapiro, A. Fu, M. W. Lufaso, J. Karapetrova, G. Kletetschka, and V. Mikula, *The Effects of Small Metal Additions (Co,Cu,Ga,Mn,Al,Bi,Sn) on the Magnetocaloric Properties of the Gd5Ge2Si2 Alloy*, J. Appl. Phys. **99**, 08K908 (2006).

[20] M. Halder, S. M. Yusuf, M. D. Mukadam, and K. Shashikala, *Magnetocaloric Effect and Critical Behavior near the Paramagnetic to Ferrimagnetic Phase Transition Temperature InTbCo2−xFex*, Phys. Rev. B **81**, 174402 (2010).

[21] V. K. Pecharsky and K. A. Gschneidner, *Tunable Magnetic Regenerator Alloys with a Giant Magnetocaloric Effect for Magnetic Refrigeration from ~20 to ~290 K*, Appl. Phys. Lett. **70**, 3299 (1997).

[22] V. Paul-Boncour and T. Mazet, *Investigation of Compounds for Magnetocaloric Applications: YFe2H4.2, YFe2D4.2, and Y0.5Tb0.5Fe2D4.2*, J. Appl. Phys. **105**, 013914 (2009).

[23] J. Q. Li, W. A. Sun, Y. X. Jian, Y. H. Zhuang, W. D. Huang, and J. K. Liang, *The Giant Magnetocaloric Effect of Gd5Si1.95Ge2.05 Enhanced by Sn Doping*, J. Appl. Phys. **100**, 073904 (2006).

[24] M.-H. Phan and S.-C. Yu, *Review of the Magnetocaloric Effect in Manganite Materials*, J. Magn. Magn. Mater. **308**, 325 (2007).

[25] B. G. Shen, J. R. Sun, F. X. Hu, H. W. Zhang, and Z. H. Cheng, *Recent Progress in Exploring Magnetocaloric Materials*, Adv. Mater. **21**, 4545 (2009).

[26] L. Jia, J. R. Sun, J. Shen, Q. Y. Dong, J. D. Zou, B. Gao, T. Y. Zhao, H. W. Zhang, F. X. Hu, and B. G. Shen, *Magnetocaloric Effects in the La (Fe,Si) 13 Intermetallics Doped by Different Elements*, J. Appl. Phys. **105**, 7 (2009).

[27] B. Podmiljšak, P. McGuiness, B. Miklavič, K. Ž. Rožman, and S. Kobe, *Magnetocaloric Properties and Nanoscale Structure of Fe-Doped Gd5 Ge2 Si2 Alloys*, J. Appl. Phys. **105**, 47 (2009).

[28] E. Yüzüak, I. Dincer, and Y. Elerman, *Magnetocaloric Properties of the Gd5Si2.05-XGe1.95-XMn2x Compounds*, J. Rare Earths **28**, 477 (2010).

[29] W. Wu, A. O. Tsokol, K. A. Gschneidner, and J. A. Sampaio, *Influence of Oxygen on the Giant Magnetocaloric Effect of Gd5Si1.95Ge2.05*, J. Alloys Compd. **403**, 118 (2005).

[30] D. K. Xiong, D. Li, W. Liu, and Z. D. Zhang, *Magnetocaloric Effect of Gd(FexAl1−x)2 Compounds*, Phys. B Condens. Matter **369**, 273 (2005).

[31] V. K. Pecharsky and K. A. Gschneidner, *Effect of Alloying on the Giant Magnetocaloric Effect of Gd5(Si2Ge2)*, J. Magn. Magn. Mater. **167**, L179 (1997).

[32] L. Li, K. Nishimura, D. Tamei, and K. Mori, *Structure, Transport Properties and the Magnetocaloric Effect in Gd(Co1−xNix)2 Pseudobinary Compounds*, Solid State Commun. **145**, 427 (2008).

[33] Z. Gu, B. Zhou, J. Li, W. Ao, G. Cheng, and J. Zhao, *Magnetocaloric Effect of GdCo2−xAlx Compounds*, Solid State Commun. **141**, 548 (2007).

[34] K. A. Gschneidner and V. K. Pecharsky, *Magnetocaloric Materials*, Annu. Rev. Mater. Sci. **30**, 387 (2000).

[35] T. Krenke, E. Duman, M. Acet, E. F. Wassermann, X. Moya, L. Manosa, and A. Planes, *Inverse Magnetocaloric Effect in Ferromagnetic Ni-Mn-Sn Alloys*, Nat. Mater. **4**, 450 (2005).

[36] R. Sahoo, A. K. Nayak, K. G. Suresh, and A. K. Nigam, *Effect of Fe Substitution on the Magnetic, Transport, Thermal and Magnetocaloric Properties in Ni 50 Mn 38−x Fe x Sb 12 Heusler Alloys*, J. Appl. Phys. **109**, 123904 (2011).

[37] K. Mandal, D. Pal, N. Scheerbaum, J. Lyubina, and O. Gutfleisch, *Magnetocaloric Effect in Ni-Mn-Ga Alloys*, in *IEEE Transactions on Magnetics*, Vol. 44 (2008), pp. 2993–2996.

[38] K. Mandal, D. Pal, N. Scheerbaum, J. Lyubina, and O. Gutfleisch, *Effect of Pressure on the Magnetocaloric Properties of Nickel-Rich Ni–Mn–Ga Heusler Alloys*, J. Appl. Phys. **105**, 073509 (2009).

[39] T. Krenke, E. Duman, M. Acet, X. Moya, L. Mañosa, and A. Planes, *Effect of Co and Fe on the Inverse Magnetocaloric Properties of Ni-Mn-Sn*, J. Appl. Phys. **102**, 033903 (2007).

[40] R. Das, S. Sarma, A. Perumal, and A. Srinivasan, *Effect of Co and Cu Substitution on the Magnetic Entropy Change in Ni 46 Mn 43 Sn 11 Alloy*, J. Appl. Phys. **109**, 07A901 (2011).

[41] P. A. Bhobe, K. R. Priolkar, and A. K. Nigam, *Room Temperature Magnetocaloric Effect in Ni–Mn–In*, Appl. Phys. Lett. **91**, 242503 (2007).

[42] I. Babita, S. I. Patil, and S. Ram, *First Order Structural Transformation and Inverse Magnetocaloric Effect in Melt-Spun Ni–Mn–Sn Ribbons*, J. Phys. D. Appl. Phys. **43**, 205002 (2010).

[43] A. Ghosh and K. Mandal, *Large Magnetic Entropy Change and Magnetoresistance Associated with a Martensitic Transition of Mn-Rich Mn50.5-XNi41Sn 8.5+x Alloys*, J. Phys. D. Appl. Phys. **46**, (2013).

[44] A. Ghosh and K. Mandal, *Large Inverse Magnetocaloric Effect in Ni48.5−Co Mn37Sn14.5 (X= 0, 1 and 2) with Negligible Hysteresis*, J. Alloys Compd. **579**, 295 (2013).

[45] A. Ghosh and K. Mandal, *Effect of Structural Disorder on the Magnetocaloric Properties of Ni-Mn-Sn Alloy*, Appl. Phys. Lett. **104**, 031905 (2014).

[46] A. Ghosh, P. Sen, and K. Mandal, *Measurement Protocol Dependent Magnetocaloric Properties in a Si-Doped Mn-Rich Mn-Ni-Sn-Si off-Stoichiometric Heusler Alloy*, J.

Appl. Phys. **119**, (2016).

[47] E. Yüzüak, I. Dincer, Y. Elerman, A. Auge, N. Teichert, and A. Hütten, *Inverse Magnetocaloric Effect of Epitaxial Ni-Mn-Sn Thin Films*, Appl. Phys. Lett. **103**, 222403 (2013).

[48] J. Liu, T. Gottschall, K. P. Skokov, J. D. Moore, and O. Gutfleisch, *Giant Magnetocaloric Effect Driven by Structural Transitions*, Nat. Mater. **11**, 620 (2012).

[49] T. Krenke, E. Duman, M. Acet, E. F. Wassermann, X. Moya, L. Mañosa, A. Planes, E. Suard, and B. Ouladdiaf, *Magnetic Superelasticity and Inverse Magnetocaloric Effect in Ni-Mn-In*, Phys. Rev. B **75**, 104414 (2007).

[50] D. Cong, W. Xiong, A. Planes, Y. Ren, L. Mañosa, P. Cao, Z. Nie, X. Sun, Z. Yang, X. Hong, and Y. Wang, *Colossal Elastocaloric Effect in Ferroelastic Ni-Mn-Ti Alloys*, Phys. Rev. Lett. **122**, 255703 (2019).

[51] A. Taubel, T. Gottschall, M. Fries, S. Riegg, C. Soon, K. P. Skokov, and O. Gutfleisch, *A Comparative Study on the Magnetocaloric Properties of Ni-Mn-X(-Co) Heusler Alloys*, Phys. Status Solidi **255**, 1700331 (2018).

[52] C. L. Zhang, Y. G. Nie, H. F. Shi, E. J. Ye, J. Q. Zhao, Z. D. Han, H. C. Xuan, and D. H. Wang, *Tunable Magnetostructural Coupling and Large Magnetocaloric Effect in Mn1-XNi1-XFe2xSi1-XGax*, J. Magn. Magn. Mater. **432**, 527 (2017).

[53] C. L. Zhang, H. F. Shi, E. J. Ye, Y. G. Nie, Z. D. Han, and D. H. Wang, *Magnetostructural Transition and Magnetocaloric Effect in MnCoGe–NiCoGe System*, J. Alloys Compd. **639**, 36 (2015).

[54] N. T. Trung, L. Zhang, L. Caron, K. H. J. Buschow, and E. Brück, *Giant Magnetocaloric Effects by Tailoring the Phase Transitions*, Appl. Phys. Lett. **96**, 172504 (2010).

[55] A. M. Tishin and Y. I. Spichkin, *The Magnetocaloric Effect and Its Applications - Series in Condensed Matter Physics*, in (2003), pp. 1–475.

[56] C. Kittel, *Introduction to Solid State Physics 7th Edition- Kittel, Charles*, in *John Wiley & Sons* (1996).

[57] V. Franco, J. S. Blázquez, J. J. Ipus, J. Y. Law, L. M. Moreno-Ramírez, and A. Conde, *Magnetocaloric Effect: From Materials Research to Refrigeration Devices*, Prog. Mater.

Sci. **93**, 112 (2018).

[58] J. Romero Gómez, R. Ferreiro Garcia, A. De Miguel Catoira, and M. Romero Gómez, *Magnetocaloric Effect: A Review of the Thermodynamic Cycles in Magnetic Refrigeration*, Renew. Sustain. Energy Rev. **17**, 74 (2013).

[59] V. Pecharsky, K. Gschneidner, A. Pecharsky, and A. Tishin, *Thermodynamics of the Magnetocaloric Effect*, Phys. Rev. B **64**, 144406 (2001).

[60] V. K. Pecharsky and K. A. Gschneidner, *Magnetocaloric Effect from Indirect Measurements: Magnetization and Heat Capacity*, J. Appl. Phys. **86**, 565 (1999).

[61] V. Franco, J. S. Blázquez, B. Ingale, and A. Conde, *The Magnetocaloric Effect and Magnetic Refrigeration near Room Temperature: Materials and Models*, Annu. Rev. Mater. Res. **42**, 305 (2012).

[62] L. Tocado, E. Palacios, and R. Burriel, *Direct Measurement of the Magnetocaloric Effect InTb5Si2Ge2*, J. Magn. Magn. Mater. **290**–**291**, 719 (2005).

[63] S. Y. Dan'kov, A. M. Tishin, V. K. Pecharsky, and K. A. Gschneidner, *Experimental Device for Studying the Magnetocaloric Effect in Pulse Magnetic Fields*, Rev. Sci. Instrum. **68**, 2432 (1997).

[64] F. Canepa, S. Cirafici, M. Napoletano, C. Ciccarelli, and C. Belfortini, *Direct Measurement of the Magnetocaloric Effect of Microstructured Gd Eutectic Compounds Using a New Fast Automatic Device*, Solid State Commun. **133**, 241 (2005).

[65] A. Giguère, M. Foldeaki, B. Ravi Gopal, R. Chahine, T. K. Bose, A. Frydman, and J. A. Barclay, *Direct Measurement of the "Giant" Adiabatic Temperature Change in Gd5Si2Ge2*, Phys. Rev. Lett. **83**, 2262 (1999).

[66] L. Caron, Z. Q. Ou, T. T. Nguyen, D. T. Cam Thanh, O. Tegus, and E. Brück, *On the Determination of the Magnetic Entropy Change in Materials with First-Order Transitions*, J. Magn. Magn. Mater. **321**, 3559 (2009).

[67] V. K. Pecharsky and K. A. Gschneidner, *Advanced Magnetocaloric Materials: What Does the Future Hold?*, Int. J. Refrig. **29**, 1239 (2006).

[68] F. Hu, B. Shen, J. Sun, Z. Cheng, G. Rao, and X. Zhang, *Influence of Negative Lattice Expansion and Metamagnetic Transition on Magnetic Entropy Change in the*

Compound LaFe11.4Si1.6, Appl. Phys. Lett. **78**, 3675 (2001).

[69] T. Kanomata, H. Ishigaki, T. Suzuki, H. Yoshida, S. Abe, and T. Kaneko, *Magneto-Volume Effect of MnCo1−xGe(0⩽x⩽0.2)*, J. Magn. Magn. Mater. **140**–**144**, 131 (1995).

[70] H. Fjellvåg and A. F. Andresen, *On the Crystal Structure and Magnetic Properties of MnNiGe*, J. Magn. Magn. Mater. **50**, 291 (1985).

[71] V. Johnson and C. G. Frederick, *Magnetic and Crystallographic Properties of Ternary Manganese Silicides with Ordered Co2P Structure*, Phys. Status Solidi **20**, 331 (1973).

[72] C. L. Zhang, D. H. Wang, Z. D. Han, B. Qian, H. F. Shi, C. Zhu, J. Chen, and T. Z. Wang, *The Tunable Magnetostructural Transition in MnNiSi-FeNiGe System*, Appl. Phys. Lett. **103**, 132411 (2013).

[73] J. Chen, H. G. Zhang, E. K. Liu, M. Yue, Q. M. Lu, W. H. Wang, G. H. Wu, and J. X. Zhang, *Wide Temperature Window of Magnetostructural Transition Achieved in Mn 0.4 Fe 0.6 NiSi 1−x Ga x by a Two-Step Isostructural Alloying Process*, AIP Adv. **6**, 056220 (2016).

[74] E. Liu, W. Wang, L. Feng, W. Zhu, G. Li, J. Chen, H. Zhang, G. Wu, C. Jiang, H. Xu, and F. de Boer, *Stable Magnetostructural Coupling with Tunable Magnetoresponsive Effects in Hexagonal Ferromagnets*, Nat. Commun. **3**, 873 (2012).

[75] Z. Wei, E. Liu, Y. Li, G.-Z. Xu, X.-M. Zhang, G.-D. Liu, X.-K. Xi, H.-W. Zhang, W.-H. Wang, G.-H. Wu, and X.-X. Zhang, *Unprecedentedly Wide Curie-Temperature Windows as Phase-Transition Design Platform for Tunable Magneto-Multifunctional Materials*, Adv. Electron. Mater. **1**, 1500076 (2015).

[76] W. Bazela, A. Szytuła, J. Todorović, Z. Tomkowicz, and A. Zięba, *Crystal and Magnetic Structure of NiMnGe*, Phys. Status Solidi **38**, 721 (1976).

[77] S. C. Ma, Y. X. Zheng, H. C. Xuan, L. J. Shen, Q. Q. Cao, D. H. Wang, Z. C. Zhong, and Y. W. Du, *Large Roomtemperature Magnetocaloric Effect with Negligible Magnetic Hysteresis Losses in Mn1−xVxCoGe Alloys*, J. Magn. Magn. Mater. **324**, 135 (2012).

[78] Y. K. Fang, C. C. Yeh, C. W. Chang, W. C. Chang, M. G. Zhu, and W. Li, *Large Low-Field Magnetocaloric Effect in MnCo0.95Ge1.14 Alloy*, Scr. Mater. **57**, 453 (2007).

[79] T. Graf, C. Felser, and S. S. P. Parkin, *Simple Rules for the Understanding of Heusler Compounds*, Prog. Solid State Chem. **39**, 1 (2011).

[80] A. Planes, L. Mãosa, and M. Acet, *Magnetocaloric Effect and Its Relation to Shape-Memory Properties in Ferromagnetic Heusler Alloys*, J. Phys. Condens. Matter **21**, (2009).

[81] K. R. Priolkar, P. A. Bhobe, D. N. Lobo, S. W. D'Souza, S. R. Barman, A. Chakrabarti, and S. Emura, *Antiferromagnetic Exchange Interactions in the Ni2Mn1.4In0.6 Ferromagnetic Heusler Alloy*, Phys. Rev. B **87**, 144412 (2013).

[82] P. J. Webster and R. S. Tebble, *The Magnetic and Chemical Ordering of the Heusler Alloys Pd 2 MnIn, Pd 2 MnSn and Pd 2 MnSb*, Philos. Mag. **16**, 347 (1967).

[83] S. Imada, A. Yamasaki, T. Kanomata, T. Muro, A. Sekiyama, and S. Suga, *Composition Dependence of Ni Magnetic Moment in Ni–Mn-Based Heusler-Type Intermetallic Compounds*, J. Magn. Magn. Mater. **310**, 1857 (2007).

[84] P. Lázpita, J. M. Barandiarán, J. Gutiérrez, J. Feuchtwanger, V. A. Chernenko, and M. L. Richard, *Magnetic Moment and Chemical Order in Off-Stoichiometric Ni–Mn–Ga Ferromagnetic Shape Memory Alloys*, New J. Phys. **13**, 033039 (2011).

[85] J. Ma, J. He, D. Mazumdar, K. Munira, S. Keshavarz, T. Lovorn, C. Wolverton, A. W. Ghosh, and W. H. Butler, *Computational Investigation of Inverse Heusler Compounds for Spintronics Applications*, Phys. Rev. B **98**, 094410 (2018).

[86] S. Skaftouros, K. Özdoğan, E. Şaşıoğlu, and I. Galanakis, *Generalized Slater-Pauling Rule for the Inverse Heusler Compounds*, Phys. Rev. B **87**, 024420 (2013).

[87] M. Gilleßen and R. Dronskowski, *A Combinatorial Study of Inverse Heusler Alloys by First-Principles Computational Methods*, J. Comput. Chem. **32**, NA (2009).

[88] V. G. de Paula and M. S. Reis, *All- d -Metal Full Heusler Alloys: A Novel Class of Functional Materials*, Chem. Mater. **33**, 5483 (2021).

[89] F. E. Wang, S. J. Pickart, and H. A. Alperin, *Mechanism of the TiNi Martensitic Transformation and the Crystal Structures of TiNi-II and TiNi-III Phases*, J. Appl. Phys. **43**, 97 (1972).

[90] F. E. Wang, W. J. Buehler, and S. J. Pickart, *Crystal Structure and a Unique*

``Martensitic'' Transition of TiNi, J. Appl. Phys. **36**, 3232 (1965).

[91] K. Bhattacharya, *Theory of Martensitic Microstructure and the Shape-Memory Effect*, Unpubl. Notes 87 (2000).

[92] Z. Zhang, R. D. James, and S. Müller, *Energy Barriers and Hysteresis in Martensitic Phase Transformations*, Acta Mater. **57**, 4332 (2009).

[93] K. F. Hane and T. W. Shield, *Symmetry and Microstructure in Martensites*, Philos. Mag. A **78**, 1215 (1998).

[94] J. Cui, Y. S. Chu, O. O. Famodu, Y. Furuya, J. Hattrick-Simpers, R. D. James, A. Ludwig, S. Thienhaus, M. Wuttig, Z. Zhang, and I. Takeuchi, *Combinatorial Search of Thermoelastic Shape-Memory Alloys with Extremely Small Hysteresis Width*, Nat. Mater. **5**, 286 (2006).

[95] Y. Song, X. Chen, V. Dabade, T. W. Shield, and R. D. James, *Enhanced Reversibility and Unusual Microstructure of a Phase-Transforming Material*, Nature **502**, 85 (2013).

[96] W. H. Meiklejohn and C. P. Bean, *New Magnetic Anisotropy*, Phys. Rev. **105**, 904 (1957).

[97] W. H. Meiklejohn and C. P. Bean, *New Magnetic Anisotropy*, Phys. Rev. **102**, 1413 (1956).

[98] D. Paccard, C. Schlenker, O. Massenet, R. Montmory, and A. Yelon, *A New Property of Ferromagnetic-Antiferromagnetic Coupling*, Phys. Status Solidi **16**, 301 (1966).

[99] C. Binek, *Training of the Exchange-Bias Effect: A Simple Analytic Approach*, Phys. Rev. B - Condens. Matter Mater. Phys. **70**, 1 (2004).

[100] C. Binek, S. Polisetty, X. He, and A. Berger, *Exchange Bias Training Effect in Coupled All Ferromagnetic Bilayer Structures*, Phys. Rev. Lett. **96**, 1 (2006).

[101] T. Kasuya, *Electrical Resistance of Ferromagnetic Metals*, Prog. Theor. Phys. **16**, 58 (1956).

[102] M. Kataoka, *Resistivity and Magnetoresistance of Ferromagnetic Metals with Localized Spins*, Phys. Rev. B **63**, 134435 (2001).

[103] Z. Y. Wei, E. K. Liu, J. H. Chen, Y. Li, G. D. Liu, H. Z. Luo, X. K. Xi, H. W. Zhang, W. H. Wang, and G. H. Wu, *Realization of Multifunctional Shape-Memory*

Ferromagnets in All- d -Metal Heusler Phases, Appl. Phys. Lett. **107**, 022406 (2015).

[104] L. M. Moreno-Ramírez, C. Romero-Muñiz, J. Y. Law, V. Franco, A. Conde, I. A. Radulov, F. Maccari, K. P. Skokov, and O. Gutfleisch, *Tunable First Order Transition in La(Fe,Cr,Si)13 Compounds: Retaining Magnetocaloric Response despite a Magnetic Moment Reduction*, Acta Mater. **175**, 406 (2019).

[105] L. Huang, D. Y. Cong, H. L. Suo, and Y. D. Wang, *Giant Magnetic Refrigeration Capacity near Room Temperature in Ni 40 Co 10 Mn 40 Sn 10 Multifunctional Alloy*, Appl. Phys. Lett. **104**, 132407 (2014).

[106] T. Samanta, D. L. Lepkowski, A. U. Saleheen, A. Shankar, J. Prestigiacomo, I. Dubenko, A. Quetz, I. W. H. Oswald, G. T. McCandless, J. Y. Chan, P. W. Adams, D. P. Young, N. Ali, and S. Stadler, *Hydrostatic Pressure-Induced Modifications of Structural Transitions Lead to Large Enhancements of Magnetocaloric Effects in MnNiSi-Based Systems*, Phys. Rev. B **91**, 020401 (2015).

[107] S. Samanta, S. Ghosh, S. Chatterjee, and K. Mandal, *Large Magnetocaloric Effect and Magnetoresistance in Fe-Co Doped Ni50-(FeCo) Mn37Ti13 All-d-Metal Heusler Alloys*, J. Alloys Compd. 164929 (2022).

[108] A. Taubel, B. Beckmann, L. Pfeuffer, N. Fortunato, F. Scheibel, S. Ener, T. Gottschall, K. P. Skokov, H. Zhang, and O. Gutfleisch, *Tailoring Magnetocaloric Effect in All-d-Metal Ni-Co-Mn-Ti Heusler Alloys: A Combined Experimental and Theoretical Study*, Acta Mater. **201**, 425 (2020).

Chapter 2 Experimental Details

We discuss here a general procedure of sample preparation and characterization and various measurement techniques. Sample preparation in the present thesis is done using Electric arc-furnace (EAF). Crystallographic phase of these samples has been confirmed by X-ray diffraction (XRD) using SmartLab9kW, Rigaku with Cu-K_a radiation. The actual compositions are verified by energy dispersive x-ray (EDX, Quanta FEG 250). To measure physical properties Differential scanning calorimetry (DSC, TA Instrument, Q2000) is used. Magnetic and magneto-transport properties have been measured by physical property measurement system (PPMS, Quantum Design) using the vibrating sample magnetometer (VSM) and electrical-transport option (ETO).

2 Experimental Details

2.1 Sample Preparation

2.1.1 Electric Arc-melting Furnace

Sample in the form of ingot is prepared by melting of high purity raw elements in Tri-arc electric melting furnace (EAF) under argon atmosphere [1]. The whole furnace chamber assembles tri-arc furnace (Centorr Vacuum industries, Model:5TA), dc power supply, rotary pump, chiller and vacuum pump unit. The furnace has two main parts; (i) a copper hearth with positive electrical polarity situated in the bottom section and (ii) in the top section, three electrodes with negative polarity, as represented in **Fig. 2.1**. The water-cooled top and bottom parts of the furnace is separated by Pyrex glass tube for visualization purpose. Each electrode is made of copper stringer with tungsten attached at the end of it. In addition to that, each rod is mounted with swivel ball which helps angular and vertical gesture. A maximum temperature 3000°C and corresponding current ~ 120 A is achieved in this system.

During sample preparation, first each raw element is mounted on the copper hearth. Then furnace is evacuated by vacuum pump and purged with inert gas argon (Ar). About 5 times roughing and purging is required for having good quality of inert atmosphere. Noted that the Ar gas flow is carried on with the melting process to prevent oxidation until sample preparation is finish. Before beginning the melting, titanium is melted by striking the arc to reduce any presence of oxygen inside the chamber. After melting the elements in the form of round block, current is gradually increased and the electrode are moved around and above the sample to improve homogeneity. The sample is capsized after cooling and remelted 5 to 6 times to ensure homogeneity [2].

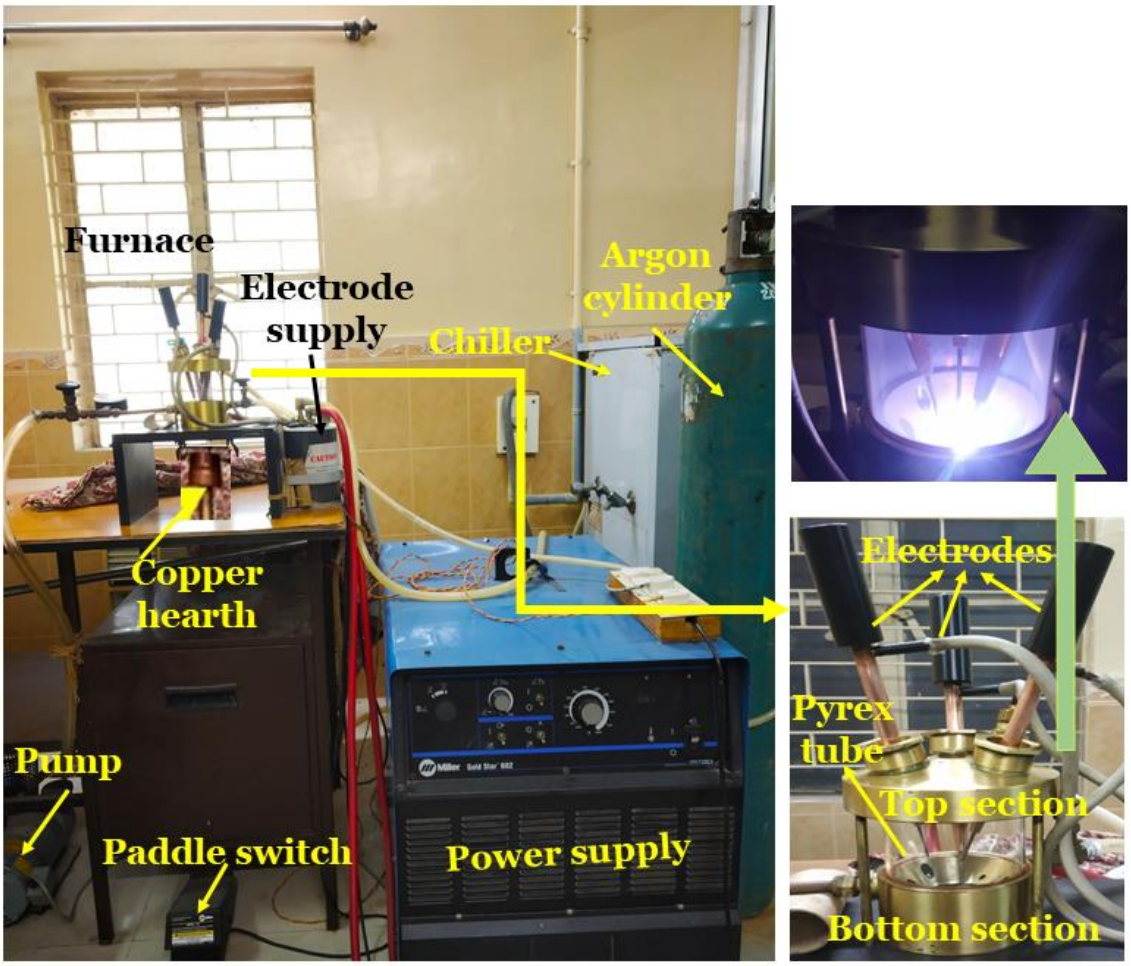

Figure 2.1: An image of electric-Arc melting furnace (Centorr Vacuum Industries model 5TA).

2.1.2 Annealing

The as-prepared ingot is ultrasonicated in alcohol bath for cleaning and sealed with tantalum foils in **Fig. 2.2(a)** to further prevent from oxidation in a evacuated quartz tube. Before sealing, the tube is roughed and parged with Ar for several times so that sample do not oxidise. Then the sample is annealed on their respective temperature for 4 days. Past 4 days of heat treatment, the ingot is quenched into ice water in order to arrest high temperature phase of the sample. The sample is then cut into various shape using low speed saw (Buehler Isomet^{TM}) according to their need in the different experiment. The image of quartz tube, box furnace and cutter machine is shown in **Fig.2.2**.

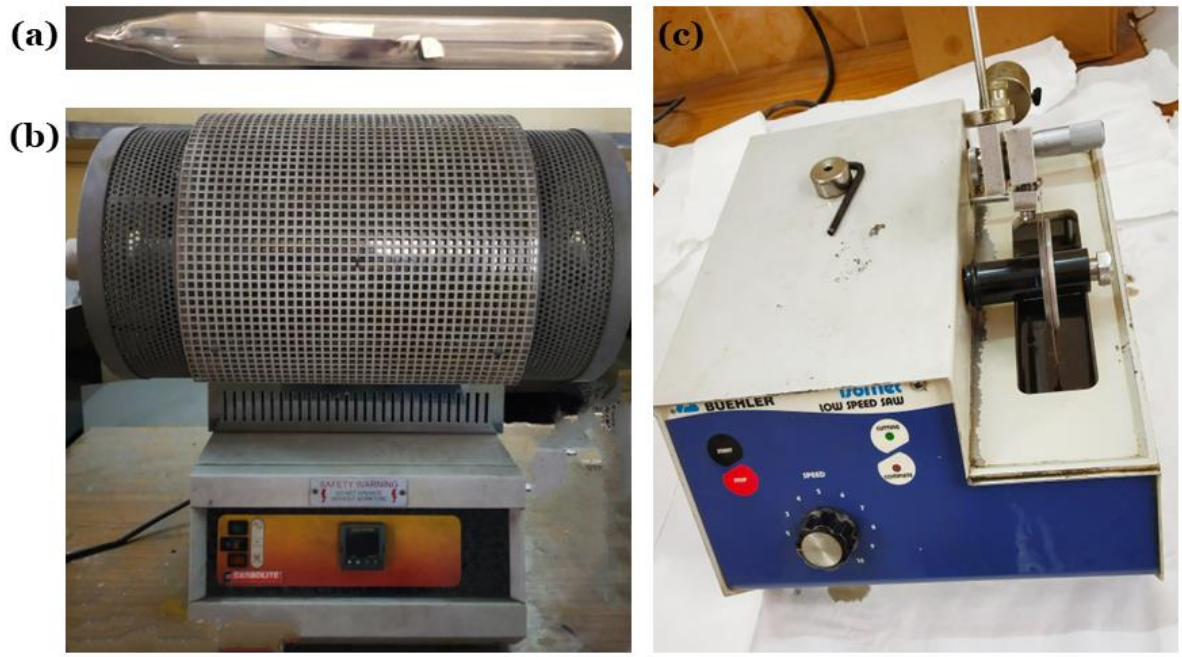

Figure 2.2: Tube furnace (a), a sample with four peace of tantalum foils inside a quartz ampoule, and (c) Buehler low speed saw cutter machine.

2.2 Structural characterization

2.2.1 X-ray Diffractometer (XRD)

X-ray diffractometer (XRD) is used to determine the crystallographic structure of a material. It allows us to study crystal structure, phase, preferred crystallographic direction of plane and other crystal information about lattice strain, average grain size [3]. A block diagram of the X-ray diffractometer is schematized in **Fig. 2.3(a),** where a monochromatic beam of X-ray from the X-ray tube experience on the surface of crystalline material. The electrons from different crystal planes of the material elastically scattered the incident beam, forming outgoing spherical waves. In a few specific angular directions, these scattered waves interfere constructively that are determined by following Bragg's law [4]

$$2d\ \mathrm{Sin}\theta = n\lambda \qquad (\mathbf{2.1})$$

Where d is interplanar spacing in the crystal, θ is the angle of diffraction, λ is the wavelength of the incident beam, and n is an integer (order of diffraction). The diffracted intensity of X-rays is captured by the detector in different directions. The experimental diffraction peak is

identified by comparing its diffraction pattern with standard reference patterns of the Joint Committee on Powder Diffraction Standards (JCPDS).

There are three different experimental method for diffraction study. (i) **Lau method**: θ is fixed and λ is variable. (ii) **Rotating Crystal-method**: λ is fixed, where θ varies with respect to the variation of single crystal. (iii) **Powder method**: like the second one. Noted in this thesis we have used powder diffraction technique because of our polycrystalline sample.

However, powder diffractometer comes into two basic sections: θ-θ system and θ-2θ system. In the θ-θ system, both the X-ray source and the detector concurrently move, but the sample holder is fixed. On the other hand, for θ-2θ system, X-ray source remains fixed and the detector moves at speed twice the rotation speed of the sample holder. In this thesis, a θ-2θ system of Panalytical X-ray diffractometer is used. **Figure 2.3(b**) shows XRD pattern of $(NiMnSi)_{0.83}(FeCoGa)_{0.17}$ polycrystalline sample.

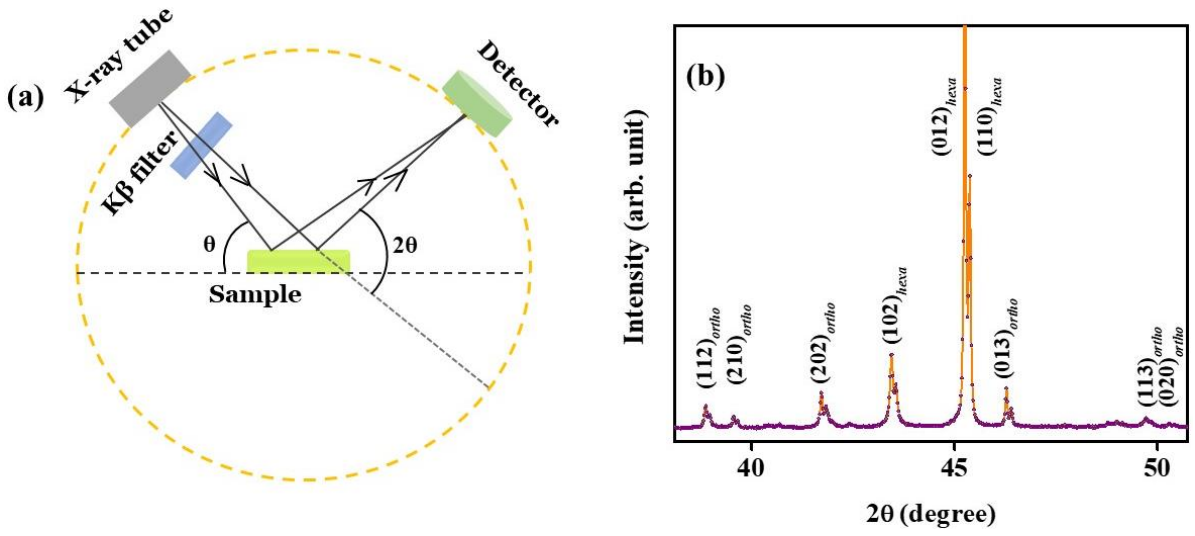

Figure 2.3:(a) Schematic of X-ray diffractometer. (b) Room-temperature-XRD pattern of $(NiMnSi)_{0.83}(FeCoGa)_{0.17}$ hexagonal system.

2.2.2 Scanning electron microscope (SEM)

Scanning electron microscope (SEM) is widely used to study sample's morphology and composition analysis in material science as well as engineering field. In SEM, a branch of electrons beam is generated from an electron gun either by thermionically or cold field emission [5,6], as elaborated in **Fig. 2.4(a)**. An electrostatic field accelerate these electrons and maintained a very high voltage between the source of the electron (cathode) and the anode

plate. Then these accelerated electrons beam gone through electromagnetic lenses which is made of insulated copper wire, and deflected by the magnetic field and take a circular path while passing through the lenses. SEM usually works in a voltage range of 2-50kV with a beam diameter ranging between 5nm- 3µm.

When this accelerated electron interacts with the sample surface, due to inelastic collision between electrons beam and sample, the incident electrons deaccelerated through energy dissipation. As a result, varieties of signals such as secondary electrons, auger electrons, characteristic X-rays, backscattered electrons, and cathodoluminescence are governed. Depending upon their energy, secondary and backscattered electrons are collected and distinguished by the detector. Hence, SEM images of the sample are formed.

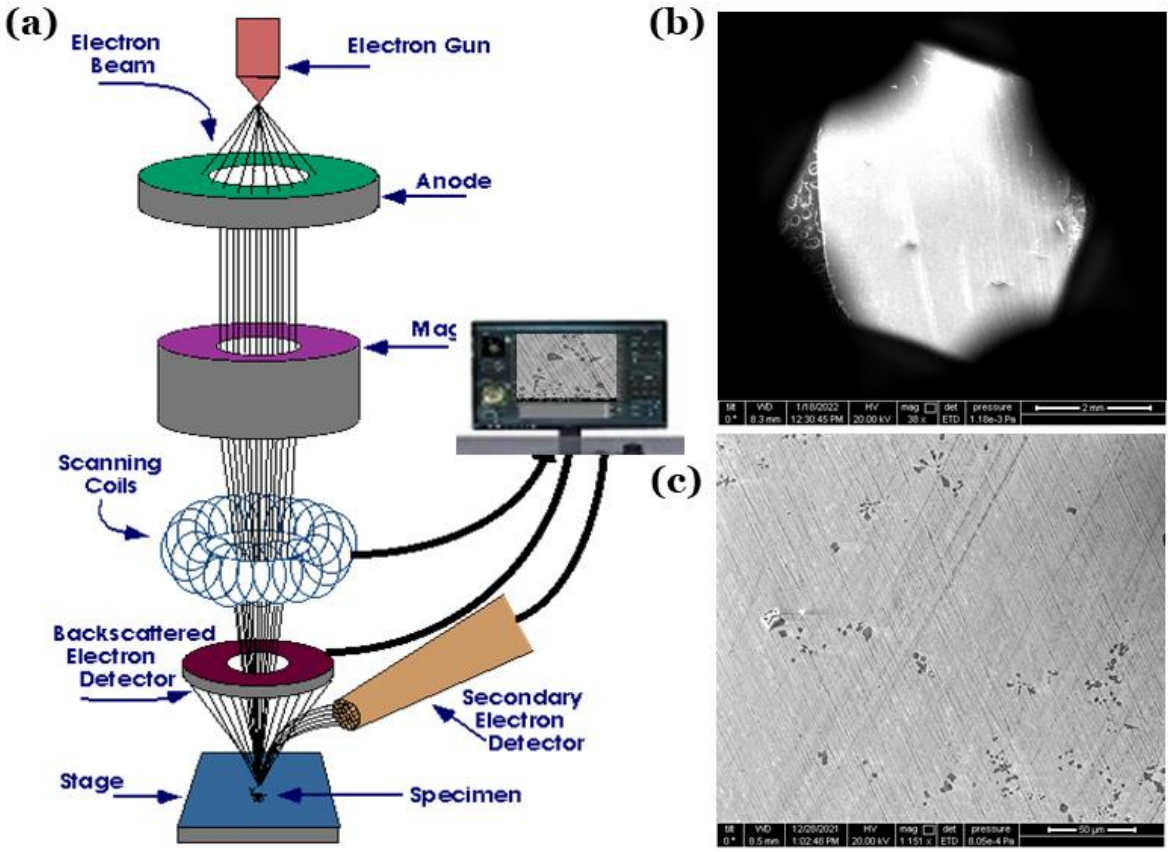

Figure 2.4: (a) Block diagram of an SEM unit. [source from internet]. (b) and (c) SEM micrograph of the Ni(Co)-Mn-Ti all-*d*-metal system.

2.2.3 Energy dispersive analysis of X ray (EDAX)

Energy dispersive analysis of X-ray (EDAX) is often used to microanalysis like chemical composition of a bulk to nano particle [7]. When a material is bombard by high energetic electron beams, the electron from inner shell is ejected from atom of the material. For instance, emission of K-shell electron quits the atom in an excited state. This creates a vacancy in a particular electronic shell and thus an electron from higher energy shell jumps into vacant energy shell. Therefore, the energy difference between these two shells is emitted as a characteristic X-ray from the material. In EDAX, Si or Li detector is generally used as energy dispersive spectrometer that can measure the amount of energy and count the number of emitted X-ray. A typical X-ray spectrum is explained in **Fig 2.5(a)**. In **Fig. 2.5(b)**, a branch of X-ray photons is counted over the binding energy in order to get compositional analysis. The width of characteristic X-ray is calculated from the following equation

$$[N^2 + 5.5F\epsilon\, E]^{0.5} \qquad \textbf{(2.2)}$$

Where N is electronic noise of the system, F is the Fano factor (0.11 for Si), ϵ, the energy to produce an electron hole pair (3.8 eV) and E is the X-ray line energy.

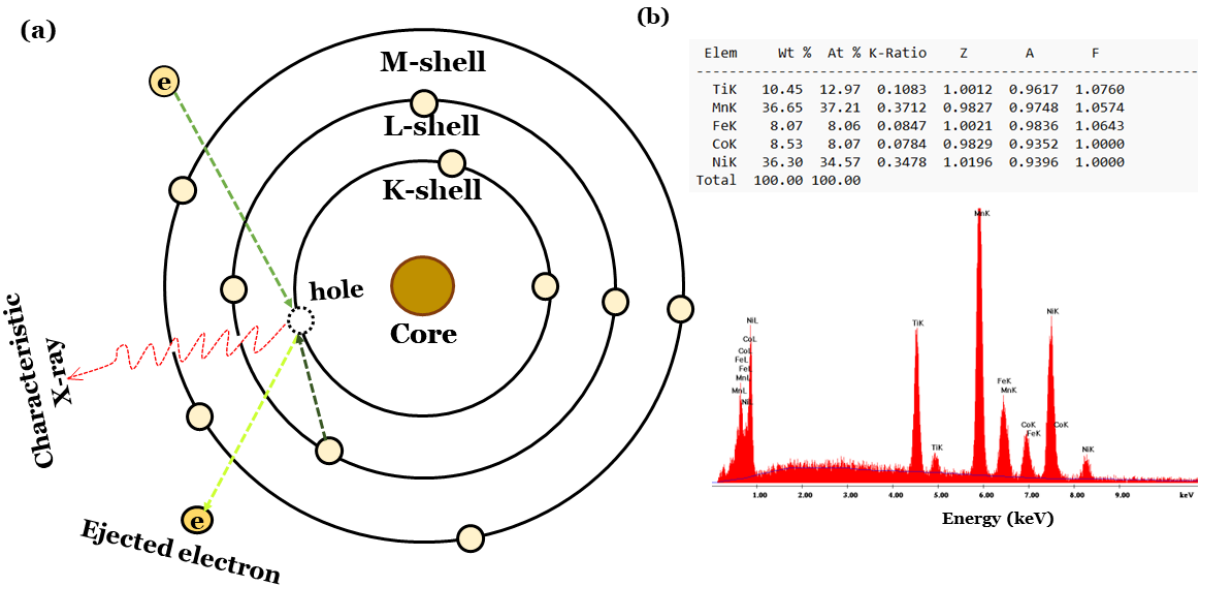

Figure 2.5: (a) Schematic of EDAX principle. (b) EDAX spectra for Ni-(FeCo)-Mn-Ti all-*d*-metal Heusler alloy.

2.3 Differential Scanning Calorimetry (DSC)

Differential Scanning Calorimetry (DSC) is a thermal analysis tool which measures physical properties like melting, boiling, glass transition and corresponding enthalpies of a material [8–10]. DSC determines the difference of heat flow between sample and references as a function of time and temperature under heating, cooling, or isothermal condition. DSC is first commercially introduced in 1970, and able to provide easily quantitative as well as qualitative data overall reaction kinetics with relative speed. DSC is divided into two basic types: heat-flux DSC and power compensation DSC. In our measurement, we used a commercially available Q2000^{TM} instrument, which works on the principle of heat-flux DSC, schematized in **Fig. 2.6(a)**.

In the heat-flux DSC, the sample and reference are connected through a low resistance heat flow path and heated by a single heater. When the heater is heated at a constant heat rate, its internal energy also changes. A temperature difference between sample and reference ($\Delta T=T_S-T_R$) is governed that is proportional to their differential heat flow rate ($\dot{q}$) by the Newton's law of cooling; $\frac{dq}{dt} = -k'\Delta T$, where k′ is the factory-installed calibration factor.

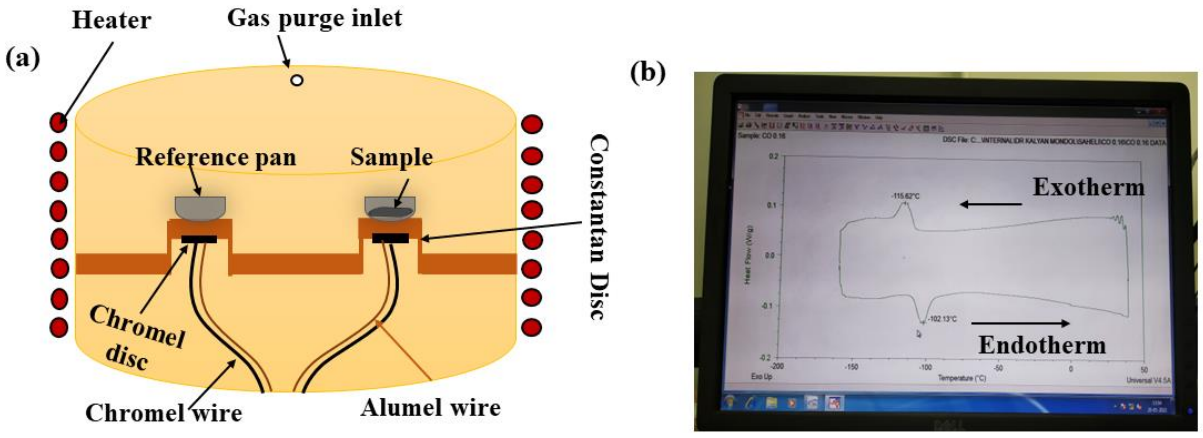

Figure 2.6: (a) Schematic diagram of heat-flux DSC. (b) Heat flow DSC curve vs temperature exhibiting structural transition temperature of Ni(Co)-Mn-Ti all-*d*-metal Heusler alloy.

Figure 2.6(b) shows DSC heat flow curve exhibiting the first order phase transition involving hysteresis between exothermic and endothermic curve of Ni(Co)-Mn-Ti all-*d*-metal Heusler alloy. Generally, we detect the characteristics temperatures of the martensitic transformation at a constant heat rate 10°C/min from DSC heat flow curve. The latent heat, enthalpy, specific

heat, and entropy associated with the transition have been calculated from the analysis of DSC curve.

2.4 Quantum design Physical Properties measurement System (PPMS)

Quantum design's Physical properties measurement system (PPMS) is equipped with a temperature control system and superconducting magnet, and allows the measurement of magnetization and electrical resistivity in the temperature range of 1.8-400 K with the maximum magnetic field of 9 T. The minimum pressure reached in the system is about 0.01mTorr.

2.4.1 Vibrating Sample Magnetometer (VSM)

The temperature and field dependent dc magnetization measurements are performed using a vibrating sample magnetometer (VSM) module in a 9T Dynacool PPMS, Quantum Design [11]. The VSM module of PPMS, in **Fig. 2.7(a)**, consists of a gradiometer pick-up coil detecting the response, a coil set puck for detection, a linear transport motor for vibrating the sample, and electronics set up for operating linear motor. The basic principle of VSM is established by the Faraday's law of induction, according to which induced voltage in the pick-up coil is proportional to the time derivative of magnetic flux through the coil. The induced voltage is given by

$$V_{coil} = -\frac{d\varphi}{dt} = -\left(\frac{d\varphi}{dz}\right)\left(\frac{dz}{dt}\right)$$

$$= \mathrm{CmA\omega Sin(\omega t)}$$

Where, C is the calibration constant which is used to calibrate the response, m is the magnetic moment of the sample, A is the amplitude of the sample, and $\omega = 2\pi f$, f is the frequency of oscillation of the sample. Electromagnetic field is generated by superconducting solenoid which has a vertical field. The output of the gradiometer pickup coil is connected to the preamplifier and VSM module is connected to a lock-in amplifier providing phase sensitive detection. Under a certain magnetic field, the moment is induced inside the material. A vertical sinusoidal mechanical oscillation is provided to the sample so that magnetic flux is enclosed with the help of pick-up coil as a function of time. The moment is measured as a function of time, magnetic field, and temperature.

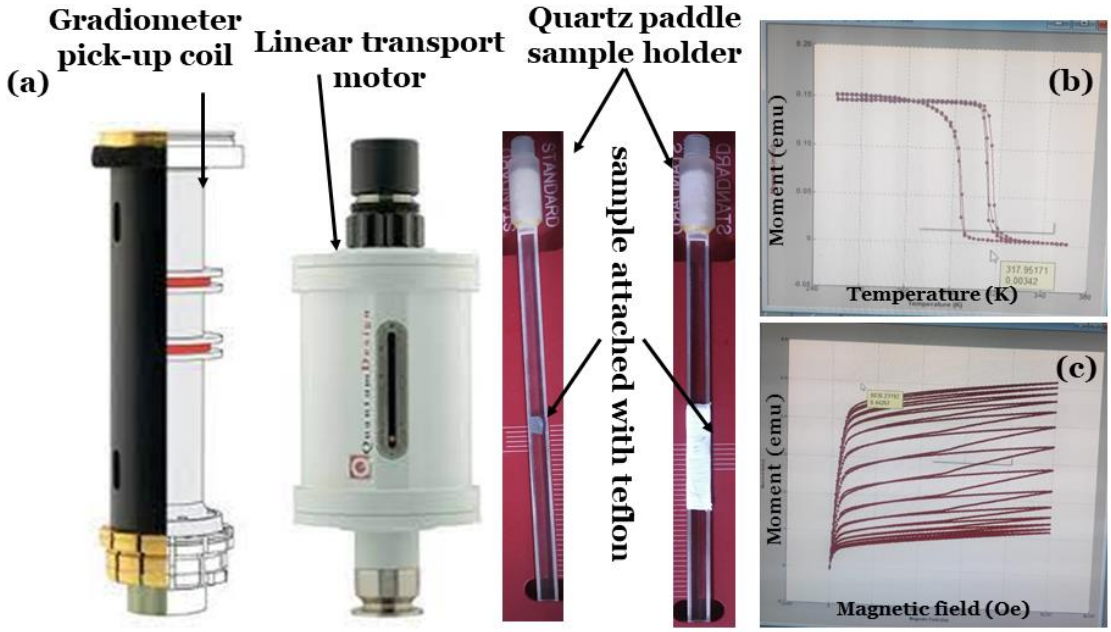

Figure 2.7: (a) Image of VSM module parts of PPMS and sample holder with attached sample for the magnetic properties measurement. (b) Temperature dependent magnetic moment at different rate, and (c) Field dependent moment of MnNiSi-based hexagonal system.

For the measurement, the investigating sample is usually rapped in a Teflon tape and attached in a non-magnetic quartz paddle-sample holder and then sample holder is mounted inside the chamber. Chamber is purged several times after the sample insertion process. Then the optimum position of the sample is set by scanning the output signal as a function of sample's position. Once the sample position is optimised, setup is ready for the measurement. During the measurement, sample vibrates vertically through the pick-up coil in steeps with the help of linear motor. Change in the sample position modifies the flux attached with the pick-up coil and demonstrates in the change of current flowing in the detection circuit. The magnetic moment is determined as the unit of emu by induced voltage with respect to the sinusoidal vibration. **Figure 2.7(b)** and **(c)** is associated with the temperature and field dependent magnetization data of our investigating MnNiSi-based system.

2.4.2 Electrical transport properties measurement

The electrical resistivity and magnetoresistance of the samples is measured in ac mode by standard four-probe method, illustrated in **Fig. 2.8(a)** [12]. First, sample is pasted on the mica sheet using GE varnish (good thermal conductor but bad electrical insulator) in **Fig. 2.8(b)**.

Four electrical contacts are made on top of the samples using thin copper wire (diameter ~ 120 μm) and conducting silver epoxy. 1st and 4th terminals act as a current source in which current is allowed to flow as well as voltage is measured between 2nd and 3rd probes. The ac resistivity of the samples is measured using the electrical transport option (ETO) of the above-mentioned system. A constant sinusoidal current of proper amplitude and of frequency 33.5 Hz was allowed to flow through the current leads and the ac voltage was measured across the voltage leads and amplified through a lock-in amplifier. And noise reduction is done using the lock-in amplifier and data averaging. The temperature-dependent electrical resistivity of the samples was recorded by PPMS Multiview software on a computer. The typical values of current for the electrical transport measurements were about 5 mA. The electrical resistivity (ρ) of the samples have been evaluated by using the following formula:

$$\rho = R\frac{A}{l},$$

Where l is the separation between the two voltage leads and A is the cross-sectional area of the samples. Temperature dependent resistivity curves under 0T and 5T is represented in **Fig.2.8(c)** for all-*d*-metal Ni(Co)-Mn-Ti system.

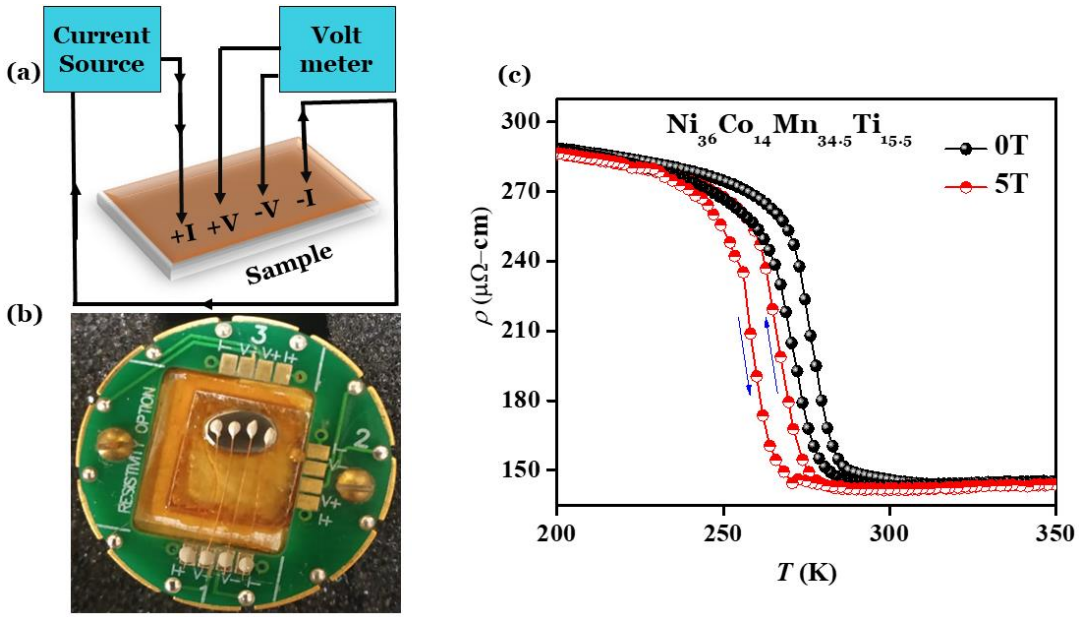

Figure 2.8: (a) Schematic of four probe setup for electrical resistivity measurement. (b) Corresponding photograph of puck used for mounting sample, and (c) Temperature dependent electrical resistivity of Ni(Co)-Mn-Ti all-*d*-metal Heusler alloy.

References:

[1] M. Ohring and A. Haldipur, *A Versatile Arc Melting Apparatus for Quenching Molten Metals and Ceramics*, Rev. Sci. Instrum. **42**, 530 (1971).

[2] S. Samanta, S. Ghosh, S. Chatterjee, and K. Mandal, *Large Magnetocaloric Effect and Magnetoresistance in Fe-Co Doped Ni50-(FeCo) Mn37Ti13 All-d-Metal Heusler Alloys*, J. Alloys Compd. **910**, 164929 (2022).

[3] P. B. Hirsch, *Elements of X-Ray Diffraction*, Phys. Bull. **8**, 237 (1957).

[4] J. C. Woolley, *Introduction to Solid State Physics*, J. Mech. Phys. Solids **6**, 83 (1957).

[5] D. McMullan, *Scanning Electron Microscopy 1928-1965*, Scanning **17**, 175 (2006).

[6] S. Guha, A. Bandyopadhyay, S. Das, and B. P. Swain, *Synthesis and Characterization of Titanium Silicon Nitride (TiSiN) Thin Film: A Review*, IOP Conf. Ser. Mater. Sci. Eng. **377**, 012181 (2018).

[7] M. Scimeca, S. Bischetti, H. K. Lamsira, R. Bonfiglio, and E. Bonanno, *Energy Dispersive X-Ray (EDX) Microanalysis: A Powerful Tool in Biomedical Research and Diagnosis*, Eur. J. Histochem. **62**, 89 (2018).

[8] C. H. Spink, *Differential Scanning Calorimetry*, in *Methods in Cell Biology*, Vol. 84 (2008), pp. 115–141.

[9] R. Volume, *2(t, /t(6.*, **123**, (1961).

[10] L. Zuo, X. Chen, S. Yu, and M. Lu, *Design and Fabrication of a Differential Scanning Nanocalorimeter*, J. Micromechanics Microengineering **27**, 025006 (2017).

[11] Q. Design, *Physical Property Measurement System Vibrating Sample Magnetometer (VSM) Option, User's Manual*, Design 152 (2008).

[12] J. H. Scofield, *Ac Method for Measuring Low-frequency Resistance Fluctuation Spectra*, Rev. Sci. Instrum. **58**, 985 (1987).

Chapter 3 Measurement Protocols dependent giant magnetocaloric Effect in MnNiSi-based system

Magnetothermal history is a crucial parameter for first-order phase transition material. If we determine the magnetocaloric properties by different procedure and compare together, they should not be same due to their history dependence. In this chapter, we have established an accurate and preferred measurement protocol to determine magnetocaloric effect precisely across the first-order phase transition in $(MnNiSi)_{0.835}(FeCoGa)_{0.165}$ *hexagonal system. Moreover, estimated magnetic entropy change using the Clausius-Clapeyron equation, Maxwell equation, the analysis of universal scaling behavior of the calculated* ΔS_M *data, and calorimetry study of magnetocaloric effect justifies the observations.*

Content of this chapter has been published in: S. Ghosh, S. Samanta, J. Sinha, and K. Mandal, " Measurement Protocols Dependent Giant Magnetocaloric Effect in MnNiSi-based system," Appl. Phys. Lett, 119, 183901(2021)

3 Measurement Protocol dependent giant magnetocaloric effect in MnNiSi-based system

3.1 Preface

Recent magnetic materials with combined structural and magnetic transition (known as magnetostructural transition, MST) from paramagnetic (PM) parent phase to ferromagnetic (FM) martensitic phase has gained enormous interest due to their magnetoresponsive properties [1–7]. Therefore, searching such material with MST near room temperature (RT) is an intensive research topic for magnetic refrigeration technology [8].

Recently, a family belonging to the Mn*M'X* (*M'* = Ni, Co, and *X* = Si, Ge) intermetallic compounds have grabbed significant attention to the scientific community as these materials exhibit MST near RT accompanied with a large unit cell volume changes as well as a jump in magnetization across the transition that results into a large MCE response [9–11]. In general, Mn*M'X* compounds in their stoichiometric form display a second-order magnetic transition followed by a first-order structural transformation from a low-temperature orthorhombic phase to a high-temperature hexagonal phase in the PM state without having a substantial change in magnetization. To make these materials useful for RT refrigeration technology, magnetic and structural transitions can be coupled at the same temperature which can lead to a first-order coupled MST associated with a sizeable change in magnetization across that transition. Because of cost of raw materials, MnNiSi system compared with the rest of the materials of Mn*M'X* family and other transition-metal-based magnetocaloric alloys is extremely cost-effective. The stoichiometric MnNiSi compound undergoes FM to PM transition at Curie temperature (T_C) ~ 622 K and above that temperature, a structural change from a TiNiSi-type orthorhombic structure to a Ni_2In-type hexagonal structure at T_M ~ 1210 K [12]. Therefore, to concurrently occur magnetic and structural transition in the vicinity of RT in MnNiSi compounds, two or more elemental substitutions [13,14], and alloying with binary or ternary compounds such as Fe_2Ge [15], FeCoGe [10], FeNiGe [9], FeCoGa [11], and MnFeGe [16] are found to be an effective method.

Generally, the use of Maxwell relation is a well-established method to explore the MCE response for these similar types of materials though the incorrect application of this relation overestimates the obtained magnetocaloric parameter [1,2,5,7]. It is known that the Maxwell relation is based on the equilibrium thermodynamic, i.e., magnetization and entropy are single-valued function of state. This is the appropriate treatment for the materials having a second-order magnetic transition (SOMT), but for the first-order MST, this analysis technique governs overestimation problem due to the magnetic and thermal hysteresis. This enables the existence of metastable along with the non-equilibrium state. Therefore, it is important to have correct and more reliable MCE parameters in such giant magnetocaloric materials across their MST, an error-free and reliable measurement protocol should be considered.

In this chapter, we have explored the MCE responses of $(MnNiSi)_{0.835}(FeCoGa)_{0.165}$ alloy using various measurement protocols. From our earlier studies, the MnNiSi system is observed to exhibit a MST in a well-regulated temperature regime of 224 K – 342 K when it is alloyed with FeCoGa for the composition of $(MnNiSi)_{1-x}(FeCoGa)_x$ (x = 0.15–0.17) alloys [11]. The present investigated system with x = 0.165 shows MST at about 265 K. MCE response of the system is deduced using the Maxwell equation from the measured isotherms in the vicinity of MST obeying discontinuous heating and cooling protocol. Further, the Clausius-Clapeyron equation is used to evaluate the MCE parameters from the isofield magnetization data. Moreover, the universal scaling behavior of the obtained data of the MCE parameter is analyzed to understand the effective method of measuring MCE response. The overall outcomes suggest that the discontinuous cooling mode is the preferred protocol to determine the MCE response of these similar types of materials accurately using the Maxwell relation.

3.2 Experimental

$(MnNiSi)_{0.835}(FeCoGa)_{0.165}$ alloy of approximately 2 g is prepared by conventional arc melting technique under a 4 N purity Argon atmosphere using high purity constituent elements from Sigma Aldrich. The sample is re-melted five to six times to ensure the homogenization. The as-cast sample is wrapped with a tantalum foil and sealed in a quartz tube under high vacuum and annealed at 1173 K. Past 4 days of heat treatment, the sample is quenched into ice water. X-ray diffraction (XRD) pattern of the sample is investigated using SmartLab9kW, Rigaku with Cu-K_α radiation. Magnetization measurements are performed in Vibrating Sample Magnetometer (VSM) using a physical property measurement system (PPMS, Quantum design). Temperature dependence of magnetization is carried out at a temperature ramp rate of 2 K/min. Differential scanning calorimetry (DSC) is performed to measure the heat flow curve of the sample with a heating/cooling.

3.3 Results and discussions

3.3.1 Temperature dependent Structural characterization

Figure 3.1 depicts the temperature dependent XRD pattern for $(MnNiSi)_{0.835}(FeCoGa)_{0.165}$ alloy. The sample at room temperature shows a purely hexagonal structure and no traces of orthorhombic structure is observed which indicates that the structural transformation temperature has been shifted to below *RT* from about 1210 K for the parent MnNiSi compound. The lattice parameters in the hexagonal phase are $a_h = 4.003$ Å and $c_h = 5.180$ Å. Temperature-dependent XRD pattern of this compound confirms the structural transformation of this sample from Ni_2In-type hexagonal to TiNiSi-type orthorhombic structure. The reduction of hexagonal distortion (c_h/a_h ratio) from about 1.636 for the parent MnNiSi compound [17] to 1.294 for the studied alloy stabilizes the hexagonal phase towards the lower temperature. At low temperatures, the sample crystallizes in a dominating orthorhombic phase, and the presence of few traces of hexagonal phase is attributed to inhibition of entire structural transformation which arises from the grinded sample.

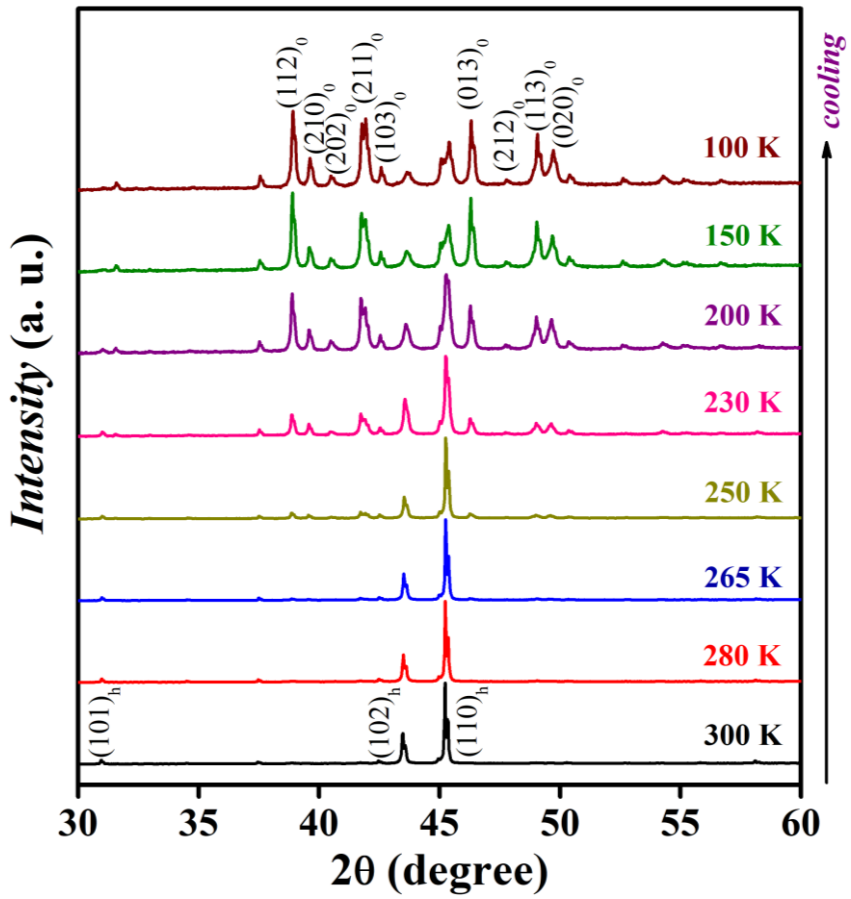

Figure 3.1: ***X***-ray diffraction pattern for $(MnNiSi)_{0.835}(FeCoGa)_{0.165}$ alloy at different temperatures.

3.3.2 Magnetic properties analysis

Figure 3.2(a) represents the temperature-dependent magnetization curve (M-T) under a low magnetic field of 0.05 T. M-T data are recorded on heating and subsequent cooling mode in presence of an applied field after cooling the sample to the desired temperature in zero fields cooled (ZFC) condition. It is seen that the alloy undergoes a MST from a high-temperature PM hexagonal phase to a low-temperature FM orthorhombic phase at T_t = 265 K during cooling. The presence of thermal hysteresis (ΔT_{hys}) of around 14 K during heating and cooling confirms the coupling of PM to FM transition and hexagonal to orthorhombic structural transition at the same temperature which leads to coupled first-order MST. The reverse transition takes place during heating at $T_t^{'}$ about 279 K. Further, M-T measurements are carried out at various applied magnetic fields following the above-mentioned way which are shown in **Fig. 3.2(b)**. The magnetic field usually favors to stabilize the magnetic phase with a higher magnetic moment and here it is the ferromagnetic orthorhombic phase.

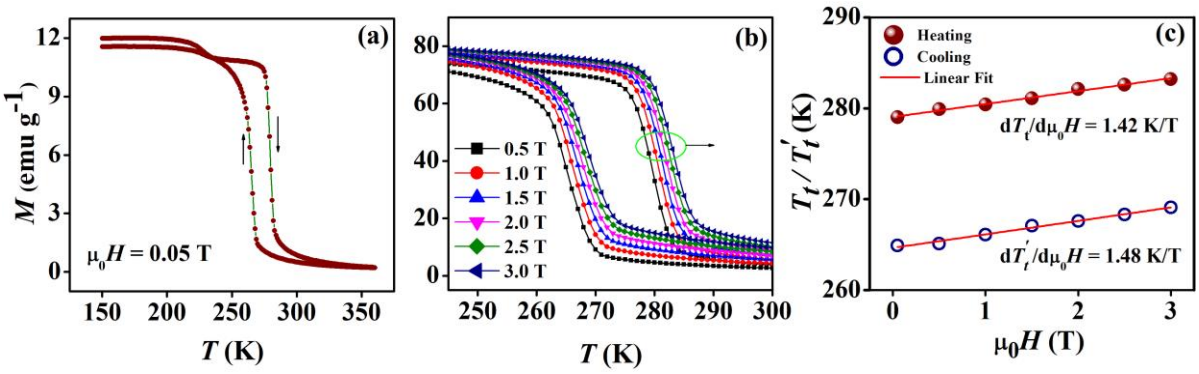

Figure 3.2: (a) M-T curve in presence of a low magnetic field of 0.05 T [Inset: dM /dT vs. T plots to deduce the structural transformation temperature during both heating and cooling] (b) M-T curves at the different applied magnetic field of 0.5, 1.0, 1.5, 2.0, 2.5 and 3.0 T (c) MST temperatures as a function of applied field for $(MnNiSi)_{0.835}(FeCoGa)_{0.165}$ alloy.

Hence, a shift of both T_t and $T_t^{'}$ is observed towards higher temperature with enhancing the applied field. ΔT almost remains constant with enhancing applied field. MST temperatures are plotted as a function of the applied field upon heating and on cooling in **Fig. 3.2(c)**. The sensitivity of transition temperature to the applied field is characterised by $dT_t/d\mu_0 H$ and $dT_t^{'}/d\mu_0 H$ which are +1.42 K/T and +1.48 K/T respectively. The obtained results is quite a weak field dependence of MST compared to other first-order magnetocaloric materials such as +4.9 K/T for $Gd_5Si_2Ge_2$ [18], +4.4 K/T for $LaFe_{11.6}Si_{1.4}$ [19], -8.5 K/T for $Fe_{49}Rh_{51}$ [20], +2.1 K/T for $MnFeP_{0.55}As_{0.45}$ [21], and -6.9 K/T for $Ni_{49.8}Mn_{35.0}In_{15.2}$ [22].

3.3.3 Thermal properties analysis

To detect the first-order structural transition by measuring the associated latent heat, DSC heat flow measurement is a powerful technique. **Figure 3.3(a)** carried out DSC heat-flow curve of the sample in heating as well as in cooling mode with a ramp rate of $dT/dt \pm 5$ K/min. On cooling, the transition takes place at $T_t \sim 264.6$ K where the peak of heat flow changes occurred during the transformation. The reverse transformation follows during heating at $T_t^{'}$ about 279.6 K. The presence of thermal hysteresis between heating and cooling mode confirms the transition is first-order in nature. We calculate the latent heat or the enthalpy change after the baseline correction and found to be about 10.62 J/g on cooling and ~13.21 J/g on heating. The change in total entropy at the structural transition is estimated following the equation,

$$\Delta S_{tr} = \int_{T_i}^{T_f} \frac{dQ}{dt}\left(\frac{dT}{dt}\right)^{-1}\frac{1}{T}dT \qquad (3.1)$$

where, dQ/dt is the heat flow changes of the sample. T_i and T_f are the starting and finishing temperatures of first-order phase transition respectively. The obtained ΔS_{tr} is found to be about 45.24 and ~ 47.36 $Jkg^{-1}K^{-1}$ during cooling and heating mode respectively.

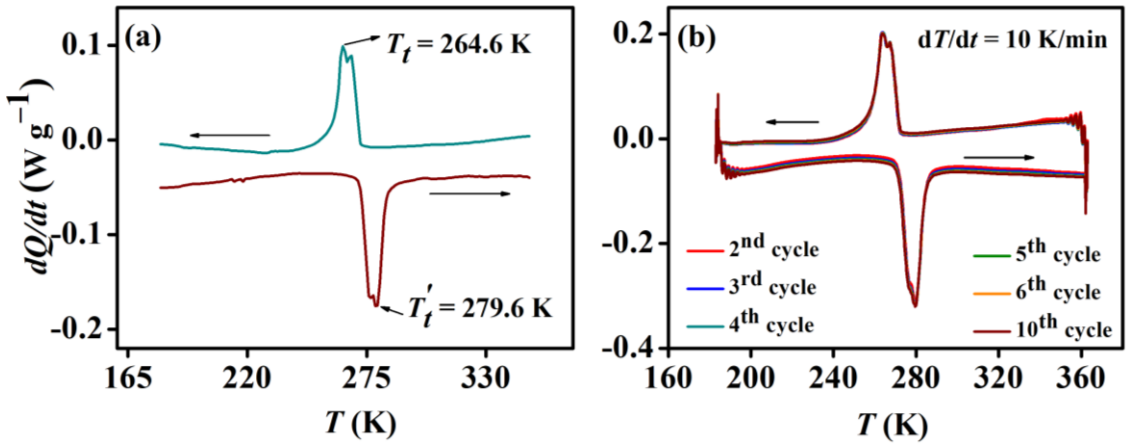

Figure 3.3 DSC heat flow curve for the investigating sample (a) at a heating/cooling rate of 5 K/min (b) several run up to 7th cycle at a heating/cooling rate of 10 K/min.

These types of materials exhibit remarkable structural changes during the thermal cycle across the MST which results in crack formation to the bulk sample and effectively reduces the mechanical stability of the sample. However, the physical properties remain unchanged after various thermal cycles, which have been examined by measuring several DSC heat flow run across the MST and is shown in **Fig. 3.3(b)**. This result indicates that despite of change in its mechanical properties due to repeated thermal cycles, the value of the transformation entropy change has no change. Noted that the MST temperatures and the width of thermal hysteresis also almost remain the same.

3.3.4 Field-dependent magnetization using heating and cooling protocol

Isothermal M-μ_0H curves are measured upon heating mode at a temperature interval of 2 K in the vicinity of T_t' for a maximum field change of 0-5 T which is shown in **Fig. 3.4(a)**. Isotherms are taken following discontinuous heating mode, where the sample is cooled to a reset temperature of 175 K (pure martensitic region) to record each M-μ_0H measurement. Surprisingly, M-μ_0H curves during heating do not exhibit any field-induced hysteresis which signifies that no first-order transition takes place on heating both in magnetic field increasing

and decreasing mode and it is unusual compared with the results obtained from M-T curves where the material shows clear thermal hysteresis across the transition. Here, 5 T magnetic fields are not sufficient to induce field-induced metamagnetic transition upon heating and hence, a very high magnetic field is necessary for that.

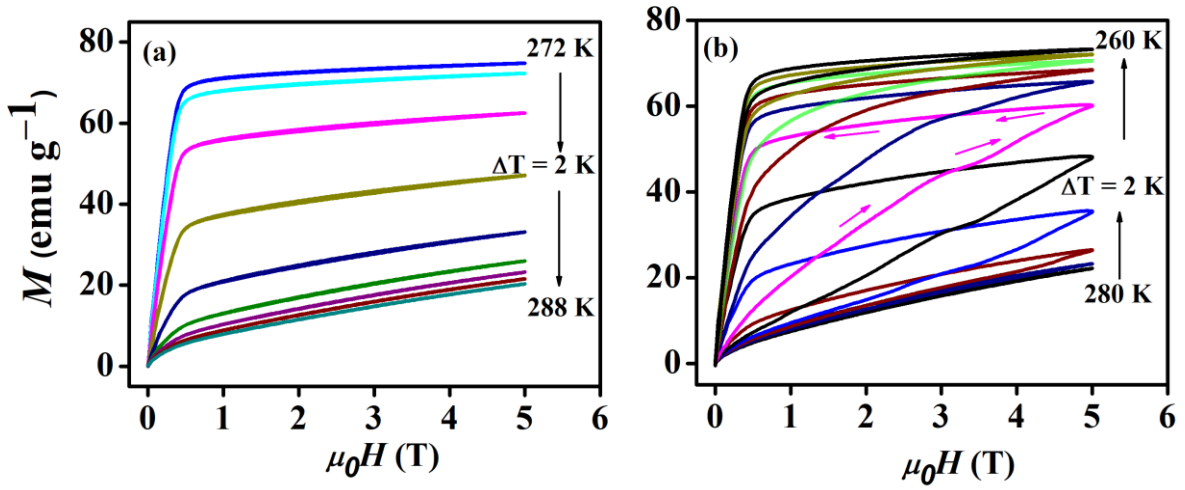

Figure 3.4: Isothermal M-μ_0H curves for $(MnNiSi)_{0.835}$ $(FeCoGa)_{0.165}$ alloy following (a) heating and (b) cooling mode.

Besides, isothermal M-μ_0H curves are measured following cooling mode in the temperature regime of 280 K -260 K at 2 K intervals each in the vicinity of T_t which is shown in **Fig. 3.4(b)**. To erase the field history effect of the sample, loop process methods [23,24] are used to measure the isotherms. Here, measurement protocol is as followed by **350 K → T_1(M-μ_0H) → 350 K→ T_2(M-μ_0H)** where T_1 and T_2 are the first temperature (for example 280 K for cooling mode), and the next target temperature higher than by 2 K of the previous one. It is seen that M-μ_0H curves exhibit field-induced hysteresis in the vicinity of transition temperature which is a signature of field-induced structural transition from PM to FM phase. Here, it can be noted that field-induced structural transition is realized during the field increasing mode only.

3.3.5 Isothermal magnetic entropy change

Isothermal magnetic entropy change (ΔS_M) is a crucial parameter to quantify the MCE response which provides an evidence of the viability of the sample as a magnetic refrigerant and is calculated using Maxwell equation from the measured isothermal M-μ_0H curves as [25],

$$\Delta S_M(T, \Delta H) = \mu_0 \int_0^H \left(\frac{\partial M(H,T)}{\partial T}\right)_H dH \quad (3.2)$$

The calculated ΔS_M values during both heating and cooling protocol (field increasing and decreasing mode) are shown in **Fig. 3.5(a)** and **3.5(b)**. On cooling protocol, ΔS_M reaches a maximum value of about 29.8 J kg^{-1} K^{-1} during the field increasing mode. On the other hand, ΔS_M is calculated on heating protocol which shows a maximum value of about 42.3 Jkg^{-1}K^{-1} due to a field change of 5 T for fields increasing mode. Here, we can see that M-μ_0H curves on cooling mode are pronounced to exhibit field-induced PM to FM transition in the vicinity of MST whereas, such kind of transition is not observed during heating protocol. The sample, in this case, resides either in FM/PM or in the mixed-phase of FM-PM throughout the isotherms measurements. Hence, temperature evolution of the FM phase give rises the unphysical overestimated ΔS_M value on heating protocol where ΔS_M values are much larger compared to the value of ΔS_M estimated from field increasing during cooling protocol. Moreover, field induced MST can be observed only during field increasing of cooling protocol, which is shown in **Fig. 3.5(a)** by drawing a line through connecting the peak values of ΔS_M for the different field changes.

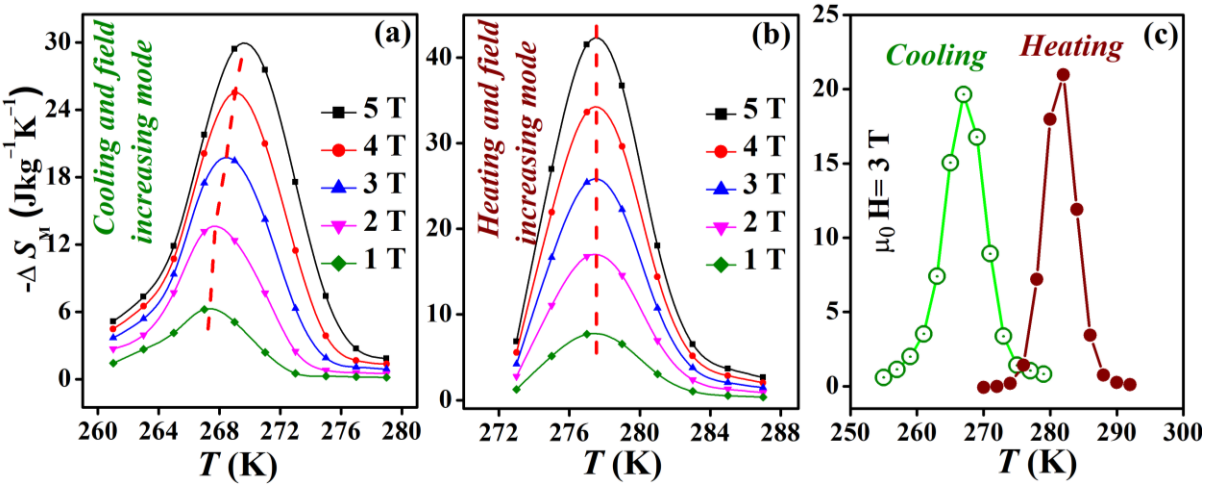

Figure 3.5: Magnetic entropy change (ΔSM) as a function of temperature estimated from isothermal M-H curves using Maxwell equation for (a) cooling and field increasing mode (b) heating and field increasing mode. ΔS_M as a function of temperature estimated from *M-T* curves following Clausius-Clapeyron equation during (c) heating mode and cooling mode. [The peak values of ΔS_M for the different field variations are connected by a line]

Therefore, the estimation of ΔS_M from magnetization during the field increasing of cooling protocol is a correct experimental protocol to obtain the MCE response of these similar types

of materials. A large change in magnetization across the MST originates from the lattice and magnetic structure changes, governs a giant MCE response in this system.

In order to further evidence the reliable protocol to use Maxwell equation for the estimation of ΔS_M, magnetic entropy change has been estimated using the Clausius-Clapeyron equation (CCE) which is appropriate for the first-order MST. The total magnetic entropy change can be estimated as, $\Delta S_M = -\Delta M \left(\frac{dT}{d\mu_0 H}\right)^{-1}$, where ΔM is the change in magnetization between FM and PM phases for a certain applied field. Total ΔS_M is found to be ~ -42.25 $Jkg^{-1}K^{-1}$ by adopting the value of ΔM about 60 emu/g and dT_t'/dH ~ 1.42 K/T during heating across MST, due to field changes from H_i ~ 50 mT to H_f ~ 3 T. Hence the obtained magnitude of ΔS_M using Maxwell equation from the magnetization during cooling and field increasing protocol is in the limit of total magnetic entropy change.

Further, the following equation based on the transformation fraction (TF-CCE) has been employed to deduce ΔS_M values from isofield *M-T* measurements for the different field changes on both heating and cooling mode [26],

$$\Delta S_M = -\Delta f \, \Delta M \left(\frac{dT_t}{d\mu_0 H}\right)^{-1} \quad \textbf{(3.3)}$$

where, Δf is the change of phase fraction induced by the change of magnetic field that can be defined as $\Delta f(T, \Delta H) = f(T, H_f) - f(T, H_i)$. $\mu_0 H_i$, and $\mu_0 H_f$, the initial and final applied magnetic field. The phase volume fraction is assumed as proportional to the total magnetization and thus, the phase fraction of the ferromagnetic orthorhombic phase can be estimated as [26]:

$$f(T) = \frac{M(T) - M_{LT}(T)}{M_{HT}(T) - M_{LT}(T)} \quad \textbf{(3.4)}$$

where, M_{LT} (T) and M_{HT} (T) represent the magnetization of the low-temperature phase (here, FM orthorhombic) and high-temperature phase (PM hexagonal) respectively.

ΔS_M has been calculated using equation (**3.3**) during both heating and cooling mode which is plotted in **Fig. 3.5(c)**. During heating across MST, ΔS_M is found to be ~ 20.97 $Jkg^{-1}K^{-1}$ due to field changes from H_i ~ 50 mT to H_f ~ 3 T whereas ΔS_M is observed to be around 19.65 $Jkg^{-1}K^{-1}$ during cooling mode due to the same field changes. The calculated values of ΔS_M during heating and cooling mode using transformation fraction-CCE equation are consistent with the measured ΔS_M value using Maxwell equation in the field increasing of cooling mode only which suggest that the estimation of ΔS_M using Maxwell equation from the isothermal *M-*

H curves during field increasing and cooling mode provide the accurate results in this similar type of systems.

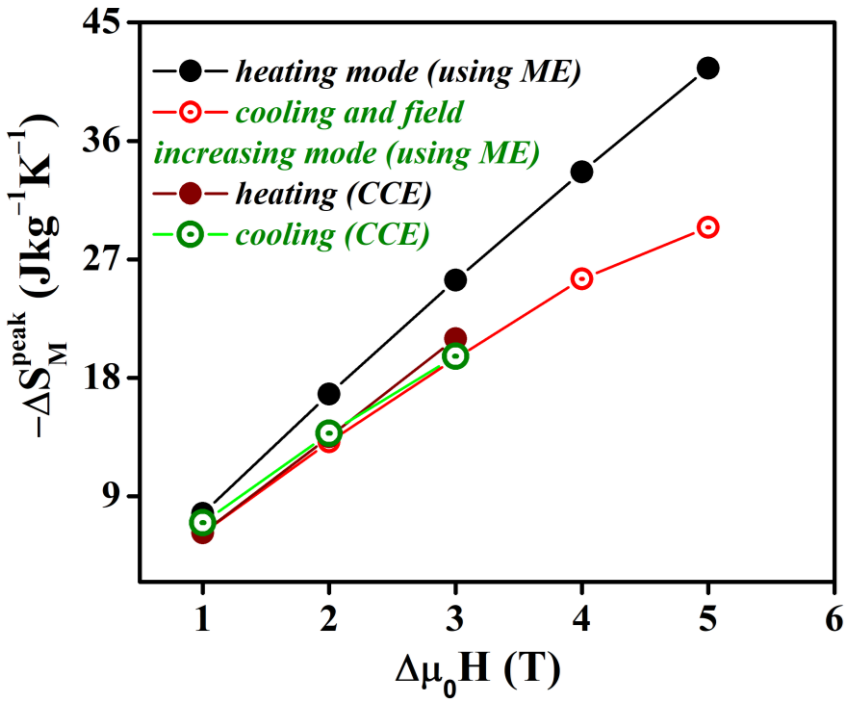

Figure 3.6: Comparison of the maximum value of ΔSM estimated using different methods (Maxwell equation is abbreviated as ME and Clausius-Clapeyron equation is abbreviated as CCE).

The deduced ΔS_M values from different measurement protocols are summarized in **Fig. 3.6**. ΔS_M values obtained from TF-CCE match well with ΔS_M value, obtained from Maxwell equation during cooling and field increasing mode. Importantly, during cooling mode, ΔS_M values shows a saturated tendency with the applied magnetic field and within the limit of transformation entropy changes from DSC heat flow measurement. In contrast, during heating mode, ΔS_M increases almost linearly with magnetic field and is supposed to exceed the limit of transformation entropy changes which is unphysical.

3.3.6 Universal Curve Fitting of MCE

Franco and Conde proposed a model to check the nature of magnetic phase transition by the evolution of MCE. According to this model, for 2nd –order phase transition all temperature-dependence entropy curves under different fields should collapse into a single universal curve [27]. In **Fig. 3.7**, the phenomenological universal graphs are plotted during both heating and cooling protocol (field increasing) by taking the normalized value of ΔS_M

using their respective peak of ΔS_M, defined as $\Delta S_M/\Delta S_M^{peak}$ and by rescaling the temperature (θ) using the following equation

$$\theta = \frac{T-T_{pk}}{T_r-T_{pk}} \quad \textbf{(3.5)}$$

where T_{pk} is defined as the temperature where the maximum of ΔS_M is obtained. T_r is selected as a temperature where $\Delta S_M(T_r) = 0.5\ \Delta S_M^{peak}$ above the peak temperature.

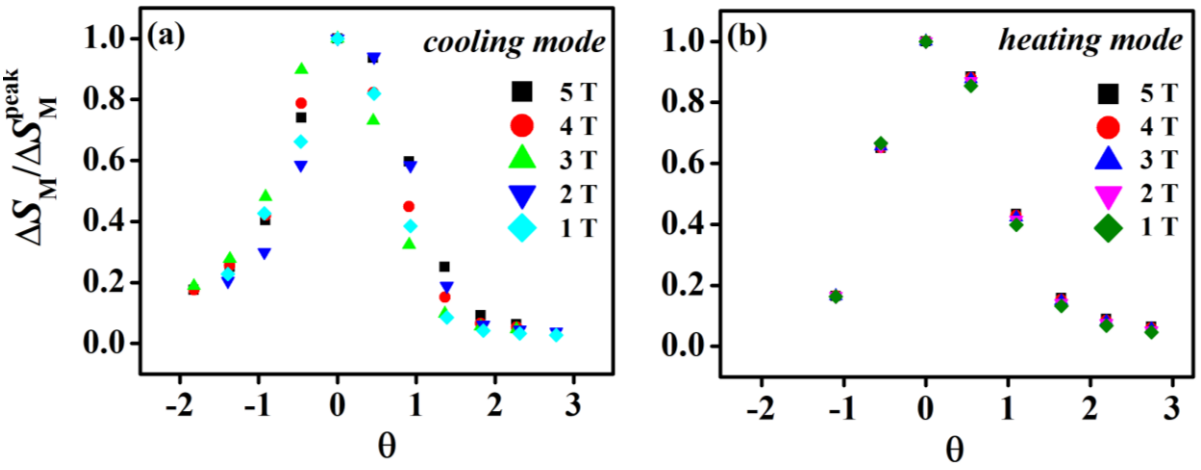

Figure 3.7: Universal curve for $(MnNiSi)_{0.835}(FeCoGa)_{0.165}$ alloy during (a) cooling and (b) heating protocol.

During the cooling mode of **Fig 3.7(a)**, all the normalized data are not well distributed but rather scattered in respect of rescaling temperatures which cannot be fitted in a single master curve and hence, the breakdown of the universal behavior is a signature of first-order type transition. In contrast, for heating protocol in **Fig 3.7(b)**, the normalized data for the different field variations are found to be well distributed and can be fitted in a single master curve which revealed the universal behavior of the alloy and the universality signifies the transition is of a second-order type. Hence, cooling and field increasing mode only shows first-order MST and the determination of MCE parameter will be trustworthy if it is measured following the mentioned protocol.

3.4 Conclusion

In summary, the magnetocaloric response of $(MnNiSi)_{0.835}(FeCoGa)_{0.165}$ alloy has been evaluated across the magnetostructural transformation from a high-temperature paramagnetic hexagonal structure to a low-temperature ferromagnetic orthorhombic structure. The material

shows ΔS_M as large as about 29.8 $Jkg^{-1}K^{-1}$ due to a field change of 5 T only. ΔS_M has been estimated using different measurement procedures and the use of Maxwell equation following discontinuous cooling protocol is found to be an effective method to determine the MCE response correctly. The estimated value of ΔS_M using transformation Clausius-Clapeyron equation, calorimetry study of MCE, and the breakdown of universal scaling behavior support the statement.

References:

[1] J. Liu, T. Gottschall, K. P. Skokov, J. D. Moore, and O. Gutfleisch, *Giant Magnetocaloric Effect Driven by Structural Transitions*, Nat. Mater. **11**, 620 (2012).

[2] V. K. Pecharsky and K. A. Gschneidner, Jr., *Giant Magnetocaloric Effect in Gd5(Si2Ge2)*, Phys. Rev. Lett. **78**, 4494 (1997).

[3] H. Wada and Y. Tanabe, *Giant Magnetocaloric Effect of MnAs1-XSbx*, Appl. Phys. Lett. **79**, 3302 (2001).

[4] J. Du, Q. Zheng, W. J. Ren, W. J. Feng, X. G. Liu, and Z. D. Zhang, *Magnetocaloric Effect and Magnetic-Field-Induced Shape Recovery Effect at Room Temperature in Ferromagnetic Heusler Alloy Ni–Mn–Sb*, J. Phys. D. Appl. Phys. **40**, 5523 (2007).

[5] T. Krenke, E. Duman, M. Acet, E. F. Wassermann, X. Moya, L. Manosa, and A. Planes, *Inverse Magnetocaloric Effect in Ferromagnetic Ni-Mn-Sn Alloys*, Nat. Mater. **4**, 450 (2005).

[6] A. Ghosh and K. Mandal, *Large Magnetic Entropy Change and Magnetoresistance Associated with a Martensitic Transition of Mn-Rich Mn50.5-XNi41Sn 8.5+x Alloys*, J. Phys. D. Appl. Phys. **46**, (2013).

[7] A. K. Nayak, K. G. Suresh, and A. K. Nigam, *Giant Inverse Magnetocaloric Effect near Room Temperature in Co Substituted NiMnSb Heusler Alloys*, J. Phys. D. Appl. Phys. **42**, 035009 (2009).

[8] V. Franco, J. S. Blázquez, J. J. Ipus, J. Y. Law, L. M. Moreno-Ramírez, and A. Conde, *Magnetocaloric Effect: From Materials Research to Refrigeration Devices*, Prog. Mater. Sci. **93**, 112 (2018).

[9] C. L. Zhang, D. H. Wang, Z. D. Han, B. Qian, H. F. Shi, C. Zhu, J. Chen, and T. Z. Wang, *The Tunable Magnetostructural Transition in MnNiSi-FeNiGe System*, Appl. Phys. Lett. **103**, 132411 (2013).

[10] T. Samanta, P. Lloveras, A. Us Saleheen, D. L. Lepkowski, E. Kramer, I. Dubenko, P. W. Adams, D. P. Young, M. Barrio, J. L. Tamarit, N. Ali, and S. Stadler, *Barocaloric and Magnetocaloric Effects in (MnNiSi) 1− x (FeCoGe) X*, Appl. Phys. Lett. **112**, 021907 (2018).

[11] S. Ghosh, A. Ghosh, P. Sen, and K. Mandal, *Giant Room-Temperature Magnetocaloric Effect Across the Magnetostructural Transition in (MnNiSi)1-x(FeCoGa)x Alloys*, Phys. Rev. Appl. **14**, 014016 (2020).

[12] V. Johnson and C. G. Frederick, *Magnetic and Crystallographic Properties of Ternary Manganese Silicides with Ordered Co2P Structure*, Phys. Status Solidi **20**, 331 (1973).

[13] J. Chen, H. G. Zhang, E. K. Liu, M. Yue, Q. M. Lu, W. H. Wang, G. H. Wu, and J. X. Zhang, *Wide Temperature Window of Magnetostructural Transition Achieved in Mn 0.4 Fe 0.6 NiSi 1−x Ga x by a Two-Step Isostructural Alloying Process*, AIP Adv. **6**, 056220 (2016).

[14] S. Ghosh, P. Sen, and K. Mandal, *Magnetostructural Transition and Large Magnetocaloric Effect in (Mn0.6Fe0.4)NiSi1−Al (x = 0.06–0.08) Alloys*, J. Magn. Magn. Mater. **500**, 166345 (2020).

[15] C. L. Zhang, H. F. Shi, E. J. Ye, Y. G. Nie, Z. D. Han, B. Qian, and D. H. Wang, *Magnetostructural Transition and Magnetocaloric Effect in MnNiSi-Fe2Ge System*, Appl. Phys. Lett. **107**, 2 (2015).

[16] T. Samanta, D. L. Lepkowski, A. U. Saleheen, A. Shankar, J. Prestigiacomo, I. Dubenko, A. Quetz, I. W. H. Oswald, G. T. McCandless, J. Y. Chan, P. W. Adams, D. P. Young, N. Ali, and S. Stadler, *Hydrostatic Pressure-Induced Modifications of Structural Transitions Lead to Large Enhancements of Magnetocaloric Effects in MnNiSi-Based Systems*, Phys. Rev. B **91**, 020401 (2015).

[17] Y. Li, Z. Y. Wei, E. K. Liu, G. D. Liu, S. G. Wang, W. H. Wang, and G. H. Wu, *Structural Transitions, Magnetic Properties, and Electronic Structures of Co(Fe)-Doped MnNiSi Compounds*, J. Appl. Phys. **117**, 17C117 (2015).

[18] T. Gottschall, K. P. Skokov, M. Fries, A. Taubel, I. Radulov, F. Scheibel, D. Benke, S. Riegg, and O. Gutfleisch, *Making a Cool Choice: The Materials Library of Magnetic Refrigeration*, Adv. Energy Mater. **9**, (2019).

[19] K. P. Skokov, K.-H. Müller, J. D. Moore, J. Liu, A. Y. Karpenkov, M. Krautz, and O. Gutfleisch, *Influence of Thermal Hysteresis and Field Cycling on the Magnetocaloric Effect in LaFe11.6Si1.4*, J. Alloys Compd. **552**, 310 (2013).

[20] A. Chirkova, K. P. Skokov, L. Schultz, N. V. Baranov, O. Gutfleisch, and T. G.

Woodcock, *Giant Adiabatic Temperature Change in FeRh Alloys Evidenced by Direct Measurements under Cyclic Conditions*, Acta Mater. **106**, 15 (2016).

[21] N. Ennassiri, N. Tahiri, O. El Bounagui, H. Ez-Zahraouy, and A. Benyoussef, *Structural, Electronic, Magnetic, and Magnetocaloric Properties in Metallic Antiperovskite Compound Mn3GaC*, Mater. Res. Bull. **98**, 335 (2018).

[22] T. Gottschall, E. Stern-Taulats, L. Mañosa, A. Planes, K. P. Skokov, and O. Gutfleisch, *Reversibility of Minor Hysteresis Loops in Magnetocaloric Heusler Alloys*, Appl. Phys. Lett. **110**, 223904 (2017).

[23] A. Ghosh, P. Sen, and K. Mandal, *Measurement Protocol Dependent Magnetocaloric Properties in a Si-Doped Mn-Rich Mn-Ni-Sn-Si off-Stoichiometric Heusler Alloy*, J. Appl. Phys. **119**, (2016).

[24] L. Caron, Z. Q. Ou, T. T. Nguyen, D. T. Cam Thanh, O. Tegus, and E. Brück, *On the Determination of the Magnetic Entropy Change in Materials with First-Order Transitions*, J. Magn. Magn. Mater. **321**, 3559 (2009).

[25] K. A. GschneidnerJr, V. K. Pecharsky, and A. O. Tsokol, *Recent Developments in Magnetocaloric Materials*, Reports Prog. Phys. **68**, 1479 (2005).

[26] K. Xu, Z. Li, Y.-L. Zhang, and C. Jing, *An Indirect Approach Based on Clausius–Clapeyron Equation to Determine Entropy Change for the First-Order Magnetocaloric Materials*, Phys. Lett. A **379**, 3149 (2015).

[27] V. Franco and A. Conde, *Scaling Laws for the Magnetocaloric Effect in Second Order Phase Transitions: From Physics to Applications for the Characterization of Materials*, Int. J. Refrig. **33**, 465 (2010).

Chapter 4 Giant room temperature magnetocaloric response in a $(MnNiSi)_{1-x}(FeNiGa)_x$ system

We design a new room temperature giant MCE material of $(FeNiGa)_x$ doped $(MnNiSi)_{1-x}$ system which yields a coupled magnetostructural transition (MST). The explicit dependence of the MST shifts with alloying has also been discussed. Through an optimum composition with x = 0.17, a giant MCE has been found in this Chapter.

Content of this chapter has been published in: S. Ghosh, **S. Samanta**, J. S. Mohanty, J. Sinha, and K. Mandal, "*Giant room temperature magnetocaloric response in a $(MnNiSi)_{1-x}(FeNiGa)_x$ system*," **J. Appl. Phys. 132, 045001 (2022).**

4 Giant room temperature magnetocaloric response in a $(MnNiSi)_{1-x}(FeNiGa)_x$ system

4.1 Preface

To prevent global warming and energy crisis, energy-efficient and eco-friendly technologies have attracted significant research interest in recent times. Solid-state-based magnetic refrigeration based on magnetocaloric effect (MCE) has massive potential to replace the conventional gas refrigeration system in cooling technology due to its various advantages such as higher energy conversion rate, environment-friendly, and the use of solid magnetic materials as magnetic refrigerant [1–3]. For an efficient and wide range of application landscape, magnetocaloric material should have a large value of magnetic entropy change (ΔS_M) in a low magnetic field. Therefore, the search of high potential magnetocaloric materials, following the observation of giant MCE response in $Gd_5Si_2Ge_2$ [4], several classes of materials such as $La(Fe, Si)_{13}$-based alloys [5–7], Mn-As-based alloys [6,8], Mn-Fe-based compounds [6], and Ni-Mn-based Heusler alloys [6,9–12] has been explicitly explored which are largely associated with a first-order magnetostructural transition (MST) near room temperature regime where both magnetic and structural transitions coincide at a particular temperature. However, the finding of such magnetocaloric materials containing low-cost and non-toxic elements and yielding large MCE response in a relatively lower applied magnetic field is a recent hot research topic. From the fundamental view point, it is known that the change in the unit cell volume ($\Delta V/V_0$) is related to the transformation entropy change (ΔS_{tr}) that can be expressed as $\Delta S_{tr} \approx \Delta S_{lat} + \Delta S_{mag} + \Delta S_{ele}$, where, ΔS_{lat}, ΔS_{mag}, and ΔS_{ele} are the lattice, magnetic, and electronic contribution, respectively. Across the transition, large $\Delta V/V_0$ leads to the stronger ΔS_{tr} (and hence ΔS_{lat}). Thus, a large magnetocaloric effect can be achieved where simultaneous unit cell volume change and magnetization change is observed.

Recently, Mn*M'X* (*M'* = Ni, Co, and *X* = Si, Ge) intermetallic compounds have grabbed significant attention due to their coupled MST near room temperature which is accompanied with a large change in unit cell volume and a jump in magnetization across the transition [13–

15]. Generally, stoichiometric Mn*M'X* compounds usually display a second-order magnetic transition followed by a first-order structural transition from a low-temperature TiNiSi-type orthorhombic to a high-temperature Ni_2In-type hexagonal phase in the paramagnetic (PM) state. Therefore, to use these materials for refrigeration technology, magnetic and structural transitions can be coupled near room temperature which can further lead to a first-order coupled MST associated with a large change in magnetization. In view of the cost of raw materials, MnNiSi system is extremely cost-effective compared to rest Mn*M'X*-based materials. However, the stoichiometric MnNiSi compound displays a ferromagnetic (FM) to PM transition at Curie temperature (T_C) ~ 622 K and subsequently, a structural transformation at T_M ~ 1210 K [16]. Hence, using two or more element substitutions in MnNiSi system, MST is successfully induced in the vicinity of room temperature which eventually shows giant MCE response around the transition [13–15,17–19].

In the previous chapter (**chapter 3**) we investigated that isostructural alloy doping in this MnNiSi system is an effective tool to achieve coupled MST around RT. We observed, that the use of Maxwell equation from isothermal M-μ_0H measurement during discontinuous cooling and field increasing mode, where the field-induced structural transition can be realized, provides only accurate results of MCE response in these materials. In all other cases, the continuous heating mode/ discontinuous heating mode, or discontinuous cooling and field decreasing mode inevitably result in the overestimation of measured MCE parameters.

In the present work, a coupled magnetostructural transition is realised in $(MnNiSi)_{1-x}$ system near room temperature through chemically doping with $(FeNiGa)_x$ for x = 0.16, 0.17, and 0.18. We have optimised x = 0.16, and 0.17 compositions where coupled MST is found. The structural transformation is noticed to shift at 317 K and 298 K for x = 0.16, and 0.17 respectively from T_M ~1210 K of the parent MnNiSi compound. MST is observed to be accompanied with a significant jump in unit cell volume and a sizeable change in magnetization. Therefore, a giant MCE response as ΔS_M of about 26.2 and ~ 63.2 $Jkg^{-1}K^{-1}$ for the alloys with x = 0.16 and 0.17 respectively is obtained due to a magnetic field change of 50 kOe only using the abovementioned measurement protocol. These materials containing low-cost and non-toxic elements are potential candidates for room-temperature solid-state-based MR technology.

4.2 Experimental

$MnNiSi)_{1-x}(FeNiGa)_x$ (x = 0.16,0.17, and 0.18) polycrystalline samples are prepared by arc melting technique under a 4 N purity Argon atmosphere using high purity constituent elements from Sigma Aldrich. The samples are re-melted five to six times to ensure homogenization. The as-cast sample is wrapped with a tantalum foil and sealed in a quartz tube under a high vacuum and annealed at 1173 K. Past 4 days of heat treatment, the sample is quenched into ice water. X-ray diffraction (XRD) patterns of the samples are investigated using SmartLab9kW, Rigaku with Cu-K_α radiation. Magnetic measurements are performed in a vibrating sample magnetometer (VSM) using physical property measurement system (PPMS, Quantum design). Differential scanning calorimetry (DSC) is performed to measure the heat flow curve of the sample with a constant heating/cooling rate of 10 K/min.

4.3 Results

4.3.1 Composition optimization from magnetic measurement

Magnetization vs. temperature (M-T) curves are recorded during zero field cooled (ZFC) and FC conditions in presence of 500 Oe magnetic field and plotted in **Fig. 4.1** for all the prepared samples. The presence of thermal hysteresis (ΔT_{hys}) between heating and cooling curve, confirms the coupling of magnetic and structural transitions along with a sharp change in magnetization from FM to PM which leads to a first-order MST. One can see that on cooling, the MST occurs from PM hexagonal to FM orthorhombic phase at T_t ~ 317 K and 298 K respectively for x = 0.16 and 0.17 alloys and the reverse transition takes place during heating at T_t' ~ 339 K and 315 K for the alloys with x = 0.16 and 0.17 respectively. On the other hand, from M-T curve that unlike other samples, x = 0.18 does not experience coupled MST, rather exhibits a structural transition T_t ~ 201 K followed by a magnetic transition ~220 K on temperature decreasing. On the other hand, 5 T magnetic field produces a weak MST for x = 0.18, as shown in the inset of **Fig. 4.1**. ΔT_{hys} is observed to reduce from 22 K, 17 K, and 16 K with increasing x content from 0.16 to 0.18. Therefore, considering the advantage of MST, we focus on particularly x = 0.16 and 0.17 samples for further measurements.

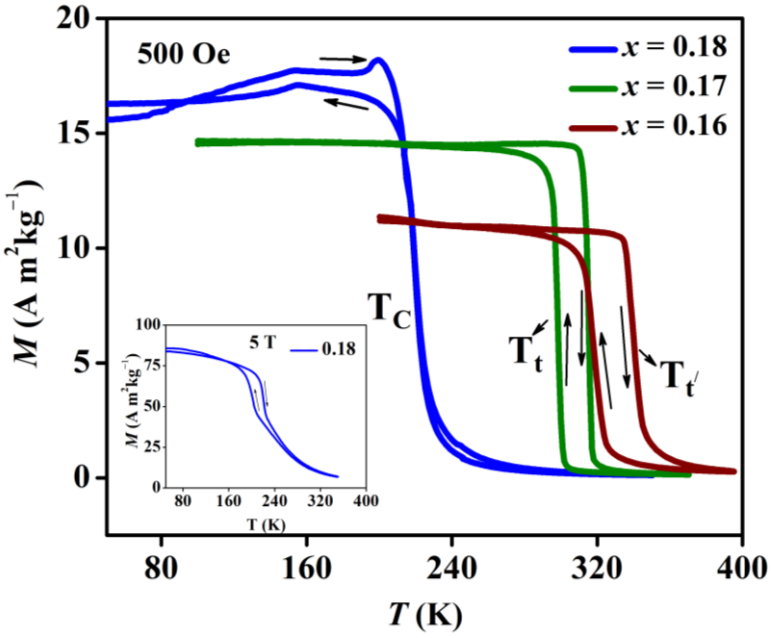

Figure 4.1: Temperature-dependent magnetization curve under 500 Oe for the present alloys. [Inset shows MT-curve of 0.18 sample taken 5 T.

4.3.2 Structural characterization

XRD patterns are shown for $(MnNiSi)_{1-x}(FeNiGa)_x$ (x = 0.16 and 0.17) samples at room temperature which is shown in **Fig. 4.2(a)**. Both the samples exhibit a mixed phase of orthorhombic and hexagonal structure which suggest that structural transition drastically reduces from a high temperature of 1210 K for MnNiSi parent compound to around room temperature with $(FeNiGa)_x$ doping. The increase of hexagonal phase volume fraction volume with increase in x concentration indicates the shifting of T_M towards lower temperature with increasing $(FeNiGa)_x$ percentage. Structural refinement of the XRD data is done using the Rietveld profile refinement method in "FULLPROF" software. The obtained lattice parameters for x = 0.16 in the dominating orthorhombic phase are a_{ortho} = 5.821 Å, b_{ortho} = 3.666 Å, c_{ortho} = 6.962 Å and in the hexagonal phase are a_{hexa} = 4.006 Å and c_{hexa} =5.207Å whereas, for the alloys with x = 0.17, the lattice parameters in the dominating hexagonal phase are a_{hexa} = 4.005 Å and c_{hexa} = 5.197 Å and in the orthorhombic phase are a_{ortho} = 5.802 Å, b_{ortho} = 3.661 Å and c_{ortho} = 6.952 Å.

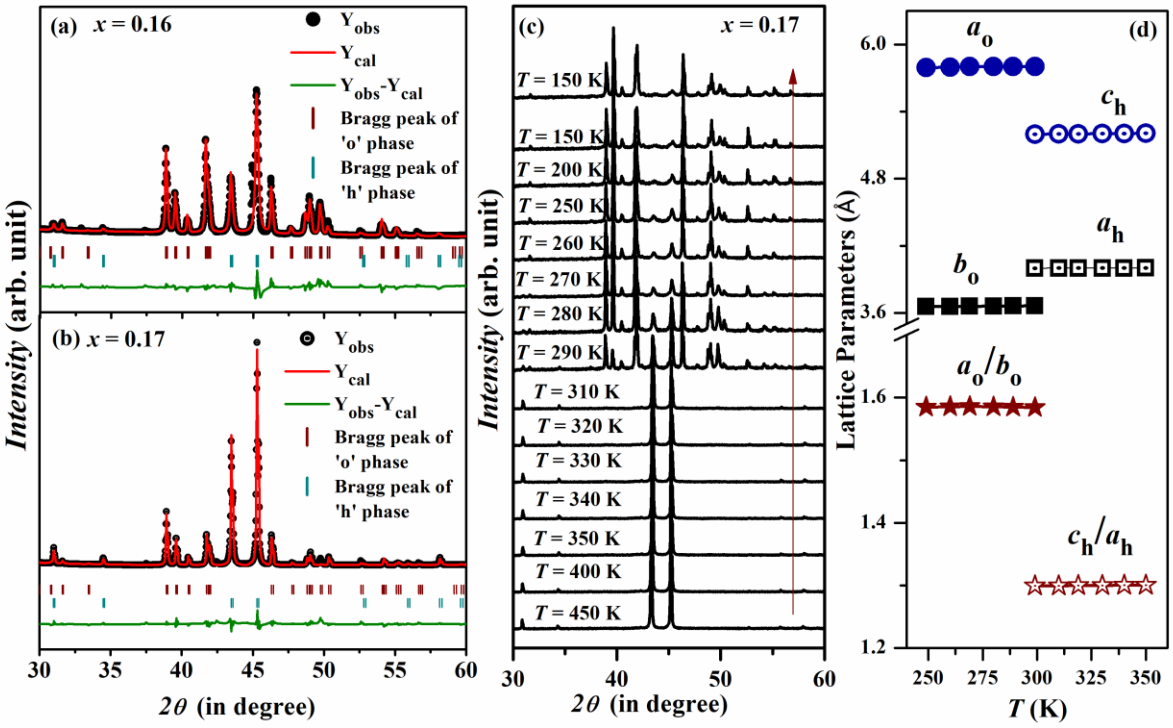

Figure 4.2: Rietveld profile refinement of XRD pattern of powder samples of (MnNiSi)1-*x*(FeNiGa)*x* alloys with (a) $x = 0.16$ and (b) $x = 0.17$ at room temperature (~ 300 K). [hexagonal and orthorhombic phase are denoted as 'h' and 'o' respectively] (c) Temperature-dependent XRD pattern at various temperatures for the sample with $x = 0.17$ recorded during cooling. (d) Lattice parameters, estimated from Rietveld profile refinement, as a function of temperatures.

From the crystallographic relation between hexagonal and orthorhombic phase, the TiNiSi-type structure is considered as an orthorhombic distortion of Ni_2In-type hexagonal structure. Hence, the reduction in the degree of hexagonal distortion (c/a ratio of hexagonal phase) with the increase in *x* content stabilizes the hexagonal phase towards lower temperature. The similar justification is found well in *MnM'X* -based compounds.

We have also carried out the temperature-dependent XRD pattern of $x = 0.17$ alloy during cooling for various temperatures as shown in **Fig. 4.2(b)** and corresponding lattice parameters of both phases as a function of temperature are plotted in **Fig. 4.2(c)**. It is seen that the structural transition from a high temperature dominating hexagonal to a low temperature orthorhombic structure is associated with a significant change a_{ortho} and b_{ortho}. Therefore, a large unit cell volume change 2.6% is observed for $x = 0.17$. A little trace of hexagonal phase in

orthorhombic phase can be attributed due to the inhibition of entire structural transformation originating from the ground sample.

4.3.3 Realization coupled MST from DSC and MT curve

M-T curves for all the optimised alloys are recorded in presence of 5 T magnetic field, shown in **Fig. 4.3(a)**. Usually, magnetic field stabilizes the magnetic phase with higher magnetic ordering. Here the FM orthorhombic phase stabilizes with increase in magnetic field and hence, a shifting of T_t can be observed toward higher temperature with a rate of $dT/d\mu_0 H$ = 1.4 K/T for both alloys. From **Fig. 4.3(a)** one can notice that, during MST that a big change in magnetization of about 63.9 and 73.15 emu/g for x = 0.16 and 0.17 is observed. Moreover, the saturation magnetization (M_S) of the samples enhances with the doping content which can be due to the reduction of hexagonal distortion with FeNiGa doping.

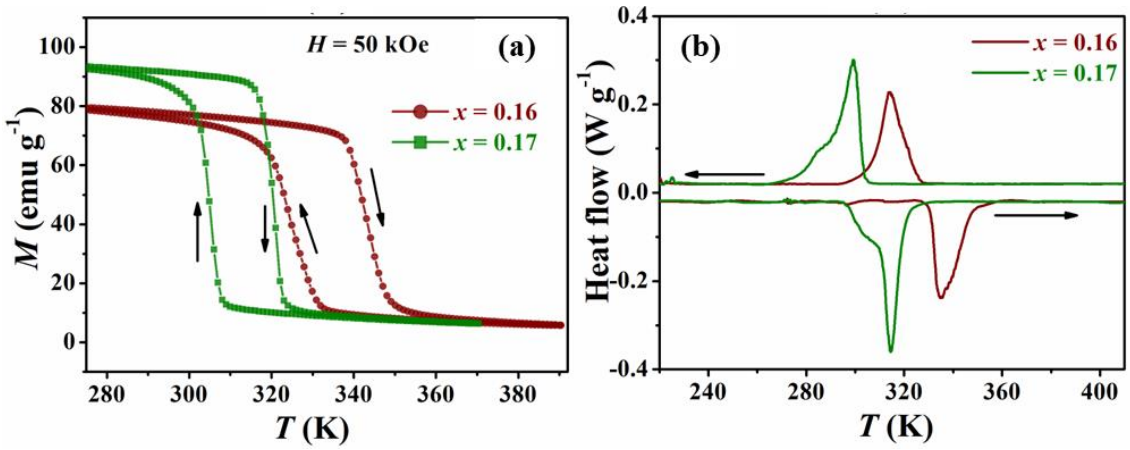

Figure 4.3: Temperature-dependent magnetization curve under 500 Oe for the present alloys. [Inset shows M-T-curve of 0.18 sample taken 5 T].

DSC heat flow curves of the samples are carried out during heating and cooling cycles as shown in **Fig. 4.3(b)**. The structural transition is realized during cooling at T_t ~ 317 K and 299 K for the alloys with x = 0.16 and 0.17 respectively (well consistent in M-T curve), where the maximum heat flow changes occur and the reverse transition takes place during heating. The associated latent heat during structural transition and the presence of thermal hysteresis signifies the first order nature of MST. ΔS_{tr} of these alloys across first-order structural transition during cooling are measured following the equation,

$$\Delta S_{tr} = \int_{T_i}^{T_f} \frac{dQ}{dt}\left(\frac{dT}{dt}\right)^{-1}\frac{1}{T}dT \qquad (4.1)$$

where dQ/dt refers to the heat flow changes of the sample. T_i and T_f are the starting and finishing temperatures of first-order phase transition respectively. The calculated ΔS_{tr} is found to be about 45.7 and ~ 66.9 $Jkg^{-1}K^{-1}$ for the alloys with x = 0.16 and 0.17 respectively.

4.3.4 Magnetocaloric properties

4.3.4.1 Magnetic entropy change

Isothermal magnetization vs. magnetic field (M-μ_0H) curves are carried out at different temperatures in the vicinity of T_t for the samples with x = 0.16 and 0.17 following the loop process method and plotted in **Fig. 4.4(a)** and **4.4(b)**. The protocol, already described in the **chapter 3**, is used to record each isothermal M-μ_0H measurement. The presence of magnetic hysteresis in the M-μ_0H plot confirms the field induced first-order MST from PM to FM phase during field increasing mode.

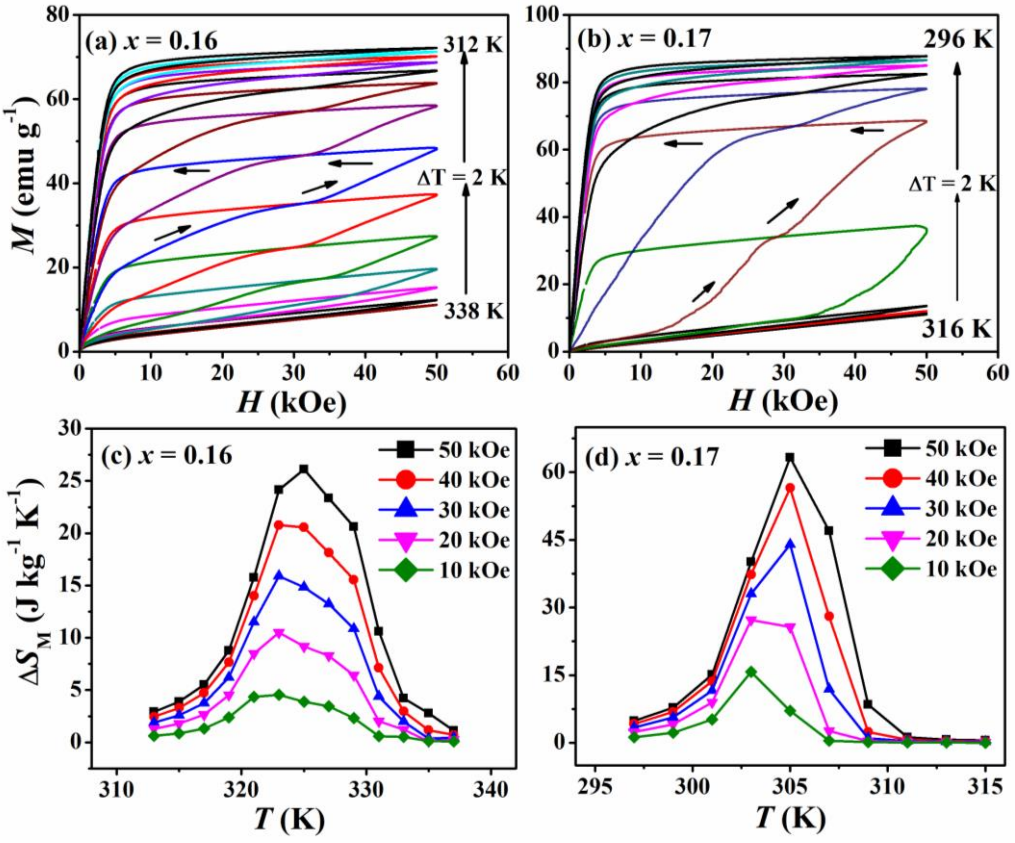

Figure 4.4: Isothermal M-μ_0H curves across T_t for the alloys with (a) x = 0.16, and (b) x = 0.17, recorded during discontinuous cooling protocol. Magnetic entropy change (ΔS_M) vs. temperature for the different field variations for the alloys with (c) x = 0.16 and (d) x = 0.17.

To know the viability of the investigated materials as a magnetic refrigerant, isothermal magnetic entropy change (ΔS_M) is computed using Maxwell equation from isothermal M-μ_0H curves as, $\Delta S_M(T, \Delta H) = \mu_0 \int_0^H \left(\frac{\partial M(H,T)}{\partial T}\right)_H dH$. ΔS_M has been estimated from isothermal M-μ_0H curves measured during cooling and field increasing protocol and plotted as a function of temperatures for the different field variation as shown in **Fig. 4.4(c)** and **4.4(d)**. The ΔS_M is found to be as large as about 26.2 Jkg^{-1}K^{-1} at a peak temperature of T_p ~ 323 K and ~ 63.2 Jkg^{-1}K^{-1} at T_p ~ 305 K due to application of 5 T magnetic field. Moreover, these materials show large MCE response in relatively low applied magnetic field where ΔS_M is about 10.5 and ~27.2 Jkg^{-1}K^{-1} for the field changes of 2 T. Thus, this giant MCE originates at magnetostructural transition that modifies the magnetic exchange interactions through the change in the lattice parameters. **Table 4.I** compares the peak value of ΔS_M at 5 T of $(MnNiSi)_{1-x}(FeNiGa)_x$ (x = 0.16 and 0.17) and other related promising systems. ΔS_M of the present system is the highest value among the reported other promising systems. Compared to the other Mn*M'X* -based magnetocaloric compounds such as MnCoGe-based systems, MnFeGe-based systems, and NiCoGe-based systems, our investigated MnNiSi systems contain Ge-free element and consist of a relative lower concentration of Ga, which make the present systems much more cost effective and suitable for magnetic refrigeration technology.

Table 4.I: Comparison of ΔS_M at 5 T and their respective transition temperatures of $(MnNiSi)_{1-x}(FeNiGa)_x$ compound, and other related compounds and alloys.

Materials	$\lvert\Delta S_M^{peak}\rvert$ **(J kg^{-1}K^{-1})**	**T^{peak} (K)**	**References**
$LaFe_{11.7}Si_{1.3}$	25	188	[20]
$LaFe_{11.2}Co_{0.7}Si_{1.1}$	12.5	274	
$LaFe_{11.6-x}Cr_xSi_{1.4}$			[21]
***x* = 0**	23.5	191	
***x* = 0.12**	22	189	
***x* = 0.21**	21.5	185	
***x* = 0.35**	17.5	178	
$LaFe_{11.5}Si_{1.5}H_{0.9}$	16.9	272	

$LaFe_{11.5}Si_{1.5}H_{1.3}$	17	288	[22]
$LaFe_{11.5}Si_{1.5}H_{1.5}$	16.8	312	
$La(Fe_{0.97}Mn_{0.03})_{11.7}Si_{1.3}H_{\delta}$	15.9	287	[23]
$La(Fe_{0.98}Mn_{0.02})_{11.7}Si_{1.3}H_{\delta}$	17.7	312	
$La(Fe_{0.92}Si_{0.08})_{11.9}Si_{1.1}$	15.6	301	[24]
$MnFeP_{0.45}As_{0.55}$	18	308	[25]
$(MnNiSi)_{1-x}(FeCoGa)_x$			[26]
x =0.15	25	323	
x =0.16	31.1	281	
x =0.17	23.8	313	
$Ni_{50}Mn_{37}Sn_{13}$	18	299	[27]
$Ni_{40}Mn_{10}Mn_{40}Sn_{10}$	14.9	288	[28]
$(MnNiSi)1-x(FeCoGa)x$			***Present work***
x =0.16	26.2	323	
x =0.17	63.2	305	

4.3.4.2 Relative cooling power

Apart from ΔS_M, relative cooling power (RCP) is another key parameter to evaluate MCE response of the investigated materials that defines the cooling efficiency as a magnetic refrigerant and it can be calculated from the temperature-dependent ΔS_M plot following the equation as,

$$RCP = \Delta S_M^{peak} \times \Delta T_{FWHM} \quad \textbf{(4.2)}$$

where, ΔS_M^{peak} represents the peak value of ΔS_M from the ΔS_M-T curve (in **Fig. 4.4(c)-(d)**) and ΔT_{FWHM} is the temperature region of the full width at half maxima (FWHM) of the same curve.

The materials with x = 0.16 and 0.17 have large RCP of about 268.8 and ~ 357.1 J/kg respectively upon 5 T whereas, for the field changes of 2 T the values of RCP are 107.1 and 122.4 J/kg. order to evaluate the utility of these materials in refrigeration technology, average magnetic hysteresis loss (HL) during field sweeping is need to be subtracted from the calculated RCP value to obtain their net RCP as magnetic refrigerant. HL is estimated as a function of temperature from the isothermal *M-H* curves using the equation, $HL = \mu_0 \int_0^{H_{max}} \left| M_{H_{increase}} - M_{H_{decrease}} \right|_H dH$, which is shown below. Integrating over the FWHM of the HL−T plot, an average HL is obtained. The average HL is found to be 48.7 and 92.5 J/kg for the alloys with x = 0.16 and 0.17 respectively which in turn provide the net RCP as 220.1 and 264.5 J/kg respectively.

4.3.4.3 Adiabatic temperature change

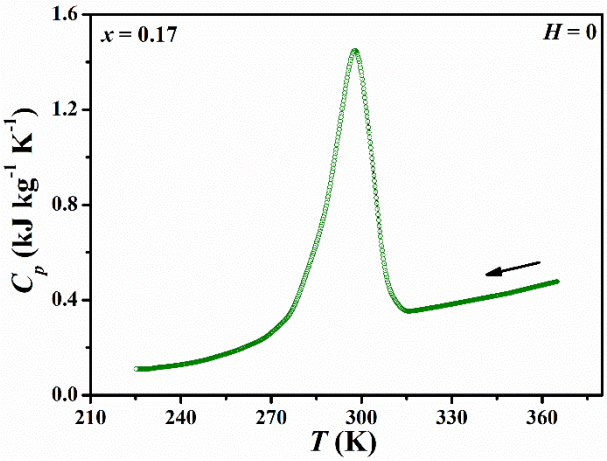

Figure 4.5: Specific heat capacity (c_p) as a function of temperature under zero field for the alloy with x = 0.17 recorded during cooling mode.

Further, for the alloy with x = 0.17, we have estimated another straightforward parameter of MCE, adiabatic temperature change (ΔT_{ad}) of the material, indirectly through measuring temperature dependent specific heat capacity (c_p) following the equation, $\Delta T_{ad} = -\frac{T}{c_p} \times \Delta S_M$. c_p has been recorded in zero field condition using modulated DSC technique as shown in **Fig. 4.5**. The peak of ΔT_{ad} is estimated from the deduced ΔS_M using peak value of zero field c_p = 1448 $Jkg^{-1}K^{-1}$ at 298 K where the field dependency of c_p is neglected and found to be about ~ 13 K due to a magnetic field change of 5 T which is certainly a large value compared to the other reported materials in literature.

4.4 Conclusions

In summary, magnetostructural transition from high temperature paramagnetic hexagonal to low temperature ferromagnetic orthorhombic phase is established in $(FeNiGa)_x$ (x = 0.16 and 0.17) doped $(MnNiSi)_{1-x}$ compound. The structural transition is shifted with x doping around room temperature from a very high temperature~ 1210 K of the parent MnNiSi system. The studied low-cost materials exhibit giant isothermal magnetic entropy change of 26.2 and ~ 63.2 $Jkg^{-1}K^{-1}$, associated with a large relative cooling power of ~ 268.8 and ~ 357.1 J/kg respectively in the vicinity of room temperature due to field change of 5 T only which enable them potential candidates for room temperature magnetic refrigeration technology.

References:

[1] K. A. GschneidnerJr, V. K. Pecharsky, and A. O. Tsokol, *Recent Developments in Magnetocaloric Materials*, Reports Prog. Phys. **68**, 1479 (2005).

[2] O. Gutfleisch, M. A. Willard, E. Brück, C. H. Chen, S. G. Sankar, and J. P. Liu, *Magnetic Materials and Devices for the 21st Century: Stronger, Lighter, and More Energy Efficient*, Adv. Mater. **23**, 821 (2011).

[3] T. Gottschall, K. P. Skokov, M. Fries, A. Taubel, I. Radulov, F. Scheibel, D. Benke, S. Riegg, and O. Gutfleisch, *Making a Cool Choice: The Materials Library of Magnetic Refrigeration*, Adv. Energy Mater. **9**, (2019).

[4] V. K. Pecharsky and K. A. Gschneidner, Jr., *Giant Magnetocaloric Effect in Gd5(Si2Ge2)*, Phys. Rev. Lett. **78**, 4494 (1997).

[5] L. Jia, J. R. Sun, J. Shen, Q. Y. Dong, J. D. Zou, B. Gao, T. Y. Zhao, H. W. Zhang, F. X. Hu, and B. G. Shen, *Magnetocaloric Effects in the La (Fe,Si) 13 Intermetallics Doped by Different Elements*, J. Appl. Phys. **105**, 7 (2009).

[6] V. Franco, J. S. Blázquez, J. J. Ipus, J. Y. Law, L. M. Moreno-Ramírez, and A. Conde, *Magnetocaloric Effect: From Materials Research to Refrigeration Devices*, Prog. Mater. Sci. **93**, 112 (2018).

[7] O. Gutfleisch, T. Gottschall, M. Fries, D. Benke, I. Radulov, K. P. Skokov, H. Wende, M. Gruner, M. Acet, P. Entel, and M. Farle, *Mastering Hysteresis in Magnetocaloric Materials*, Philos. Trans. R. Soc. A **374**, 20150308 (2016).

[8] H. Wada and Y. Tanabe, *Giant Magnetocaloric Effect of MnAs1-XSbx*, Appl. Phys. Lett. **79**, 3302 (2001).

[9] T. Krenke, E. Duman, M. Acet, E. F. Wassermann, X. Moya, L. Manosa, and A. Planes, *Inverse Magnetocaloric Effect in Ferromagnetic Ni-Mn-Sn Alloys*, Nat. Mater. **4**, 450 (2005).

[10] A. Ghosh and K. Mandal, *Large Magnetic Entropy Change and Magnetoresistance Associated with a Martensitic Transition of Mn-Rich Mn50.5-XNi41Sn 8.5+x Alloys*, J. Phys. D. Appl. Phys. **46**, (2013).

[11] A. K. Nayak, K. G. Suresh, and A. K. Nigam, *Giant Inverse Magnetocaloric Effect near*

Room Temperature in Co Substituted NiMnSb Heusler Alloys, J. Phys. D. Appl. Phys. **42**, 035009 (2009).

[12] S. Ghosh, P. Sen, and K. Mandal, *Effect of Si Doping on Magnetic and Magnetocaloric Properties of Ni–Co–Mn–Sn Alloys*, IEEE Trans. Magn. **54**, 1 (2018).

[13] C. L. Zhang, D. H. Wang, Z. D. Han, B. Qian, H. F. Shi, C. Zhu, J. Chen, and T. Z. Wang, *The Tunable Magnetostructural Transition in MnNiSi-FeNiGe System*, Appl. Phys. Lett. **103**, 132411 (2013).

[14] T. Samanta, P. Lloveras, A. Us Saleheen, D. L. Lepkowski, E. Kramer, I. Dubenko, P. W. Adams, D. P. Young, M. Barrio, J. L. Tamarit, N. Ali, and S. Stadler, *Barocaloric and Magnetocaloric Effects in (MnNiSi) 1− x (FeCoGe) X*, Appl. Phys. Lett. **112**, 021907 (2018).

[15] S. Ghosh, A. Ghosh, P. Sen, and K. Mandal, *Giant Room-Temperature Magnetocaloric Effect Across the Magnetostructural Transition in (MnNiSi)1-x(FeCoGa)x Alloys*, Phys. Rev. Appl. **14**, 014016 (2020).

[16] V. Johnson and C. G. Frederick, *Magnetic and Crystallographic Properties of Ternary Manganese Silicides with Ordered Co2P Structure*, Phys. Status Solidi **20**, 331 (1973).

[17] J. Chen, H. G. Zhang, E. K. Liu, M. Yue, Q. M. Lu, W. H. Wang, G. H. Wu, and J. X. Zhang, *Wide Temperature Window of Magnetostructural Transition Achieved in Mn 0.4 Fe 0.6 NiSi 1−x Ga x by a Two-Step Isostructural Alloying Process*, AIP Adv. **6**, 056220 (2016).

[18] S. Ghosh, P. Sen, and K. Mandal, *Magnetostructural Transition and Large Magnetocaloric Effect in (Mn0.6Fe0.4)NiSi1−Al (x = 0.06–0.08) Alloys*, J. Magn. Magn. Mater. **500**, 166345 (2020).

[19] C. L. Zhang, H. F. Shi, E. J. Ye, Y. G. Nie, Z. D. Han, B. Qian, and D. H. Wang, *Magnetostructural Transition and Magnetocaloric Effect in MnNiSi-Fe 2 Ge System*, Appl. Phys. Lett. **107**, 212403 (2015).

[20] M. Ilyn, A. M. Tishin, F. X. Hu, J. Gao, J. R. Sun, and B. G. Shen, *Magnetocaloric Properties of the LaFe11.7Si1.3 and LaFe11.2Co0.7Si1.1 Systems*, J. Magn. Magn. Mater. **290-291 PA**, 712 (2005).

[21] L. M. Moreno-Ramírez, C. Romero-Muñiz, J. Y. Law, V. Franco, A. Conde, I. A.

Radulov, F. Maccari, K. P. Skokov, and O. Gutfleisch, *Tunable First Order Transition in La(Fe,Cr,Si)13 Compounds: Retaining Magnetocaloric Response despite a Magnetic Moment Reduction*, Acta Mater. **175**, 406 (2019).

[22] F. Wang, Y.-F. Chen, G.-J. Wang, and B.-G. Shen, *LaFe 11 . 7 Si 1 . 3 Compound on the Magnetic Properties and Magnetic Entropy Changes*, Online **1**, 11 (2003).

[23] B. G. Shen, J. R. Sun, F. X. Hu, H. W. Zhang, and Z. H. Cheng, *Recent Progress in Exploring Magnetocaloric Materials*, Adv. Mater. **21**, 4545 (2009).

[24] F. X. Hu, J. Gao, X. L. Qian, M. Ilyn, A. M. Tishin, J. R. Sun, and B. G. Shen, *Magnetocaloric Effect in Itinerant Electron Metamagnetic Systems La (Fe 1-x Co x) 11.9 Si 1.1*, J. Appl. Phys. **97**, 1 (2005).

[25] O. Tegus, E. Brueck, K. H. J. Buschow, and F. R. de Boer, *ChemInform Abstract: Transition-Metal-Based Magnetic Refrigerants for Room-Temperature Applications.*, ChemInform **33**, no (2010).

[26] S. Ghosh, A. Ghosh, P. Sen, and K. Mandal, *Giant Room-Temperature Magnetocaloric Effect across the Magnetostructural Transition in (MnNiSi)1-x (FeCoGa)x Alloys*, Phys. Rev. Appl. **14**, 1 (2020).

[27] T. Krenke, E. Duman, M. Acet, E. F. Wassermann, X. Moya, L. Manosa, and A. Planes, *Inverse Magnetocaloric Effect in Ferromagnetic Ni-Mn-Sn Alloys*, Nat. Mater. **4**, 450 (2005).

[28] L. Huang, D. Y. Cong, H. L. Suo, and Y. D. Wang, *Giant Magnetic Refrigeration Capacity near Room Temperature in Ni 40Co10Mn40Sn10 Multifunctional Alloy*, Appl. Phys. Lett. **104**, 1 (2014).

Chapter 5 Tuning of magnetic and magneto-functional properties in Fe-Co doped Ni-Mn-Ti all-*d*-metal Heusler alloy

The limitation of the previous chapter has been solved by taking Ni-Mn-Ti all-d-metal Heusler alloys due to their excellent mechanical properties in this chapter. An extensive investigation of the magnetocaloric and magneto-transport properties of (Fe-Co) simultaneous doped in the above-mentioned all-d-metal Heusler alloys is presented.

Content of this chapter has been published in: **S. Samanta**, S. Ghosh, S. Chatterjee, and K. Mandal, " Large magnetocaloric effect and magnetoresistance in Fe-Co doped $Ni_{50-x}(FeCo)_xMn_{37}Ti_{13}$ all-*d*-metal Heusler alloys," **Journal of Alloys and Compounds 910 (2022) 164929**.

5 Tuning of magnetic and magneto-transport properties in Fe-Co doped all-*d*-metal Heusler alloy

5.1 Preface

Recently, Mn*M'X*-hexagonal compounds mentioned in previous two chapters (**chapter 3** and **4**) have widely studied due to their magneto-functional properties such as temperature induced magnetostructural transition (MST), giant magnetocaloric effect (GMCE), magnetic shape memory effect (MSME), barrocaloric effect (BCE), and large magnetostriction effect around low temperature [1–5]. The MST in these compounds is characterized by huge volume change as well as large magnetization change concurrently. However, after our investigation, we have faced some hurdles that may limit their utilization in long term basis. One is the brittleness properties. Owing to the structural transition from Ni_2In-type hexagonal to TiNiSi-type orthorhombic phase during cooling, a huge stress is induced which is enough to break the sample and hence, crack would form into the entire ingot. Another one, according to the Clausious-Clayperon relation, the giant entropy change greatly decreases the sensitivity of the MST to the external magnetic field. Therefore, a very high magnetic field is needed to get a complete and reversible MST.

Considering these disadvantages in Mn*M'X*-hexagonal compounds, we alternatively focus on Ni-Mn-based ferromagnetic shape memory alloys (FSMAs) which are thus promising systems for commercial applications due to their various multifunctional properties such as MSME [6], MCE [7–10], and magneto-resistance (MR) [11–13], observed across the magnetic-field induced inverse martensitic transformation (IMT) [8,9]. On cooling, these alloys undergo first-order MST from weak magnetic tetragonal/orthorhombic/ monoclinic martensite phase to ferromagnetic (FM) cubic austenite phase due to their strong coupling between crystal lattice and magnetic spin degrees of freedom. This feature makes them potentially useful in diverse technological applications in the field of actuators [14], sensors [15], and solid-state refrigerants [16]. They provide better performances to some extent like high sensitivity of MST and availability compared to Mn*M'X* compounds. However, they pose challenges towards the commercialization of solid-state refrigeration technology due to

their poor mechanical stability and large hysteresis losses across first-order MST. Besides, it is still a challenge to improve the manufacturing quality of this Heusler system.

Recently, Wei et al. have proposed an interesting multifunctional material that contains all-transition-metal based Ni-Mn-Ti Heusler alloys [17]. These newly developed promising alloys being eco-friendly, non-toxic, and inexpensive materials, have attracted great attention due to their excellent mechanical stability and multifunctionalities such as large MCE [18,19], colossal elastocaloric effect [20], giant barocaloric effect [21], giant exchange bias effect [5], and magneto-strain [22]. Wyckoff positions of Heusler alloys are A (0,0,0), B (¼,¼, ¼), C (½, ½, ½), D (¾, ¾, ¾) mentioned in the **Introduction** section. In Heusler alloys, a strong *p-d* hybridization bond between main group elements (D site) and transition elements (A/C site) influences the magnetic properties and drives MT [23] whereas, in the case of all-*d*-metal Heusler alloys, *d-d* hybridization between the transition elements with lower valance electrons (D site) and transition elements with higher valance electrons (A/C site) plays a similar role to the stabilization of parent austenite phase as well as provide an ordered structure [22].

However, in the stoichiometric form, Ni_2MnTi alloy usually displays an antiferromagnetic (AFM)-like ordering at low temperature ~120 K in the austenite phase, originating from Mn(B)-Mn(D) interaction. The off-stoichiometric Ni-Mn-Ti alloy exhibits martensitic transition in the paramagnetic (PM) state with no such significant change in magnetization. Hence, the chemical compositions adjusting or alloying new elements is a decisive tool to turn this AFM in to FM region and as a consequence, a coupled MST between FM cubic B2-type austenite (spatial group $Pm\bar{3}m$) and a weak-magnetic monoclinic (spatial group P2/m) or tetragonal (spatial group I4/mmm) will be developed [17]. However, doping one element is usually insufficient to get the afore-mentioned characteristics. For instance, substituting Co at Ni site and Ti at Mn site in Ni-Mn-Ti alloys usually increases the ferromagnetic coupling in parent phase and enhance Zeeman energy across MST, giving rise the large MCE [18]. On the other hand, it has also been reported that introducing Co in Ni site can downshift the MST temperature but leads to large thermal hysteresis (ΔT_{hys}) losses which can reduce the overall performance of the material as a refrigerant [17]. Similarly, Fe doping at the different atomic sites (Ni or Co) in the same system, not only decreases the ΔT_{hys} to an extent, yet additionally enhances the mechanical toughness through γ-phase formation in all-*d*-metal Heusler alloys [24,25]. Indeed, in Ni-Mn-Ti(Co) system, *d-d* hybridization is found to lead higher mechanical toughness across MST which is beneficial to its potential application [18]. Therefore, such experimental findings reveal that substituting two elements

for further study in all-*d*-metal Heusler alloys would be of significance in the practical and fundamental investigations.

In this chapter, we have tuned the MST by co-substitution of Fe and Co in Ni-site of all-*d*-metal Ni-Mn-Ti Heusler alloy and investigated the effect of $(FeCo)_x$ co-substitution on the structural, magnetic, magnetocaloric and magneto transport properties. The novel material $Ni_{50}Mn_{37}Ti_{13}$ is chosen as a parent sample which exhibits a martensitic transformation at a high temperature~440 K [26]. The present compositions have been tailored in such a way that the alloys undergo a MST around the room temperature with large ΔM and lower hysteresis losses across the MT. Our experimental investigations indicate that the MCE performances and MR over a wide temperature regime around the room temperature remain almost insensitive to $(FeCo)_x$ contents variation from 16 to 20 at.%. of all the present alloys. This result is expected to make these alloys to be potential materials for multifunctional applications.

5.2 Experimental

The $Ni_{50-x}(FeCo)_xMn_{37}Ti_{13}$ (x = 16, 18, and 20) alloys of approximately 2 g each are prepared by arc melting technique under a 4 N purity Argon atmosphere using high purity constituent elements. Each as-cast sample is wrapped with a tantalum foil in a high vacuum quartz tube and annealed at 1173 K for ensuring the homogenization. Past 4 days of heat treatment, samples are quenched into ice water. The final compositions are checked by energy-dispersive spectroscopy analysis. X-ray diffraction (XRD) patterns of the samples are investigated using SmartLab9kW, Rigaku with Cu-K_α radiation. Differential Scanning Calorimeter (DSC) heat flow measurements of the samples are carried out in a temperature range of 100 K ≤ T ≤ 500 K with a temperature ramp rate of 10 K/min. Magnetic measurements are performed using vibrating sample magnetometer (VSM) in a physical property measurement system (PPMS, Quantum Design). The transport measurements are performed in a physical property measurement system (PPMS, Quantum Design) using the ac-transport option. For both the resistivity and MR measurements, the electrical contacts are made in the four-probe configuration using conducting silver epoxy and copper wires.

5.3 Results

5.3.1 Structural characterization

XRD patterns and the corresponding Rietveld's refinements for all the samples at room temperature are depicted in **Fig. 5.1**. In this figure, B2, $L1_0$, and 5M denote cubic, tetragonal

and five-modulation monoclinic structure respectively. The sample x = 16 shows a modulated 5M-martensite with monoclinic structure (space group: P2/m) and non-modulated $L1_0$ martensite (structure tetragonal, spatial group I4/mmm) phase, which means the MST occurring above RT. The samples with x = 18 and 20 have a mixed phase of 5M-martensite and B2 cubic (space group P m $\bar{3}$ m) respectively, signifying that the MST is in the vicinity of RT.

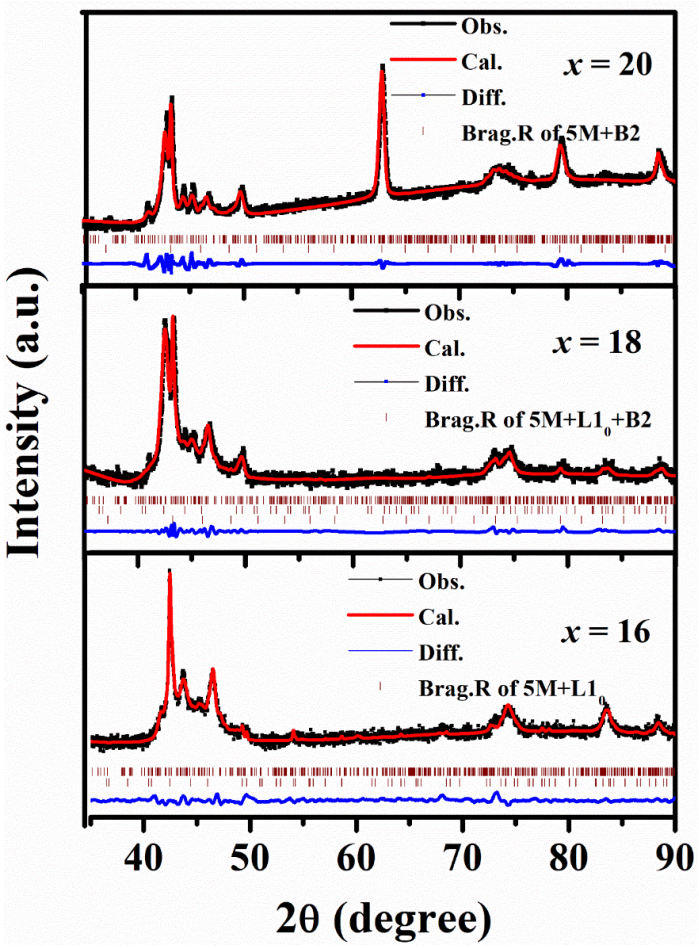

Figure 5.1: Rietveld refinements of XRD patterns of $Ni_{50-x}(Fe\ Co)_xMn_{37}Ti_{13}$ (x = 16, 18 and 20) alloys at 300 K. Here, the black line is the experimental data and red lines are Rietveld's refinement.

Therefore one can notice that with increasing $(FeCo)_x$ contents MST goes towards lower temperature through the stabilization of austenite phases [17,22]. The lattice parameters in their respective phases using the Rietveld refinement method for all the studied samples are tabulated in **Table 5.I**. In general, there is a relationship of crystal orientation between 5M martensite and B2 austenite phase and the unit cell volume changes (ΔV) of austenite and

martensite phase across the MST is obtained as; $\sqrt{2}a_M = a_c$; $b_M = a_c$; $\sqrt{2}c_M/5 = a_c$, and $2\,V_M = V_A$ [24]. With increasing $(FeCo)_x$, a large decrease in (ΔV) is observed from -1.82 % for x = 18 to -1.64 % for x = 20 upon MT. This is because Fe has smaller atomic radius compared to the Ni.

Table 5.I: Lattice parameters of B2, 5M and $L1_0$ structure for all composition transition alloys.

Sample	a_C (Å)	a_M (Å)	b_M (Å)	c_M (Å)	ß$_M$ (°)	a_{L10} (Å)	c_{L10} (Å)
x = 16	-	4.46	5.59	21.08	91.15	5.225	7.333
x = 18	5.913	4.45	5.59	21.11	91.22	5.235	7.331
x = 20	5.912	4.45	5.57	21.12	91.36	-	-

5.3.2 Magnetic properties analysis

The temperature dependence of magnetization (M-T) curves for all the samples in presence of an external magnetic field of 0.01 T under zero-field cooled (ZFC) and field cooled (FC) conditions is shown in **Fig. 5.2(a)**. All these samples show a PM to FM phase transition at their corresponding Curie temperature (T_C) along with a martensitic transition from a strong FM austenite phase to a weak magnetic martensite phase, during cooling. The presence of ΔT_{hys} in M-T curves ascertains a MST to be a first-order nature.

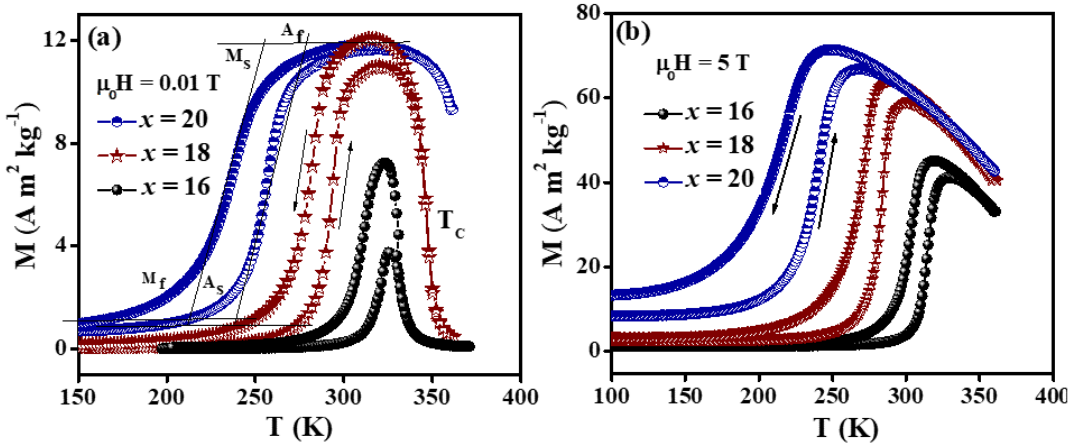

Figure 5.2: (a) M-T curves for $Ni_{50-x}(FeCo)_xMn_{37}Ti_{13}$ (x = 16, 18 and 20) alloys in presence of 0.01 T and (b) 5 T magnetic field.

The characteristic transformation temperatures of the MST namely, austenite start (A_s), austenite finish (A_f), martensite to austenite phase transition ($T_A = (A_s + A_f)/2$), martensite start (M_s), martensite finish (M_f), and austenite to martensite transition ($T_M = (M_s + M_f)/2$) as well as ($\Delta T_{hys} = T_A - T_M$) of all the alloys are tabulated in **Table 5.II**. A_s, A_f, M_s and M_f are given in the table, which is estimated from the intersection of the drawn baseline and the tangent line as shown in **Fig. 5.2(a)**. It is seen that with increasing *x* contents, T_M and T_A shifts towards lower temperatures whereas T_C is observed to shift towards higher temperatures. In general, the valance electron concentration (e/a) ratio is directly proportional to the T_M/T_A [27–29]. Here, the calculated e/a ratio is found to be decreased with $(FeCo)_x$ contents and T_M/T_A thus shifts to the lower temperature.

On the other hand, we give a detail explanation on the shifting of T_C towards higher temperature in our system. In off stoichiometric Ni-Mn-Ti system, the extra Mn atoms occupy Ti(D) sites and result AFM coupling with the nearest-neighbour Mn(B) atoms in both austenite and martensitic phase [17,18,30]. In the present work, the co-substitution of $(CoFe)_x$ acts as a "FM activator" and switches Mn(B)-Mn(D) AFM into Mn(B)-Fe/Co(A,C)-Mn(D) FM exchange coupling. It is also reported that compared to Fe, Co doping leads to a more pronounced enhancement of FM exchange interaction but rises the hysteresis loss, whereas Fe doping plays a contrastive role in affecting hysteresis loss [31,32]. Therefore, Fe-Co co-substitution would lead the higher FM exchange interaction and hence, results in increase of T_C in the all-*d*-metal Heusler alloy system. Indeed, the enhanced indirect *d-d* exchange interaction between Co/Fe(A,C)-Ti(D) in the austenite phase is also responsible for the increment of T_C [33].

Besides, M-T curves of all the samples in **Fig. 5.2(b)** within the temperature range of 80 K < T < 400 K are carried out under 5 T magnetic field. 5T magnetic field can shift the T_A about 11 K, ~12 K and ~20 K towards low temperature and calculated field sensitivity of T_A to the change of magnetic field ($\Delta T_A/\mu_0(\Delta H)$) ~ 2.2 K T^{-1}, 2.4 K T^{-1}, and 4 K T^{-1} is observed for x = 16, 18 and 20 alloys respectively. Actually, ($\Delta T_A/\mu_0(\Delta H)$) is quantified as sensitivity of the MST or IMT to the magnetic field. It is seen that the value of sensitivity in the present work is higher than previously reported Ni-Mn-Ti all-*d*-metal Heusler alloys [34–36].

Generally, the difference between T_C and T_A~$(T_C - T_A)$ is directly related to the sensitivity of T_A to the change of magnetic field i.e., larger $(T_C - T_A)$ give rise higher the $(\Delta T_A/\mu_0(\Delta H))$ [37]. According to the Clausius Clapeyron equation, $(\Delta T_A/\mu_0(\Delta H))$ $=\Delta M/\Delta S_{tr}$, the sensitivity depends on both on the magnetization change (ΔM) and transformation entropy change (ΔS_{tr}) but in opposite manner [9]. It has been shown in Ni-Mn-Z (Z= In, Sn, Sb) Heusler alloys as well that ΔS_{tr} across the transition decreases with the increase of $(T_C - T_A)$ [38–40]. These alloys with *x* = 16, 18 and 20 experience a significant jump in ΔM of about 40, ~56 and ~65 Am^2/kg respectively, during MST from FM austenite phase to weak magnetic martensite phase. The large ΔM gives rise to a large Zeeman energy difference and stabilize the FM austenite phase. This is also another consequence is that T_M shifts towards low temperature, and T_C shifts towards higher temperature. Therefore, we can expect that lower ΔS_{tr}, larger ΔM, and corresponding to the higher sensitivity with the (FeCo) doping in all-*d*-metal Heusler alloys would be favourable for refrigeration application [41,42].

Table 5.II: Characteristic transition temperatures of first-order MST, ΔT_{hys} and T_C and of $Ni_{50-x}(FeCo)_xMn_{37}Ti_{13}$ (*x* = 16, 18 and 20) alloys.

Sample	Characteristic transition temperatures							ΔT_{hys} (K)
	A_S (K)	A_f (K)	M_S (K)	M_f (K)	T_A (K) $= \left(\frac{A_S+A_f}{2}\right)$	T_M (K) $= \left(\frac{M_S+M_f}{2}\right)$	T_C (K)	
***x* = 16**	315	325	323	303	321	313	330	8
***x* = 18**	285	304	294	260	295	278	346	14
***x* = 20**	244	275	258	219	260	239	369	18

5.3.3 Study of DSC heat-flow measurement

Figure 5.3 illustrates the DSC heat-flow measurement for all the alloys where all samples exhibit endothermic and exothermic peaks, associated with IMT and MST, respectively. During cooling, MST takes place at around 311 K, 277 K, 238 K and the IMT occurs during heating at around 320 K, 294 K, 259 K for *x* = 16, 18, and 20, respectively. In addition, the presence of ΔT_{hys} between heating and cooling curve assures the phase transition to be first-order in nature. With the addition of $(FeCo)_x$ contents, the T_M decreases considerably, in agreement with the valance electron concentration (e/a ratio) where, lower valance electron of Fe and Co with respect to Ni [43,44]. Therefore, from the combination of magnetic, DSC and

XRD study described above sub-sections, we can conclude that the first-order MST is occurred around room temperature.

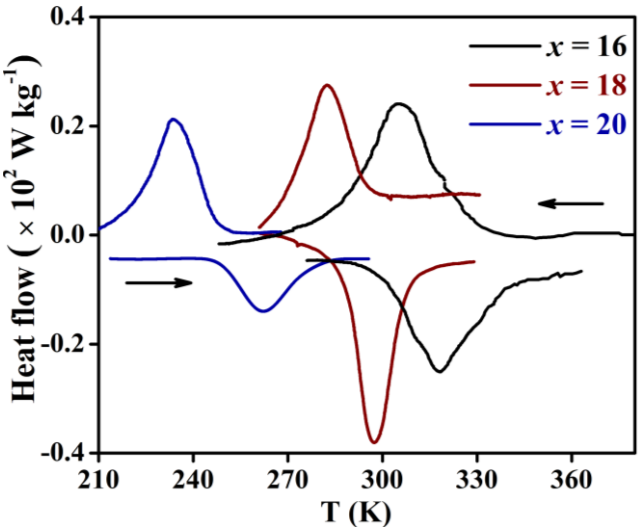

Figure 5.3: DSC heat flow curves taken upon heating and cooling at a ramp rate of 10 K/min for all the samples.

Further, S_{tr} of these alloys across first-order MST during cooling is measured following the equation,

$$\Delta S_{tr} = \int_{T_i}^{T_f} \frac{dQ}{dt}\left(\frac{dT}{dt}\right)^{-1}\frac{1}{T}dT \qquad (5.1)$$

where, dQ/dt is the heat flow changes of the sample. T_i and T_f, respectively are the starting and finishing temperatures of phase transition region. The obtained ΔS_{tr} is found to be about 14, 12.9 ~ and ~12.5 Jkg^{-1}K^{-1} for x = 16, 18, and 20 alloys, respectively. Therefore, our DSC measurement confirms that total entropy decreases at a smaller rate with larger doping changing, this may be an indication of robust transformation entropy in all-*d*-metal Heusler alloys.

5.3.4 Field dependent magnetic properties

Isothermal field-dependent magnetization (M-μ_0H) curves are measured during the heating cycle in the vicinity of IMT at 3 K interval due to a field change of 0-5 T for all the alloys which are shown in **Fig. 5.4**. The loop process protocol [45,46] is used to eliminate the field history effect of the sample for measuring M-μ_0H curves. In this protocol, the sample is

cooled down to a temperature (~150 K) in the pure martensitic phase and then heated to the desire temperature (for example 297 K for x = 16) to record isothermal M-μ_0H curve. After that the sample is heated to pure austenite phase (370K for x = 16), then cooled down to 150 K under ZFC and again heated to a temperature, 3 K upper than the previous one. It is noticeable that field-induced metamagnetic transition from FM austenite to weak/AFM magnetic martensitic phase is present for all the samples which again confirms the first-order nature of MST. The saturation magnetization increases with $(FeCo)_x$ content which signifies the enhancement of FM interaction in the system. Noted that in the x = 16 and 18 samples, the non-saturated magnetization in the M-μ_0H curves tell the presence of AFM phase in FM region [47].

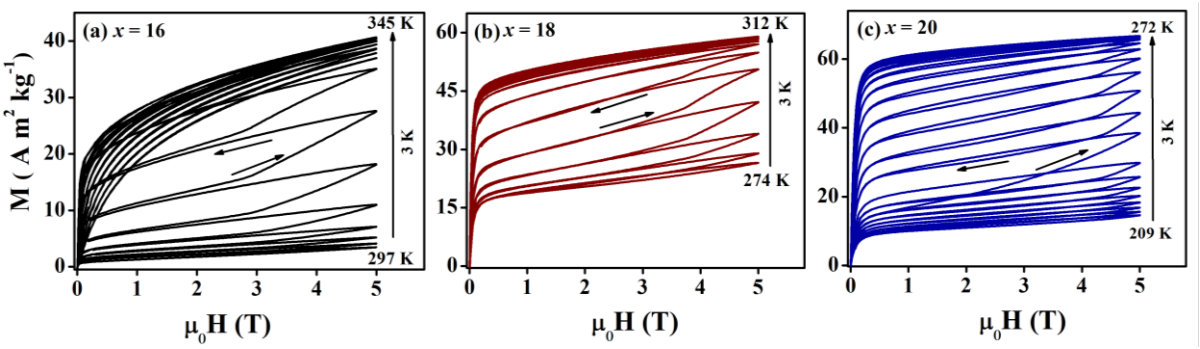

Figure 5.4: Isothermal M-μ_0H curves during heating for (a) x = 16, (b) x = 18 and (c) x = 20 samples.

Magnetocaloric properties of any magnetic material are solely depends on the nature of phase transition. A key prediction of the order of MST is the Banerjee criteria based on Arrott plot (M^2 vs. μ_0H/M). **Figure 5.5** presents here the Arrott plot of all the samples constructed using heating mode. Based on Banerjee criteria, the presence of negative slope on the Arrott plot across phase transition indicates the first-order phase transition and for the second-order phase transition, the slope takes positive values [48]. Clearly, the S-shaped curve noticed around the transition temperature ascribes the occurrence of magnetic field-induced transition [44]. Therefore, from the Arrott plot and Banerjee criteria, we can conclude that our system exhibits first-order phase transition.

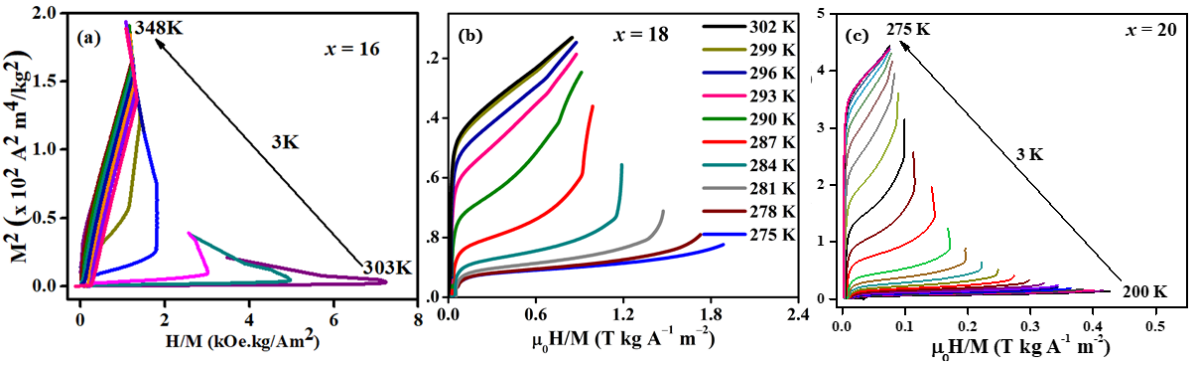

Figure 5.5: Arrott (M^2 vs. $\mu_0 H/M$) plots from isothermal M-μ_0H curve for (a) x = 16, (b) x = 18, and (c) x = 20 alloys.

5.3.5 Magnetocaloric properties

5.3.5.1 Magnetic entropy change

Isothermal magnetic entropy change (ΔS_M) is determined using Maxwell thermodynamic relation (equation **1.6**) [49] from isothermal M-μ_0H curves during field increasing mode and plotted as a function of temperature for the different field changes in **Fig. 5.6**. ΔS_M is found to be 13.8 Jkg^{-1}K^{-1} at 316 K, ~12.7 Jkg^{-1}K^{-1} at 289 K and ~11.8 Jkg^{-1}K^{-1} at 241 K due to field change of 5T for the alloy with x = 16, 18, and 20 respectively. The magnitude of ΔS_M enhances with the increasing magnetic field because large ΔM across MST is responsible in these alloys. It is striking to observe that the peak values of ΔS_M remain almost insensitive over a wide temperature regime around the room temperature when the composition changes from 16 % to 20 % in the system.

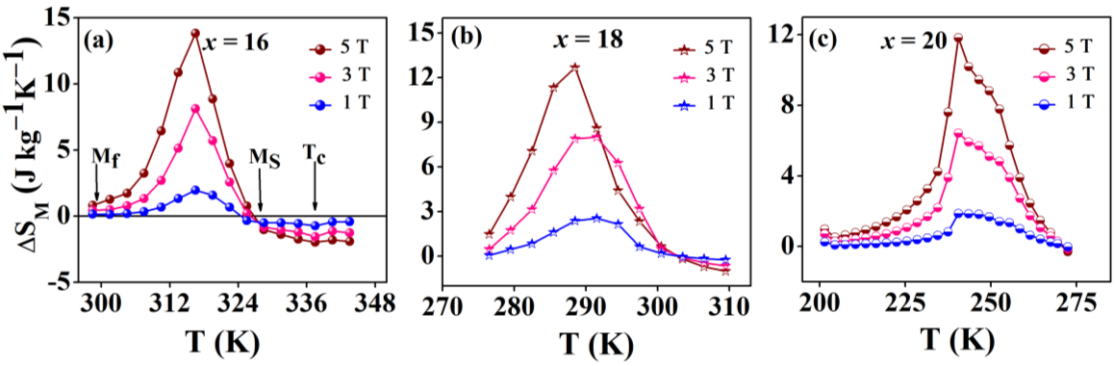

Figure 5.6: Temperature dependent magnetic entropy change under different magnetic field changes for (a) x = 16, (b) x = 18 and (c) x = 20 alloys.

5.3.5.2 Relative cooling power

Relative cooling power (RCP) is of crucial importance for the potential application to evaluate the performance of these studied alloys for the potential application as magnetic refrigerant materials. RCP can be calculated from the temperature-dependent ΔS_M curve using the following equation.

$$RCP = \Delta S_M^{peak} \times \Delta T_{FWHM} \quad (5.2)$$

where, ΔS_M^{peak} presents the peak value of ΔS_M from the ΔS_M-T curve (in **Fig. 5.6**) and ΔT_{FWHM} is the temperature region of the full width at half maxima (FWHM) of the same curve. The calculated RCP values are 137, 146, and 215 J/kg for x = 16, 18 and 20 samples respectively upon 5 T magnetic field change.

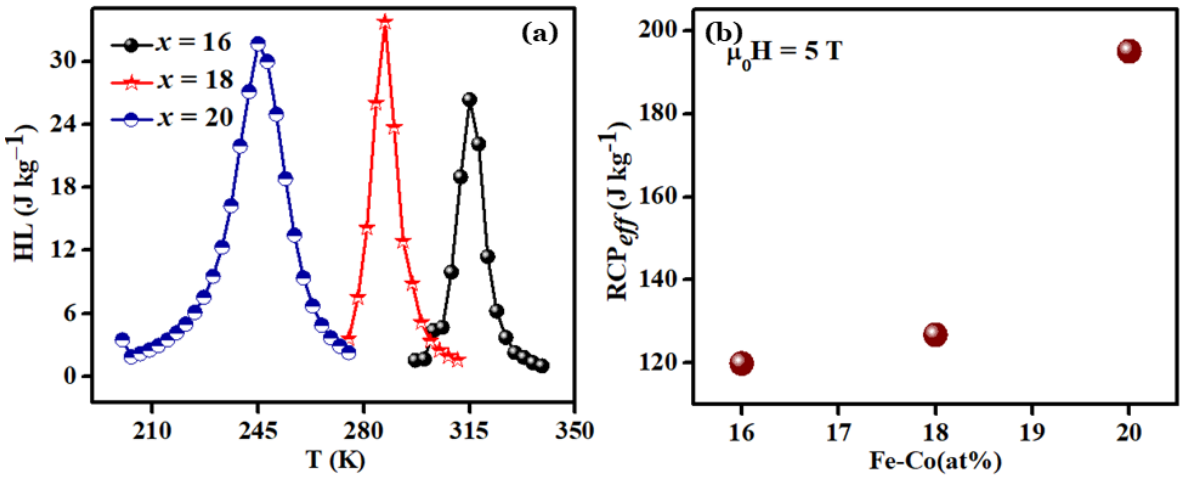

Figure 5.7: (a) Magnetic hysteresis loss vs temperature and (b) doping contents dependent effective refrigerant capacity of all the samples.

Remember, the caloric responses are solely calculated in our system across the first-order MST which includes hysteresis-related things. Therefore, to make useful of these materials in refrigeration technology, average magnetic hysteresis loss (HL) during field sweeping is need to subtract from the calculated RCP value so that we can get their effective refrigerant capacity (RC_{eff}) as magnetic refrigerant. HL in **Fig. 5.7(a)** is calculated from the isothermal M-μ_0H curves using the equation, $HL = \int_0^{H_{max}} \left| M_{H_{increase}} - M_{H_{decrease}} \right|_H dH$. The average HL is found to be 31.6, 33.7 and 26.3 J/kg for the alloys with x = 16, 18 and 20

respectively. Henceforth, the RC_{eff} in **Fig. 5.7(b)** is found to be 119.9, 126.18 and 194.4 J/kg for x = 16, 18 and 20 respectively.

5.3.6 Resistivity and Magnetoresistance

Figure 5.8(a)-(c) illustrates the temperature-dependent resistivity (ρ) for the alloys with x = 16, 18 and 20 which is recorded under thermal cycle at 0 and 5 T. From the plot at 0 T, one can see that in the martensite phase, ρ shows a increasing tendency with decreasing temperature, exhibiting a semiconductor-like behaviour [50]. Further rising temperature, especially across the MT, an abundant of martensitic fractions is transformed into austenite phase and as a consequent, a rapid decrease of resistivity is occurred [51–53]. On the contrary, ρ is observed to show a slightly increasing tendency with temperature in the austenite phase, exhibiting metallic-like behaviour. The phase transformation temperature, field-induced shift, and ΔT_{hys} as obtained from ρ-T curve agrees well with the result gotten from the DSC and M-T curves.

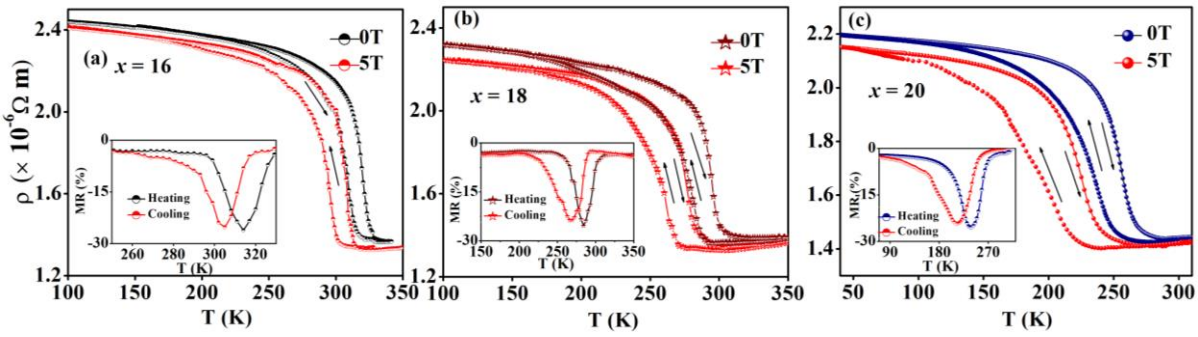

Figure 5.8: ρ-T curves for (a) x = 16, (b) x = 18 and (c) x = 20 alloys under 0 and 5 T. [The left inset of (a), (b), and (c) exhibits temperature-dependent MR for the present alloys].

In Heusler alloys, the weak magnetic martensitic phase is generally characterised by AFM or PM phase. The AFM spins have magnetic periodicity that can be different from the crystal periodicity of lattice. Therefore, it can govern new Brillouin zone boundary leading to a gap (known as superzone gap) on the fermi surface [54]. This superzone boundary gap results in the enhancement of resistivity due to the electron-spin scattering [52,55]. In addition, temperature-independent contribution known as residual resistivity, occurred from lattice defect and chemical impurities plays an important role on the increase of resistivity in the

martensitic phase. Therefore, the combined effects of both AFM spin-corelation and electron-phonon scattering resulting from the increased interfacial scattering from various twin boundary are responsible in the increase of resistivity with decreasing temperature in the martensitic phase. It can also be noticed that ρ of the martensite phase decreases with increasing $(FeCo)_x$ content which can be assigned due to the suppress of spin fluctuation in the martensite phase with magnetic doping content [32].

Once the 5 T of magnetic field is applied, the alloys exhibit similar behaviour of ρ but MT temperatures shifted towards lower temperatures, which signifies the field-induced metamagnetic MST [56]. However, the ρ of both phases is decreased under magnetic field, which can be attributed due to the Zeeman energy dominating over the s-*d* shattering [24]. The insets of **Fig. 5.8(a)-(c)** exhibit the temperature dependence of MR under a magnetic field change of 5 T and is calculated from equation **1.24** of **chapter 1**. A maximum MR values of -25.2% for $x = 16$, -24.2% for $x = 18$, and -23.7% for $x = 20$ on the cooling and ~ -26.1% for $x = 16$, -25.4% for $x = 18$, and -24.3% for $x = 20$ on the heating are observed across the MST across the IMT under 5 T, respectively. It is observed in our system that with increasing $(FeCo)_x$ contents, the AFM in the martensitic phase is reduced which lead to decreased MR [32]. Moreover, the difference in the magnitude of MR in the heating and cooling branch is due to the different fraction of coexistence austenite and martensitic phase during the MT and RMT in the sample [57]. It is worth noticing that the MR and ΔS_M show almost identical trend with increasing $(FeCo)_x$ contents throughout the measurements.

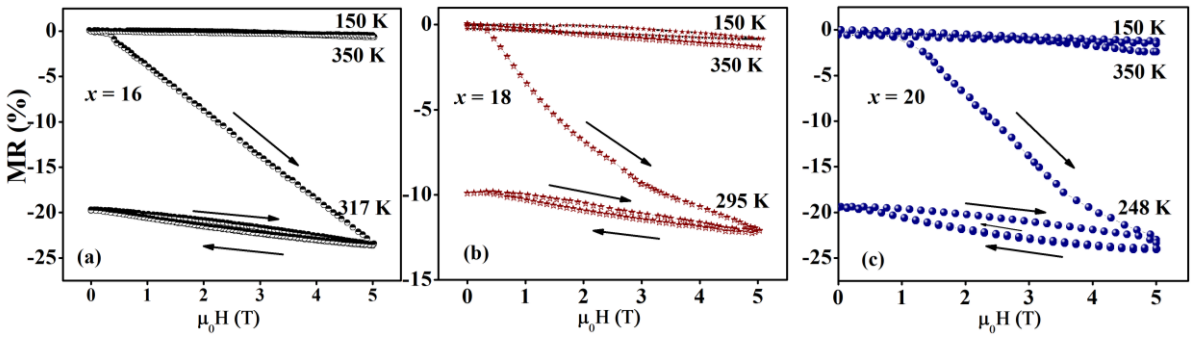

Figure 5.9. The field-dependent of MR across their respective martensite phase, magneto-structural transition temperature and austenite phase, respectively for (a) $x = 16$, (b) $x = 18$ and (c) $x = 20$ samples. The arrow shows the field ascending and descending path of the two field cycles.

The observation of large MR in the present system is further supported by isothermal field-dependent resistivity measurements at each pure phases and the transition temperature.

Before the measurement, the sample is first cooled down from austenite state to a fully martensitic phase (~100K) and then heated back to the respective temperatures and across the MT, two-loop field cycling processes are taken for the samples and the corresponding calculated MR has been highlighted in **Fig. 5.9(a)- (c)**. Clearly, in the fully martensitic region i.e., 150 K for x = 16, 150 K for x = 18, and 150K for x = 20, a small MR is observed. The MR at martensitic transition i.e., 317 K for x = 16 increases almost linearly with the field and reaches a maximum value of -25.4% at 5 T. On descending the field from 5 T to 0T, the MR could not reach back to its initial position, indicating that the sample is locked in a state with lower resistivity even after the field reduced to zero. This somehow implies that few percentage of austenite would become a kinetically arrested austenite phase through the RMT and it persists for subsequent field cycling [58,59]. On the other hand, for x = 18 and for x = 20 samples, at MT region, i.e., < 295 K and 248 K, the MR increases almost linearly for the field up to 3 T and 3.5 T respectively, beyond that it is raised slightly and reaches -12.9% and -24% at 5 T. Because the additional Zeeman energy overcomes the friction of twin boundary motion and hence, a portion of martensite transforms into austenite phase, resulting to a large MR [60]. In addition, the MR in the pure austenite region i.e., 350 K for x = 16, 18, and 20 alloys, is very small as the samples are already in the order austenite phase. Therefore, for the behaviour of field-induced locked state, the alloys can be potential candidate for magnetic memory applications.

5.4 Conclusion

The influences of varying Fe and Co with same ratio in Ni site on crystal structure, magnetocaloric and transport properties has been investigated in $Ni_{50-x}(FeCo)_xMn_{37}Ti_{13}$ all-*d*-metal Heusler alloys. First part of the study is centred on the establishment of a FM to AFM magnetostructural transition from an PM MST. It is found that with the doping from 16% to 20% of FeCo, T_M is observed to shift towards lower temperatures and T_C of austenite is found to shift to higher temperatures due to the increase of *d*-*d* hybridization between Fe/Co(A/C) site and Mn(D) site. Along with the shifting of T_M, an abrupt change in magnetization from weak magnetic martensite phase to strong FM austenite is occurred. This magnetization change across MST gives large ΔS_M of about ~13.8, ~12.7 and ~11.8 $Jkg^{-1}K^{-1}$ associated with large RC_{eff} of about 119.9, ~126.2 and ~194.4 J/kg is observed for the alloys x = 16, 18, and 20 respectively, upon application of 5 T magnetic field. In addition, maximum values of large MR~ -26.1% for x = 16, -25.4% for x = 18, and -24.3% for x = 20 are obtained in the field

of 5 T. Therefore, these materials with large MCE responses in a wide temperature window around room temperature as well as large negative MR would be considered as potential candidates for multifunctional application.

References:

[1] E. Liu, W. Wang, L. Feng, W. Zhu, G. Li, J. Chen, H. Zhang, G. Wu, C. Jiang, H. Xu, and F. de Boer, *Stable Magnetostructural Coupling with Tunable Magnetoresponsive Effects in Hexagonal Ferromagnets*, Nat. Commun. **3**, 873 (2012).

[2] Q. B. Hu, Y. Hu, S. Zhang, W. Tang, X. J. He, Z. Li, Q. Q. Cao, D. H. Wang, and Y. W. Du, *Large Reversible Magnetostrictive Effect of MnCoSi–Based Compounds Prepared by High-Magnetic-Field Solidification*, Appl. Phys. Lett. **112**, 052404 (2018).

[3] T. Samanta, P. Lloveras, A. Us Saleheen, D. L. Lepkowski, E. Kramer, I. Dubenko, P. W. Adams, D. P. Young, M. Barrio, J. L. Tamarit, N. Ali, and S. Stadler, *Barocaloric and Magnetocaloric Effects in (MnNiSi) 1− x (FeCoGe) X*, Appl. Phys. Lett. **112**, 021907 (2018).

[4] A. K. Nayak, K. G. Suresh, and A. K. Nigam, *Giant Inverse Magnetocaloric Effect near Room Temperature in Co Substituted NiMnSb Heusler Alloys*, J. Phys. D. Appl. Phys. **42**, 35009 (2009).

[5] S. Samanta, S. Ghosh, and K. Mandal, *Observation of Giant Exchange Bias Effect in Ni–Mn–Ti All-d-Metal Heusler Alloy*, J. Phys. Condens. Matter **34**, 105801 (2022).

[6] Z. H. Liu, M. Zhang, Y. T. Cui, Y. Q. Zhou, W. H. Wang, G. H. Wu, X. X. Zhang, and G. Xiao, *Martensitic Transformation and Shape Memory Effect in Ferromagnetic Heusler Alloy Ni2FeGa*, Appl. Phys. Lett. **82**, 424 (2003).

[7] T. Krenke, E. Duman, M. Acet, E. F. Wassermann, X. Moya, L. Manosa, and A. Planes, *Inverse Magnetocaloric Effect in Ferromagnetic Ni-Mn-Sn Alloys*, Nat. Mater. **4**, 450 (2005).

[8] J. Liu, T. Gottschall, K. P. Skokov, J. D. Moore, and O. Gutfleisch, *Giant Magnetocaloric Effect Driven by Structural Transitions*, Nat. Mater. **11**, 620 (2012).

[9] R. Kainuma, Y. Imano, W. Ito, Y. Sutou, H. Morito, S. Okamoto, O. Kitakami, K. Oikawa, A. Fujita, T. Kanomata, and K. Ishida, *Magnetic-Field-Induced Shape Recovery by Reverse Phase Transformation*, Nature **439**, 957 (2006).

[10] A. Ghosh and K. Mandal, *Effect of Fe Substitution on the Magnetic and Magnetocaloric Properties of Mn-Rich Mn-Ni-Fe-Sn off-Stoichiometric Heusler Alloys*, J. Appl. Phys.

117, 093909 (2015).

[11] R. Kainuma, Y. Imano, W. Ito, H. Morito, Y. Sutou, K. Oikawa, A. Fujita, K. Ishida, S. Okamoto, O. Kitakami, and T. Kanomata, *Metamagnetic Shape Memory Effect in a Heusler-Type Ni43Co7Mn39Sn11 Polycrystalline Alloy*, Appl. Phys. Lett. **88**, 192513 (2006).

[12] M. Khan, I. Dubenko, S. Stadler, and N. Ali, *Exchange Bias in Bulk Mn Rich Ni-Mn-Sn Heusler Alloys*, J. Appl. Phys. **102**, (2007).

[13] L. Chen, F. X. Hu, J. Wang, L. F. Bao, J. R. Sun, B. G. Shen, J. H. Yin, and L. Q. Pan, *Magnetoresistance and Magnetocaloric Properties Involving Strong Metamagnetic Behavior in Fe-Doped Ni 45(Co 1-XFe x) 5Mn 36.6In 13.4 Alloys*, Appl. Phys. Lett. **101**, (2012).

[14] M. Chmielus, X. X. Zhang, C. Witherspoon, D. C. Dunand, and P. Müllner, *Giant Magnetic-Field-Induced Strains in Polycrystalline Ni–Mn–Ga Foams*, Nat. Mater. **8**, 863 (2009).

[15] N. Sarawate and M. Dapino, *Experimental Characterization of the Sensor Effect in Ferromagnetic Shape Memory Ni–Mn–Ga*, Appl. Phys. Lett. **88**, 121923 (2006).

[16] L. Huang, D. Y. Cong, H. L. Suo, and Y. D. Wang, *Giant Magnetic Refrigeration Capacity near Room Temperature in Ni 40 Co 10 Mn 40 Sn 10 Multifunctional Alloy*, Appl. Phys. Lett. **104**, 132407 (2014).

[17] Z. Y. Wei, E. K. Liu, J. H. Chen, Y. Li, G. D. Liu, H. Z. Luo, X. K. Xi, H. W. Zhang, W. H. Wang, and G. H. Wu, *Realization of Multifunctional Shape-Memory Ferromagnets in All- d -Metal Heusler Phases*, Appl. Phys. Lett. **107**, 022406 (2015).

[18] A. Taubel, B. Beckmann, L. Pfeuffer, N. Fortunato, F. Scheibel, S. Ener, T. Gottschall, K. P. Skokov, H. Zhang, and O. Gutfleisch, *Tailoring Magnetocaloric Effect in All-d-Metal Ni-Co-Mn-Ti Heusler Alloys: A Combined Experimental and Theoretical Study*, Acta Mater. **201**, 425 (2020).

[19] H. Neves Bez, A. K. Pathak, A. Biswas, N. Zarkevich, V. Balema, Y. Mudryk, D. D. Johnson, and V. K. Pecharsky, *Giant Enhancement of the Magnetocaloric Response in Ni–Co–Mn–Ti by Rapid Solidification*, Acta Mater. **173**, 225 (2019).

[20] E. Bonnot, R. Romero, L. Mañosa, E. Vives, and A. Planes, *Elastocaloric Effect*

Associated with the Martensitic Transition in Shape-Memory Alloys, Phys. Rev. Lett. **100**, 125901 (2008).

[21] A. Aznar, A. Gràcia-Condal, A. Planes, P. Lloveras, M. Barrio, J.-L. Tamarit, W. Xiong, D. Cong, C. Popescu, and L. Mañosa, *Giant Barocaloric Effect in All-d-Metal Heusler Shape Memory Alloys*, Phys. Rev. Mater. **3**, 044406 (2019).

[22] Z. Y. Wei, E. K. Liu, Y. Li, X. L. Han, Z. W. Du, H. Z. Luo, G. D. Liu, X. K. Xi, H. W. Zhang, W. H. Wang, and G. H. Wu, *Magnetostructural Martensitic Transformations with Large Volume Changes and Magneto-Strains in All- d -Metal Heusler Alloys*, Appl. Phys. Lett. **109**, 071904 (2016).

[23] C. Xing, H. Zhang, K. Long, Y. Xiao, H. Zhang, Z. Qiu, D. He, X. Liu, Y. Zhang, and Y. Long, *The Effect of Different Atomic Substitution at Mn Site on Magnetocaloric Effect in Ni50Mn35Co2Sn13 Alloy*, Crystals **8**, 329 (2018).

[24] Q. Zeng, J. Shen, H. Zhang, J. Chen, B. Ding, X. Xi, E. Liu, W. Wang, and G. Wu, *Electronic Behaviors during Martensitic Transformations in All-d-Metal Heusler Alloys*, J. Phys. Condens. Matter **31**, ab2bd8 (2019).

[25] Y. Li, S. Huang, W. Wang, E. Liu, and L. Li, *Ferromagnetic Martensitic Transformation and Large Magnetocaloric Effect in Ni35Co15- XFe XMn35Ti15(x = 2, 4, 6, 8) Alloys*, J. Appl. Phys. **127**, 2 (2020).

[26] D. Cong, W. Xiong, A. Planes, Y. Ren, L. Mañosa, P. Cao, Z. Nie, X. Sun, Z. Yang, X. Hong, and Y. Wang, *Colossal Elastocaloric Effect in Ferroelastic Ni-Mn-Ti Alloys*, Phys. Rev. Lett. **122**, 255703 (2019).

[27] T. Krenke, M. Acet, E. F. Wassermann, X. Moya, L. Mañosa, and A. Planes, *Ferromagnetism in the Austenitic and Martensitic States of Ni-Mn-In Alloys*, Phys. Rev. B **73**, 174413 (2006).

[28] W. J. Feng, J. Du, B. Li, W. J. Hu, Z. D. Zhang, X. H. Li, and Y. F. Deng, *Large Low-Field Inverse Magnetocaloric Effect in Ni 50− x Mn 38+ x Sb 12 Alloys*, J. Phys. D. Appl. Phys. **42**, 125003 (2009).

[29] R. Sahoo, A. K. Nayak, K. G. Suresh, and A. K. Nigam, *Effect of Fe Substitution on the Magnetic, Transport, Thermal and Magnetocaloric Properties in Ni 50 Mn 38−x Fe x Sb 12 Heusler Alloys*, J. Appl. Phys. **109**, 123904 (2011).

[30] Z. Ni, X. Guo, X. Liu, Y. Jiao, F. Meng, and H. Luo, *Understanding the Magnetic Structural Transition in All-d-Metal Heusler Alloy Mn2Ni1.25Co0.25Ti0.5*, J. Alloys Compd. **775**, 427 (2019).

[31] L. Chen, F. X. Hu, J. Wang, L. F. Bao, J. R. Sun, B. G. Shen, J. H. Yin, and L. Q. Pan, *Magnetoresistance and Magnetocaloric Properties Involving Strong Metamagnetic Behavior in Fe-Doped Ni 45(Co 1-XFe x) 5Mn 36.6In 13.4 Alloys*, Appl. Phys. Lett. **101**, (2012).

[32] Y. Wu, H. Xuan, S. Agarwal, Y. Xu, T. Zhang, L. Feng, H. Li, P. Han, C. Zhang, D. Wang, F. Chen, and Y. Du, *Large Magnetocaloric Effect and Magnetoresistance in Fe and Co Co-Doped Ni-Mn-Al Heusler Alloys*, Phys. Status Solidi **215**, 1700843 (2018).

[33] E. C. Passamani, F. Xavier, E. Favre-Nicolin, C. Larica, A. Y. Takeuchi, I. L. Castro, and J. R. Proveti, *Magnetic Properties of NiMn-Based Heusler Alloys Influenced by Fe Atoms Replacing Mn*, J. Appl. Phys. **105**, 0 (2009).

[34] C. Ma, K. Liu, X. Han, S. Yang, N. Ye, and J. Tang, *Martensitic Transformation and Magnetocaloric Effect in Melt-Spun Mn50Ni31.5Co8.5Ti10 All-3d-Metal Alloy Ribbons*, J. Magn. Magn. Mater. **493**, 165733 (2020).

[35] K. Liu, X. Han, K. Yu, C. Ma, Z. Zhang, Y. Song, S. Ma, H. Zeng, C. Chen, X. Luo, S. U. Rehman, and Z. Zhong, *Magnetic-Field-Induced Metamagnetic Reverse Martensitic Transformation and Magnetocaloric Effect in All-d-Metal Ni 36.0 Co 14.0 Mn 35.7 Ti 14.3 Alloy Ribbons*, Intermetallics **110**, 106472 (2019).

[36] K. Liu, S. Ma, C. Ma, X. Han, K. Yu, S. Yang, Z. Zhang, Y. Song, X. Luo, C. Chen, S. U. Rehman, and Z. Zhong, *Martensitic Transformation and Giant Magneto-Functional Properties in All-d-Metal Ni-Co-Mn-Ti Alloy Ribbons*, J. Alloys Compd. **790**, 78 (2019).

[37] T. Gottschall, K. P. Skokov, D. Benke, M. E. Gruner, and O. Gutfleisch, *Contradictory Role of the Magnetic Contribution in Inverse Magnetocaloric Heusler Materials*, Phys. Rev. B **93**, 2 (2016).

[38] C. Salazar Mejía, M. Ghorbani Zavareh, A. K. Nayak, Y. Skourski, J. Wosnitza, C. Felser, and M. Nicklas, *Pulsed High-Magnetic-Field Experiments: New Insights into the Magnetocaloric Effect in Ni-Mn-In Heusler Alloys*, J. Appl. Phys. **117**, (2015).

[39] Z. D. Han, D. H. Wang, C. L. Zhang, H. C. Xuan, J. R. Zhang, B. X. Gu, and Y. W. Du,

The Phase Transitions, Magnetocaloric Effect, and Magnetoresistance in Co Doped Ni-Mn-Sb Ferromagnetic Shape Memory Alloys, J. Appl. Phys. **104**, (2008).

[40] X. He, Y. Zhang, S. Wei, Y. Cao, K. Xu, and Z. Li, *Achievement of a Reversible Giant Magnetocaloric Effect via Exerting External Hydrostatic Pressure on a Ni 45 Co 5 Mn 35 In 15 Metamagnetic Heusler Alloy*, J. Phys. D. Appl. Phys. **54**, 165001 (2021).

[41] B. Emre, N. M. Bruno, S. Yuce Emre, and I. Karaman, *Effect of Niobium Addition on the Martensitic Transformation and Magnetocaloric Effect in Low Hysteresis NiCoMnSn Magnetic Shape Memory Alloys*, Appl. Phys. Lett. **105**, 231910 (2014).

[42] A. K. Nayak, K. G. Suresh, and A. K. Nigam, *Giant Inverse Magnetocaloric Effect near Room Temperature in Co Substituted NiMnSb Heusler Alloys*, J. Phys. D. Appl. Phys. **42**, (2009).

[43] P. J. Shamberger and F. S. Ohuchi, *Hysteresis of the Martensitic Phase Transition in Magnetocaloric-Effect Ni-Mn-Sn Alloys*, Phys. Rev. B - Condens. Matter Mater. Phys. **79**, 1 (2009).

[44] X. Zhang, H. Zhang, M. Qian, and L. Geng, *Enhanced Magnetocaloric Effect in Ni-Mn-Sn-Co Alloys with Two Successive Magnetostructural Transformations*, Sci. Rep. **8**, 8235 (2018).

[45] L. Caron, Z. Q. Ou, T. T. Nguyen, D. T. Cam Thanh, O. Tegus, and E. Brück, *On the Determination of the Magnetic Entropy Change in Materials with First-Order Transitions*, J. Magn. Magn. Mater. **321**, 3559 (2009).

[46] S. Ghosh, S. Samanta, J. Sinha, and K. Mandal, *Measurement Protocols Dependent Giant Magnetocaloric Effect in MnNiSi-Based System*, Appl. Phys. Lett. **119**, 183901 (2021).

[47] R. Sahoo, A. K. Nayak, K. G. Suresh, and A. K. Nigam, *Effect of Si and Ga Substitutions on the Magnetocaloric Properties of NiCoMnSb Quaternary Heusler Alloys*, J. Appl. Phys. **109**, 07A921 (2011).

[48] N. G. Bebenin, R. I. Zainullina, V. V. Ustinov, and Y. M. Mukovskii, *Magnetic Properties of La0.7−xPrxCa0.3MnO3 Single Crystals: When Is Banerjee Criterion Applicable?*, J. Magn. Magn. Mater. **354**, 76 (2014).

[49] A. Gschneidner, V. K. Pecharsky, and A. O. Tsokol, *Recent Developments in*

Magnetocaloric Materials, Reports Prog. Phys. **68**, 1479 (2005).

[50] H. C. Xuan, Y. Deng, D. H. Wang, C. L. Zhang, Z. D. Han, and Y. W. Du, *Effect of Annealing on the Martensitic Transformation and Magnetoresistance in Ni–Mn–Sn Ribbons*, J. Phys. D. Appl. Phys. **41**, 215002 (2008).

[51] M. Khan, I. Dubenko, S. Stadler, J. Jung, S. S. Stoyko, A. Mar, A. Quetz, T. Samanta, N. Ali, and K. H. Chow, *Enhancement of Ferromagnetism by Cr Doping in Ni-Mn-Cr-Sb Heusler Alloys*, Appl. Phys. Lett. **102**, 112402 (2013).

[52] B. Zhang, X. X. Zhang, S. Y. Yu, J. L. Chen, Z. X. Cao, and G. H. Wu, *Giant Magnetothermal Conductivity in the Ni–Mn–In Ferromagnetic Shape Memory Alloys*, Appl. Phys. Lett. **91**, 012510 (2007).

[53] S. Y. Yu, Z. H. Liu, G. D. Liu, J. L. Chen, Z. X. Cao, G. H. Wu, B. Zhang, and X. X. Zhang, *Large Magnetoresistance in Single-Crystalline Ni50Mn50−xInx Alloys (X=14–16) upon Martensitic Transformation*, Appl. Phys. Lett. **89**, 162503 (2006).

[54] V. N. Antonov, A. Y. Perlov, P. M. Oppeneer, A. N. Yaresko, and S. V. Halilov, *Mechanism of the Giant Magnetoresistance in UNiGa from First-Principles Calculations*, Phys. Rev. Lett. **77**, 5253 (1996).

[55] M. D. Wilding and E. W. Lee, *Superzone Boundary Effects in the Electrical Resistivity of Dysprosium*, Proc. Phys. Soc. **85**, 955 (1965).

[56] R. Kainuma, W. Ito, R. Y. Umetsu, K. Oikawa, and K. Ishida, *Magnetic Field-Induced Reverse Transformation in B2-Type NiCoMnAl Shape Memory Alloys*, Appl. Phys. Lett. **93**, 091906 (2008).

[57] S. Chatterjee, S. Giri, S. Majumdar, and S. K. De, *Metastability and Magnetic Memory Effect in Ni2Mn1.4Sn0.6*, Phys. Rev. B **77**, 012404 (2008).

[58] S. Chatterjee, S. Giri, S. Majumdar, and S. K. De, *Giant Magnetoresistance and Large Inverse Magnetocaloric Effect in Ni 2 Mn 1.36 Sn 0.64 Alloy*, J. Phys. D. Appl. Phys. **42**, 065001 (2009).

[59] V. K. Sharma, M. K. Chattopadhyay, K. H. B. Shaeb, A. Chouhan, and S. B. Roy, *Large Magnetoresistance in Ni50Mn34In16 Alloy*, Appl. Phys. Lett. **89**, 222509 (2006).

[60] C. Jing, Y. Liu, D. Zheng, X. Wang, J. Sun, Y. Zhang, C. Liu, D. Deng, Z. Feng, K. Xu,

and Z. Li, *Large Spontaneous Exchange Bias and Giant Magnetoresistance in Ni50Mn37−xFexIn13(X=2–4) Heusler Alloys*, Solid State Commun. **241**, 32 (2016).

Chapter 6 Design of reversible magneto-functional properties around RT in Ni(Co)-Mn-Ti all-*d*-metal Heusler alloys

The problem of thermal and magnetic hysteresis in first order magnetostructural transition was pointed out before. In this Chapter 6, the topic has been discussed in detail and solved based on geometric compatibility condition between parent and product phases and minor hysteresis loop. Its effect on the reversibility of MCE and MR across the MST under field cycling has also been described.

Content of this chapter has been published in: **S. Samanta**, S. Chatterjee, S. Ghosh, and K. Mandal, "Large reversible magnetocaloric effect and magnetoresistance by improving improving crystallographic compatibility condition in Ni(Co)-Mn-Ti all-*d*-metal Heusler alloys" **Physical Review Material,** 6,094411(2022).

6 Design of reversible magnetofunctional properties around RT in Ni(Co)-Mn-Ti all-*d*-metal Heusler alloys

6.1 Preface

Energy functional material with first-order magnetostructural transitions (MST) are a prime element of solid-state-based cooling applications which has enormous potential to replace the conventional gas compression-based technology, because of high efficient and environment benign nature [1]. Among them, room-temperature (RT) magnetic refrigeration has attracted a much interest as a green, reliable, and significant energy conversion technology as after the discovery of RT giant magnetocaloric effect (MCE) across MST in $Gd_5(Si_2Ge_2)$ these system [2]. Recently, a number of materials such as $La(Fe, Si)_{13}$-based systems [3–5], MnNi(Ge, Si) systems [7], Ni-Mn-X (X=Ga, In, Sn) metamagnetic Heusler alloys [8–11] are evolved not only due to their giant MCE [12–14], but also multifunctional properties such as magnetic shape memory effect [15], elastocaloric effect [16], magneto-resistance (MR) [17–19], and so on, in the vicinity of their respective MST.

The first-order nature of MST, usually, involves the intrinsic hysteresis that causes the MCE irreversible during the subsequent field cycling operations. So far, two common technique of dealing with hysteresis; either finding way to obliterate it or reducing it as small as possible. Thus, much effort is devoted for the reduction of hysteresis based on the geometrical compatibility condition between the austenite and martensite phases [20–24]. In addition, another way to reduce the hysteresis in these Heusler family is modifying the chemical compositions, physical pressure, annealing conditions, minor loops, and measurement protocols [25–27]. For the commercial utilization, the material must be machinable in to desire shape without a reduction of MCE performances for operating thousands of cycles. However, in those systems, large hysteresis, and the brittleness nature upon magnetic field cycling acts as an obstacle in the field f technological applications.

Recently, a novel Ni-Mn-Ti all-*d*-metal Heusler alloy systems provide a strong evidence on the mechanical stability by considering *d*-*d* hybridization between transition metals instead of *p*-*d* hybridization between main group and transition metal of conventional Heusler alloys [28,29]. However, in stoichiometric form, $Ni_{50}Mn_{25}Ti_{25}$ alloy has an antiferromagnetic

(AFM) ground state with Neel temperature at 120 K in the austenite phase. This may originate from antiparallel coupling between Mn(B) and Mn(D) site. As already discussed in the previous section, by changing Mn/Ti ratio MST can be observed in the AFM region for this Ni-Mn-Ti system. Further studies turned this AFM interaction into a strong ferromagnetic (FM) Mn(B)-Co/Fe(A,C)-Mn(D) exchange coupling by partial Co/Fe substitution in Ni site. Hence a MST is established from a high temperature FM cubic B2-type austenite (spatial group $Pm\bar{3}m$) to a low temperature weak-magnetic or AFM monoclinic (spatial group P2/m) or tetragonal (spatial group I4/mmm) martensite phase [28].

Therefore, these systems have received enormous interest due to their magneto-functionalities governed at the magnetic field-induced inverse martensitic transformation (IMT). For instance, large magnetic entropy change (ΔS_M) of 38 $Jkg^{-1}K^{-1}$ driven by a relatively low magnetic field of 2 T across the MST of $Ni_{37}Co_{13}Mn_{34}Ti_{16}$ alloy is reported by Taubel *et.al* [30]. Recently, we report a giant conventional exchange bias field of 3.68 kOe in all *d*-metal $Ni_{40}(FeCo)_4Mn_{36}Ti_{20}$ Heusler alloy [31]. In addition, a colossal elastocaloric effect with a large reversible adiabatic temperature change (ΔT_{ad}) up to 31.5 K is achieved in $(Ni_{50}Mn_{31.5}Ti_{18.5})_{99.8}B_{0.2}$ bulk polycrystalline system [16]. Subsequently, Azner *et al*. obtained a giant barrocaloric effect with a large ΔS of 74 $Jkg^{-1}K^{-1}$ in the same system [32].

So far, several attempts have been reported how the MST can be tuned to RT, across which large functional properties is achieved. In the previous chapter, we were able to enhance ΔS_M by simultaneous Fe and Co doping in Ni site. But there is one issue with hysteresis which start to increase with Fe-Co doping. And another is the broadening of the MST that has a notable impact in affecting the entire magneto-functional properties. Considering all this facts and above experimental findings, we notice that tuning a small amount of Co doping in Ni site of Ni(Co)-Mn-Ti can rule out the abovementioned problems. Moreover, the effect of field cycling on the reversible MCE has not yet been addressed in this system, which is important for technological applications.

From the Clausius Clapeyron relation to get a complete and reversible field-induced IMT and its corresponding MCE, a minimum field is obtained

$$\Delta(\mu_0 H)_{min} = (\Delta T_{hys} + \Delta T_{int})/(\Delta M/\Delta S_{tr}) \quad \textbf{(6.1)}$$

(ΔM is the change in magnetization between austenite and martensite phase, ΔT_{hys}, ΔT_{int}, are the thermal hysteresis, transformation interval and ΔS_{tr} stands for the transformation entropy change respectively, across the transition). It is seen from above Eq. (6.1), the reversible field-

induced functional properties can be achieved in our systems for the smaller ΔT_{hys}, ΔS_{tr}, narrower ΔT_{int} as well as larger ΔM. Furthermore, $\Delta M/\Delta S_{tr}$ is closely related to the distance between T_C and inverse MT temperature ($T_C - T_A$) [33–35]. Hence, we can understand that it is easy to tune $\Delta M/\Delta S_{tr}$ by the varying $T_C - T_A$ in order to achieve the reversible multifunctional properties under subsequent field cycling in all-*d* -Ni-(Co)-Mn-Ti systems.

In this chapter, we investigated the reversible behavior of MCE and MR effects across the field-induced IMT in all-*d*-$Ni_{37-x}Co_{13+x}Mn_{34.5}Ti_{15.5}$ Heusler systems. Motivating by the work of Taubel *et al.* [30], our parent material is $Ni_{37}Co_{13}Mn_{34.5}Ti_{15.5}$ which exhibits smaller ΔT_{hys} (5.5 K), and ΔT_{int} (11.7 K. On the other hand, the presence of large ΔS_{tr}(~30 $Jkg^{-1}K^{-1}$) and weak sensitivity $(dT_M/d\mu_0 H)(\sim -1.6\ K/T)$ hinders them in technological application. Thus, we substituted a small amount of Co into the $Ni_{37}Co_{13}Mn_{34.5}Ti_{15.5}$, aiming to improve the reversible behaviours associated with the magnetostructural transformation. Furthermore, we established an geometrical compatibility condition, for the origin of low hysteresis, which is calculated using the lattice parameters between austenite and martensite phase [8,23,36].

6.2 Experimental

$Ni_{37-x}Co_{13+x}Mn_{34.5}Ti_{15.5}$ (x = 0, 1, and 2) polycrystalline samples are prepared by arc melting furnace under a 4 N purity Argon atmosphere using high purity constituent elements from Sigma Aldrich. Their purities are given as follows; Ni (foil, 4N), Co (granular, 3N), Mn (cheap, 2N), and Ti (foil, 5N). The furnace was purged 3 times and a Ti was melted before to the melting process in order to remove oxygen from the chamber. The samples were re-melted five to six times on each side to ensure homogenization. We faced a problem that extra Mn evaporate during melting, and then we again started re-melting using extra 6% Mn in the ingot to compensate Mn evaporation. The melted ingots were wrapped with a tantalum foil and sealed in a quartz tube under a high vacuum and annealed at 1323 K. Past 96 hours of heat treatment, the sample was quenched into ice water. The actual compositions of the presenting samples are verified by energy dispersive *x*-ray (EDX). The temperature-dependent of X-ray diffraction (XRD) patterns of the powder sample has been carried out using SmartLab9kW, Rigaku with Cu-K_α radiation. Magnetic measurements are performed in a vibrating sample magnetometer (VSM) using physical property measurement system (PPMS, Quantum design). Structural phase transition was checked by Differential scanning calorimetry (DSC, TA Instrument, Q2000) with a constant heating/cooling rate of 10 K/min. The specific heat capacity (C_P) is measured by a modulated-DSC technique using a standard sapphire sample with known C_P.

The magneto-transport measurements are performed in a physical property measurement system (PPMS, Quantum Design) using the ac-transport option.

6.3 Results and Discussions

6.3.1 Composition optimization from calorimetric Study

We substituted 1 to 2% of Co in Ni site to tune MST for optimization MCE parameters. **Fig. 6.1** illustrates DSC heat-flow curves and their characteristic transition temperatures, stated as austenite start (A_s), austenite finish (A_f), martensite start (M_s), martensite finish (M_f) determined by the tangent method from the DSC curves and corresponding austenite to martensite transition ($T_M = (M_s + M_f)/2$) and martensite to austenite phase transition ($T_A = (A_s + A_f)/2$), and ($\Delta T_{hys} = T_A - T_M$) of all the samples are tabulated in **Table 6.I**. The parent sample is plotted in black in the inset of **Fig. 6.1**. Data confirms that all samples exhibit endothermic peaks during heating and exothermic peaks during cooling, associated with IMT and MT, respectively. The ΔT_{hys} subsisted between heating and cooling curve confirms the first-order phase transition.

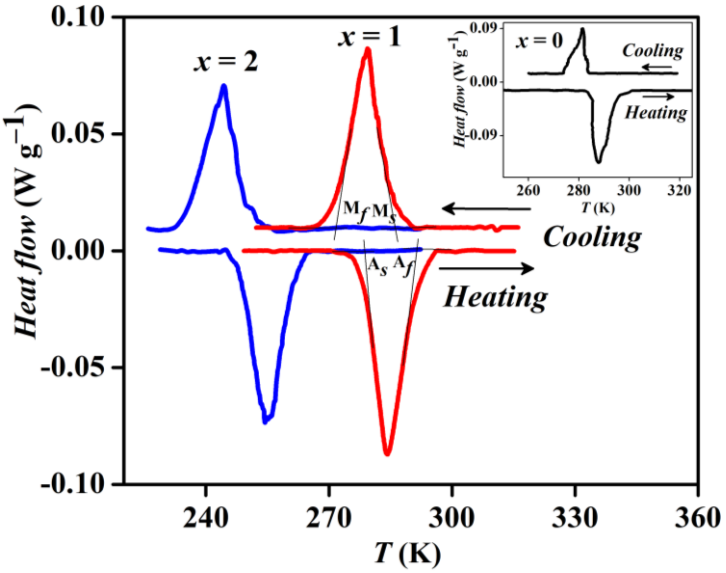

Figure 6.1: DSC heat-flow curve taken at 10K/min for all the investigated samples.

From the figure one can notice that, the transformation temperatures decrease considerably Co doping in Ni site which is in well agreement with the decrease in e/a ratio of Co with respect to that Ni [37]. Further, due to the interaction between structural and magnetic contribution to

the total transformation entropy change, ΔS_{tr} across first-order structural transition during heating is measured following the equation,

$$\Delta S_{tr} = \int_{T_i}^{T_f} \frac{dQ}{dt}\left(\frac{dT}{dt}\right)^{-1}\frac{1}{T}dT \qquad (6.2)$$

where, dQ/dt is the heat flow changes of the sample. T_i and T_f are the starting and finishing temperatures of first order phase transition respectively. The obtained ΔS_{tr} for all the samples is specified in **Table 6.I**. Clearly, x = 1 shows very small ΔT_{hys}, and moderate ΔS_{tr} compared to other samples.

Table 6.I: Transition temperatures (K) and transformation entropy change obtained from DSC curves of $Ni_{37-x}Co_{13+x}Mn_{34.5}Ti_{15.5}$ all-*d*-metal Heusler alloys.

Alloys	**M_S**	**M_f**	**A_S**	**A_f**	**T_M**	**T_A**	**ΔT_{int}**	**ΔT_{hys}**	**ΔS_{tr} (J/kg.K)**
***x* = 0**	283.2	274.3	286.1	292.3	278.6	289.2	8.9	10.6	22.5
***x* = 1**	286.1	274.9	278.5	290.1	280.5	285.2	11.2	4.7	19.89
***x* = 2**	250.3	235.3	244.6	261.1	242.8	252.9	15	10.1	18.89

6.3.2 Tuning MST from temperature dependence magnetization

Figure 6.2 shows the temperature-dependent magnetization measured under 0.05 and 5 T for all the samples. All sample exhibits a first-order MST from FM austenite to weak magnetic martensite below the Curie temperature (T_C), on cooling. The characteristic transition temperatures and T_C of all the samples are tabulated in **Table 6.II.** It is seen that upon the magnetic field change from 0.05 T to 5 T, the T_M is shifted by about 9 K, ~12 K, and ~16 K towards low temperature and corresponding to the shift of T_A about 8 K, ~10 K, and ~15 K for x = 0, 1 and 2 alloys. Hence, the sensitivity of transition temperatures to the magnetic field obtained from the linear fitting of T_M vs. field is shown in the inset of **Fig. 6.2(b)** and **6.2(c)** and their magnitudes are gathered in **Table 6.II**. This dependence produces a complete transition by applying of 5 T for x = 1 and 2 samples because the shift of T_A/T_M is larger than hysteresis. Although the value of $dT_M/d\mu_0 H$ is small compared to the Ni-Mn-In alloys [8,36,38] but higher than the Ni-Mn-Ti all-*d*-metal Heusler alloys [39], and MnNiGe-based system [40].

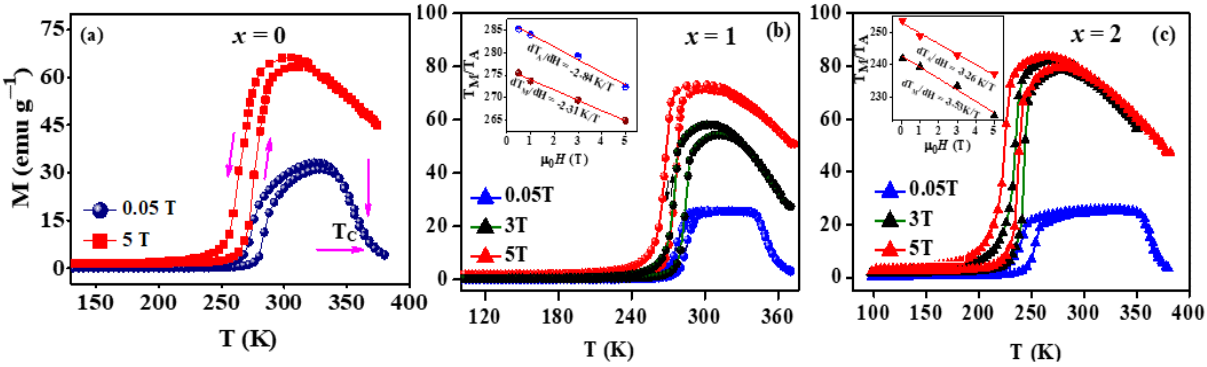

Figure 6.2: Temperature dependence magnetization in presence of 0.01T and 5 T magnetic field of (a) x = 0, (b) x = 1, and (c) x = 2 sample of Ni(Co)-Mn-Ti all-*d*-metal Heusler alloy.

As discussed in the introduction section that the sensitivity not only depends on ΔM but also ΔS_{tr} [14]. On the other hand, a clear correlation between ΔS_{tr} and $(T_C - T_A)$ is plotted in **Fig. 6.3**. It is shown that with the increasing $(T_C - T_A)$ the ΔS_{tr} across the IMT decreases because the distance of $(T_C - T_A)$ enhances the degree of chemical ordering which subsequently enhance the magnetic order of both phases which leads to a larger $dT_M/d\mu_0 H$ (and thus reversible MCE) [33–35]. Therefore, using this afore-mentioned strategy, comparing the M(T) and DSC curves, one can see that the sample with x = 1 possess relatively small ΔT_{hys}, ΔT_{int} and large ΔM, which is more favorable for the further reversible MCE studies.

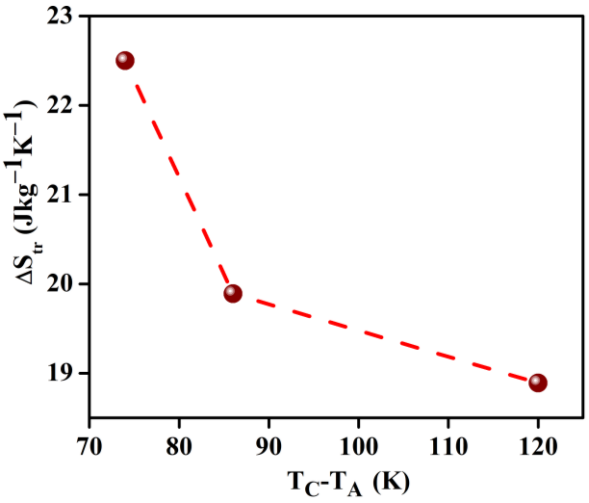

Figure 6.3: The change of total entropy at the martensitic transformation as a function of the distance between Curie temperature and martensitic transition temperature.

Table 6. II: Transition temperatures (K) and magnetic sensitivity obtained from MT curves of $Ni_{37-x}Co_{13+x}Mn_{34.5}Ti_{15.5}$ all-*d*-metal Heusler alloys.

Alloys	T_A (K)	T_M (K)	T_C (K)	ΔT_{hys} (K)	ΔT_{int} (K)	$dT_M/d\mu_0 H$(K/T)
***x* = 0**	284	275	349	9	14	1.9
***x* = 1**	284	276	352	6	11	2.8
***x* = 2**	254	242	362	12	12	3.2

6.3.2.1 Minor hysteresis loop during heating and cooling

Some points need to be considered for reversibility study is that the transformation characters in the minor loop is quite different from that a complete transition from martensite to austenite and vice versa. To study this behavior in our system we performed temperature-dependent minor loop measurement during heating and cooling sequences for $x = 1$ sample, as plotted in **Fig. 6.4**. These minor loops are strongly dependent on the size and shape of complete thermal hysteresis loop in different system. In this figure, pink dash line curves are the magnetization of complete phase transition and rests are the magnetization at different interval temperature.

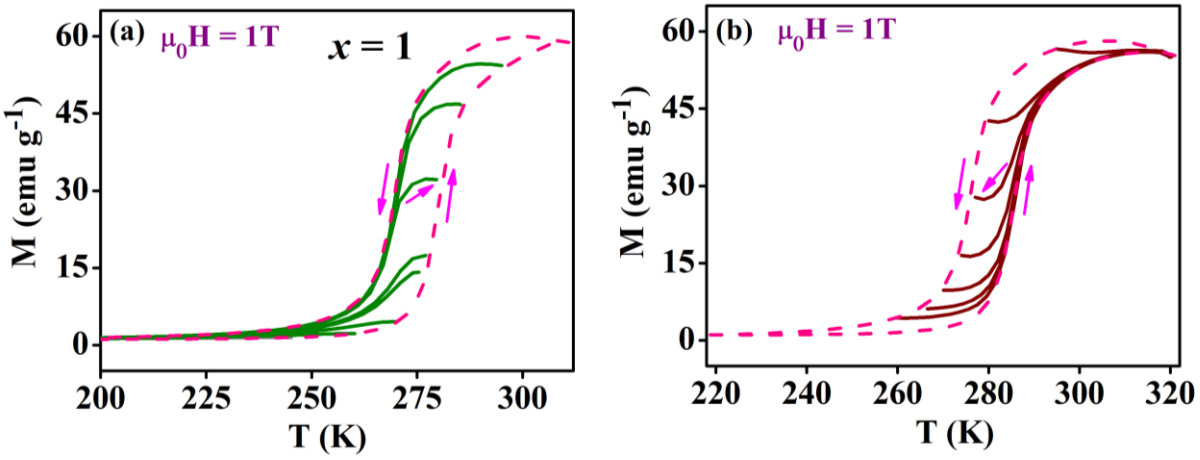

Figure 6.4: Minor hysteresis loop is measured during (a) heating and (b) cooling in presence of 1T applied magnetic field for $x = 1$ sample.

For measuring the minor hysteresis loop, sample is first cooled at a low temperature (~150 K) in the pure martensitic region and heating branch are recorded at a certain reversal temperature,

for example 280 K. At each reversal temperature, the heating is stopped and sample cooled down to 150 K to erase the memory of the sample. Same procedure is done for cooling sequences. Seven different magnetization curves of minor hysteresis loop are shown in the above **Fig. 6.4**.

It is well known that the first order martensitic transition in Heusler alloys is driven by nucleation and growth of forming a new phase and both processes contribute to the hysteresis loss. The ΔT_{hys} is associated the energy barrier between austenite and martensite phases. Minor hysteresis loop is one of the key factor that can dominate the energy barrier which is associated with the thermal hysteresis.

During heating and cooling in the minor loops, the sample undergoes a steep increase and decrease in magnetization respectively. From the graph, it is observed that in the vicinity of middle of the transition, for example, 280 K for heating and 277 K for cooling, the sample has a fraction of martensite ~ 52% and ~ 45% austenite phase respectively. The residual phase in the minor loop influences the ΔT_{hys} of forward and reverse MST as well [41–43]. Because, when we proceed a minor loop cycle instead of a major one, a certain amount of residual parent phase (austenite) is present in the product phase (martensite) before to the sample transforming back completely. This residual phase acts as nuclei and then the required nucleation energy is conserved. On the other hand, in major loop, there needs more energy for a nuclei formation. Therefore, the energy barrier of transformation can be reduced by following minor hysteresis loop. Hence, from our result it is observed that a large fraction ~ 52% of martensite upon heating mode is involved to contribute in reducing the hysteresis. Thus, we assume that due to the smaller hysteresis of minor loop, a large reversible magnetocaloric effect can be achieved in $Ni_{34}Co_{14}Mn_{34.5}Ti_{15.5}$ all-*d*-metal Heusler alloy.

6.3.3 Geometric compatibility condition from structural analysis

In magnetic shape memory alloys (SMAs), the thermal hysteresis and consequently, an irreversible properties at the IMT is strongly related to the austenite and martensite phase and their interfaces [22,23,44–46]. This interface is known as habit plane which is undistorted and un-rotated. During phase transformation, an elastic transition layer is governed at the meeting region instead of exact interface. For the MST and IMT, energy is associated with the formation of interface produce in hysteresis. Recently, geometrical compatibility condition between both phases provides an evidence for the formation of smaller hysteresis and also sharpness of

transformation interval and hence, is established a certain condition for it [20,22]. The afore-mentioned mathematical condition is characterised by the deformation of martensite which is calculated using lattice parameters of both phases. Mathematically, the determinant of the transformation stretch matrix **U** defining as a homogeneous 3×3 deformation matrix should be one. That signifies the no volume change between two phases. Second criteria are the middle eigen value λ_2 of $\mathbf{U} = 1$, where $\lambda_1 \geq \lambda_2 \geq \lambda_3$ are the order eigenvalues of **U**, yields the existence of an invariant plane between both phases.

To determine **U** for our system, structural information is needed. The temperature-dependent powder XRD experiment has been carried out for *x* = 1 sample as depicted in **Fig. 6.5(b).** During heating, the sample give rise IMT the transition from martensitic phase with a 5-modulated (5M) monoclinic structure to a cubic austenite phase. Indeed, a small fraction of martensite at 300 K is found due to the residual stress generated during the grinding the ingot into powder [47]. From **Fig**. **6.5(a)** the refined lattice parameters, at 277 K where both phases coexist, are $a_M = 4.342$ Å, $b_M = 5.5136$ Å, $c_M = 21.0359$ Å , and $\beta_M = 90.95°$ and $a_c = 5.9213$ Å for martensite and austenite phases, respectively. Theoretically, for occurring cubic to monoclinic transformation, there are 12 correspondence variants for modulated monoclinic structure of martensite phase as already mentioned in the Chapter 1. These variants have the same eigenvalue, eigenenergy and volume changes [36]. The U of one of the corresponding variants of martensite phase is given by

$$U = \begin{pmatrix} \tau & \sigma & 0 \\ \sigma & \rho & 0 \\ 0 & 0 & \delta \end{pmatrix} \tag{6.3}$$

where the deformations are given by

$$\tau = \frac{\alpha^2 + \gamma^2 + 2\alpha\gamma(sin\beta - cos\beta)}{2\sqrt{\alpha^2 + \gamma^2 + 2\alpha\gamma sin\beta}}, \tag{6.3a}$$

$$\rho = \frac{\alpha^2 + \gamma^2 + 2\alpha\gamma(sin\beta + cos\beta)}{2\sqrt{\alpha^2 + \gamma^2 + 2\alpha\gamma sin\beta}}, \tag{6.3b}$$

$$\sigma = \frac{\alpha^2 - \gamma^2}{2\sqrt{\alpha^2 + \gamma^2 + 2\alpha\gamma sin\beta}}, \tag{6.3c}$$

and $$\delta = \frac{b_M}{a_c} \tag{6.3d}$$

with $\alpha = \frac{\sqrt{2}a_M}{a_c}$, and $\gamma = \frac{\sqrt{2}c_M}{Na_c}$ [45,48], a_c is the lattice parameter of cubic austenite phase and a_M, b_M, c_M, and the angle β denote the lattice parameters of monoclinic unit cell. Now the transformation matrix of the x = 1 sample is

$$U = \begin{pmatrix} 1.0293 & 0.0161 & 0 \\ 0.0161 & 1.0124 & 0 \\ 0 & 0 & 0.9311 \end{pmatrix}$$

The eigenvalues of the above matrix are 1.0353, 1.0065, and 0.9378. It is observed that the λ_2 is very closed to 1 and hence, $|1 - \lambda_2| = 0.0065$ with the deviation of 0.65% from the unity, assuring the geometric compatibility between the two phases has been significantly improved [21,45,48,49]. Consequently, a small hysteresis is found in all-*d*- Ni-Co-Mn-Ti Heusler alloys.

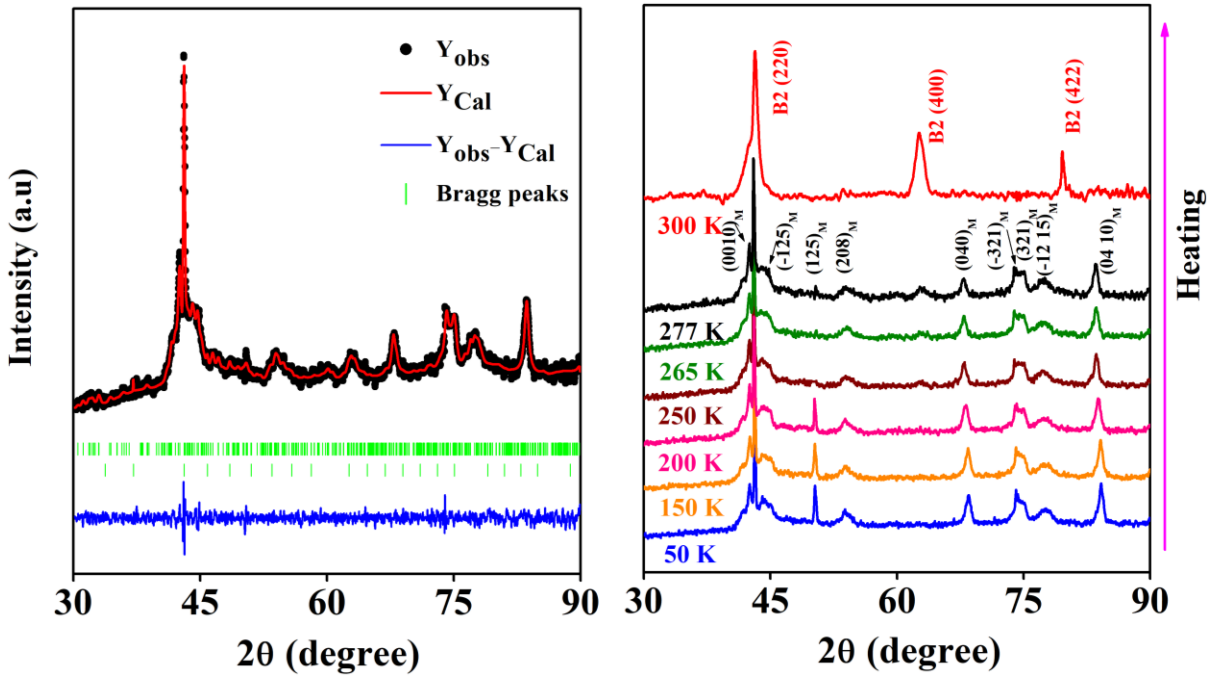

Figure 6.5: (a) Rietveld profile refinement of XRD pattern of $Ni_{37}Co_{14}Mn_{34.5}Ti_{15.5}$ alloy at the inverse martensitic transformation temperature. (b) Temperature-dependent XRD graph for the same sample is recorded in the heating mode. [Cubic and monoclinic phase are denoted as 'B2' and 'M' respectively].

6.3.4 Reversible Magnetocaloric performances

As discussed above, as x = 1 sample shows small ΔT_{hys}+ΔT_{int} and large ΔM and hence, we expected to achieve a magnetic-field-induced complete and reversible during magnetic field cycling. For this, we have taken isothermal magnetization M-μ_0H curves during cyclically magnetic field sweeping in the vicinity of transition region between 265 K and 283 K with an interval of 3 K, illustrated in **Fig. 6.6(a)**. The measurement procedure of the first field cycle is done as follows: 300K→150K→T(K) (M- μ_0H) →150K (T+2)(K) (M- μ_0H)….. [50,51]. In the second field cycle, the M-μ_0H curve at the same temperature has been measured just after the first cycle of field sweeping. The hysteresis between field increasing and decreasing branch of M-μ_0H curve is observed, exhibiting a strong metamagnetic behavior between 268 K and 283 K, confirming magnetic field-induced IMT from weak magnetic martensite to FM austenite phase. At the austenite start temperature (~268 K), M-μ_0H curves of both cycles overlap with each other, suggesting a fully reversible field-induced IMT take place. Once, we found that towards the transition from 271 K to 283 K, the low field magnetization in M-μ_0H curves of the second cycle is higher than the first one and M-μ_0H curves. The similar behavior like second cycle is observed during the third and following field cycles that coincide with the second field cycle. This observation signifies a good reversibility of magnetostructural transition after the first field cycle. No martensite phase in the M-μ_0H curve is recovered after the first cycle at 283 K, which implies that field-induced inverse martensitic transformation does not occur after 283 K under the field cycling [52,53].

Now we quantitatively elaborate the above results based on the reversible effect in the Ni-(Co)-Mn-Ti system. Once the magnetic field of 5 T is applied above A_S, for instance, from 268 K to 280 K, since FM state is energetically favourable with the magnetic field, the field-induced IMT with large magnetic hysteresis arises with the first field increasing of 5 T. Upon decreasing the magnetic field from 5 T, as a result of magnetic ΔT_{hys}, the induced austenite cannot fully go back to martensite and consequently, residual austenite is conserved. So, this residual austenite takes part in the increase in magnetization of the second cycle because of its FM nature. On the other hand, during the second cycle with small magnetic ΔT_{hys}, a portion of the sample can transform back and forth between martensite and austenite during second and all sequent field cycling. Therefore, this portion could govern a reversible and reproducible magnetocaloric effect.

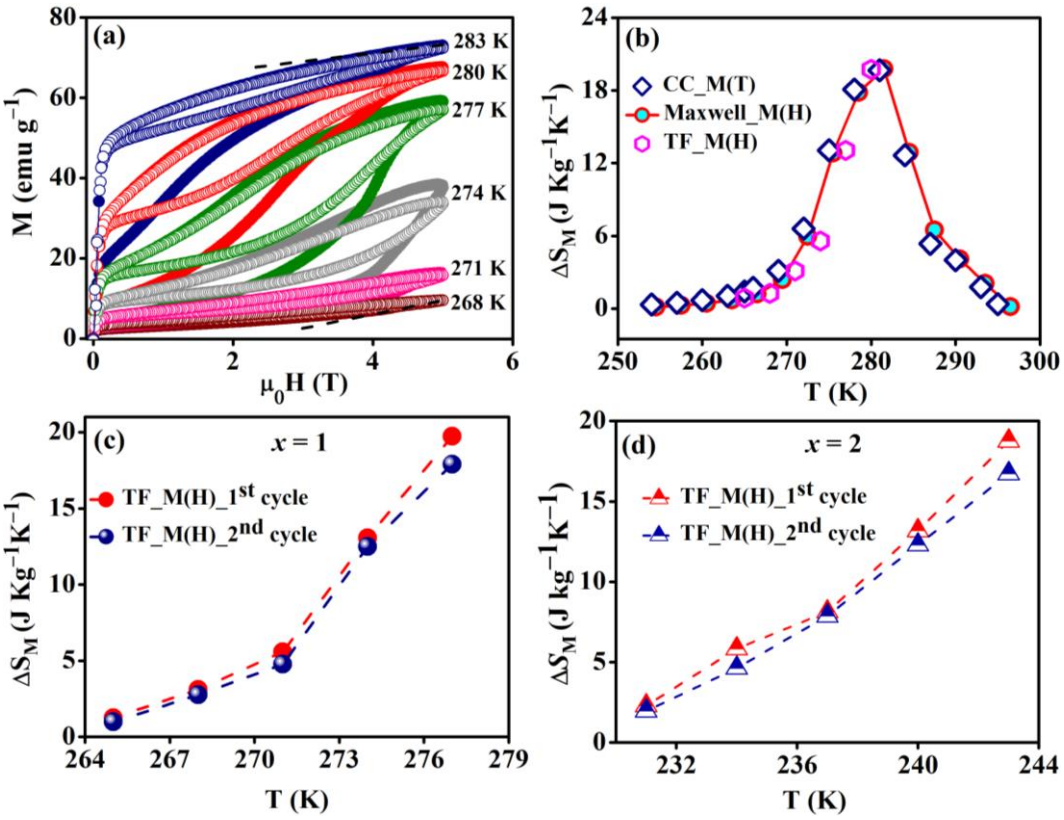

Figure 6.6: (a) Temperature dependent M-μ_0H hysteresis measured during the 1st (solid circle) and 2nd (hollow circle) cycle of field sweeping at 268 K, 271 K, 274 K, 277 K, and 280 K during heating. (b) Comparison of ΔS_M vs. T during first field cycle at 5 T determined from the various methods using Maxwell relation (Maxwell M(μ_0H)), Clausius Clapeyron relation (CC_M(T), and transformation fraction method (TF_M(H)). (c) The ΔS_M vs. T by TF_M(H)) during first and second field cycles of x = 1 sample, and (d) of x = 2 sample.

6.3.4.1 Reversible magnetic entropy change

Isothermal magnetic entropy change of the sample x = 1 and 2 is computed across T_A using Maxwell thermodynamic relation (**equation 1.14**). A maximum magnitude of ΔS_M ~ 19.78 Jkg^{-1}K^{-1} at 281.5 K is obtained for x = 1 due to a magnetic field change of 5 T. In **Fig. 6.6(b)** the magnitude of ΔS_M is in well agreement with ΔS_{tr} as determined from the DSC curve in **Table 6.I**.

To understand the reversible properties of ΔS_M in better way, the ΔS_M has been deduced using different methods. Clausius-Clapeyron equation using transformation fraction method is suitable for the first-order IMT and has been used to obtain ΔS_M values from iso-field M(T) measurements for the different field changes [54].

$$\Delta S_M = -\Delta f \, \Delta M \left(\frac{\Delta T_A}{\Delta \mu_0 H}\right)^{-1} \quad (\mathbf{6.4})$$

where, Δf is the change in phase fraction of austenite induced by the magnetic field change that can be defined as $\Delta f\,(T, \mu_0 \Delta H) = f\,(T, \mu_0 H_f) - f\,(T, \mu_0 H_i)$. $\mu_0 H_i$, and $\mu_0 H_f$ are the initial and final applied magnetic field, respectively. As the austenite phase fraction is proportional to the total magnetization and hence, austenite phase fraction can be calculated as [54] $f(T) = \frac{M(T)-M_M(T)}{M_A(T)-M_M(T)}$, where, M_M(T) and M_A(T) are the magnetization of the low-temperature phase and high-temperature phase respectively. The maximum ΔS_M for the field changes from H_i ~50 mT to H_f ~5 T is 19.66 Jkg^{-1}K^{-1}, as shown in **Fig. 6.6(b)**. The temperature dependent magnetic entropy change obtained from both Maxwell relation and CC equation confirms that our ΔS_M are reliable [55].

Furthermore, to achieve reversible and reproducible MCE, the transformation fraction method based on M-μ_0H curve is a feasible and reliable procedure for the first order phase transition system [10]. The phase fraction of austenite is determined from the M-μ_0H curve of both cycles at the respective temperatures using the following equation

$$f(H) = \frac{M(H)-M_M(H)}{M_A(H)-M_M(H)} \quad (\mathbf{6.5})$$

where, M_M (H) and M_A(H) stand for the magnetization of the martensite and austenite phase which can be noted by the extrapolating of M-μ_0H curve at 250 K and 300 K of pure martensite and austenite phase, respectively [56]. **Figure 6.6(b)** illustrates the ΔS_M value vs. temperature due to field change of 5 T based on the various methods during the first field cycle for x = 1 sample. It is clearly shown that the magnitude of ΔS_M estimated from TF_M(μ_0H) is almost consistent with the CC_M(T) and Maxwell equation. As stated in the Introduction part of this chapter, the field-induced transformation is reversible during second and subsequent field cycles in the temperature range between 265 K and 280 K, we estimated ΔS_M using TF_M(μ_0H) method for both cycles and plotted in **Fig. 6.6(c)**. One can notice that the maximum magnitude of ΔS_M during second cycle is quite close to that of the first one which ascribes to the good reversible MCE at the IMT. Since a large fraction of magnetic field-induced MST is contributed to the MCE, a large reversible ΔS_M of 17.78 Jkg^{-1}K^{-1} over a broad temperature window ~ 12 K is achieved upon 5 T for x = 1 sample.

For comparison x = 2 sample with x = 1, similar measurements are performed and the ΔS_M value at 243K obtained from TF_M(μ_0H) method for first and second cycles are 18.76 Jkg^{-1}K^{-}

^{1} and 16.72 $Jkg^{-1}K^{-1}$ respectively, depicted in **Fig. 6.6(d)**. The graph clearly shows the ΔS_M value of second field cycle is about 11% smaller than the first cycle. The reduction of ΔS_M in the second field cycle is caused due to the large residual field induced austenite formed during first field decreasing cycle does not take part in the transformation during the following field cycle. Therefore, $x = 1$ sample give rise large reversible entropy change which represent nearly 90% of total magnetic entropy change obtained at the first field cycle. We have compared the magnitude of reversible ΔS_M with the highest value reported in the other related promising systems (shown in **Table 6.III**). Thus, the present system consists of low cost materials with large reversible MCE which will be highly attractive for room temperature magnetic refrigeration.

Table 6.III: Comparison of reversible S_M at 5 T and the peak value of their respective transition temperatures (T_A) of all-*d* $Ni_{37-x}Co_{13+x}Mn_{34.5}Ti_{15.5}$ Heusler alloys, and other related promising systems.

Materials	$\lvert\Delta S_M^{peak}\rvert$ **(J kg^{-1}K^{-1})**	**T_A (K)**	**References**
Gd	10.2	294	[57]
$Gd_5(Si_2Ge_2)$	18.5	278	[2]
$Ni_{49.8}Co_{1.2}Mn_{33.5}In_{15.5}$	14.6	235	[58]
$Ni_{49}Co_3Mn_{34}In_{14}$	16.5	268	[38]
$Ni_{50.7}V_{0.3}Mn_{33.4}In_{15.6}$	18.9	276	[59]
$Ni_{41.5}Co_{9.2}Mn_{32}Ga_{14}In_{3.3}$	11	-	[60]
$Ni_{41}Ti_1Co_9Mn_{39}Sn_{10}$	18.7	287	[10]
$Ni_{1.9}Pt_{0.1}Mn_{1.4}In_{0.6}$	12	262	[61]
$Mn_{1.87}Cr_{0.13}Sb_{0.95}Ga_{0.05}$	5.2	280	[62]
$Ni_{37-x}Co_{13+x}Mn_{34.5}Ti_{15.5}$ $x = 1$	17.8	277	**Present work**

6.3.4.2 *Adiabatic temperature change*

ΔT_{ad} is another important characteristic parameter to quantify the MCE. It is reported that the reversible ΔT_{ad} is roughly estimated using the measuring temperature-dependent specific heat capacity following the equation,

$$\Delta T_{ad} = -\frac{T}{C_p} \times \Delta S_M \quad \textbf{(6.6)}$$

C_p has been recorded in zero field condition using modulated DSC technique as shown as a function of temperature in **Fig. 6.7(a)**. The reversible ΔT_{ad} is deduced from the reversible ΔS_M data in **Fig. 6.6(c)** and the C_p values shown in **Fig. 6.7(a)**. **Figure 6.7(b)** represents the ΔT_{ad} as a function of temperature. A maximum reversible ΔT_{ad} ~6.7 K is obtained in all-*d*-$Ni_{36}Co_{14}Mn_{34.5}Ti_{15.5}$ alloys and this magnitude is large and comparable to other Ni-Mn-X Heusler alloys [10,38,40,53,63].

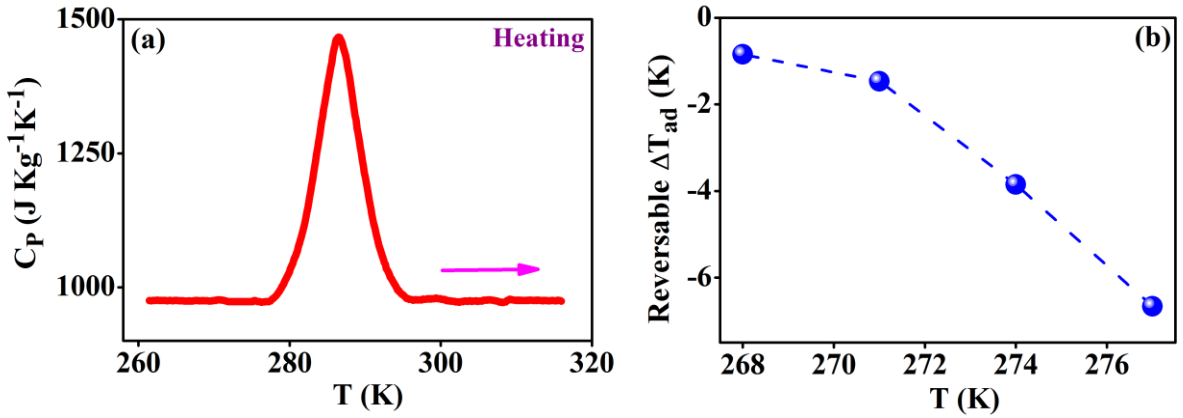

Figure 6.7: (a) Temperature dependent-specific heat capacity (c_p) under zero-field for the $Ni_{36}Co_{14}Mn_{34.5}Ti_{15.5}$ alloy recorded during heating mode. (b) Reversible ΔT_{ad} vs T(K) under 5 T.

6.3.5 *Cyclical stability from DSC measurement*

Cyclic stability of phase transformation plays a significant role on the functional fatigue behaviour of the MCE materials. **Fig. 6.8(a)** displays the thermal cycling DSC heat-flow measurements up to 35th cycles for the x = 1 alloy and their respective characterizes temperatures vs. cycle are presented in **Fig. 6.8(b)**. It is clear from the figure that the peak positions and height of the DSC heating cooling curves remain almost unchanged and no significant shift of the characteristics temperatures is observed over 35 thermal cycles.

Therefore, this observation confirms that the phase transition posses good reversibility and stability in our system.

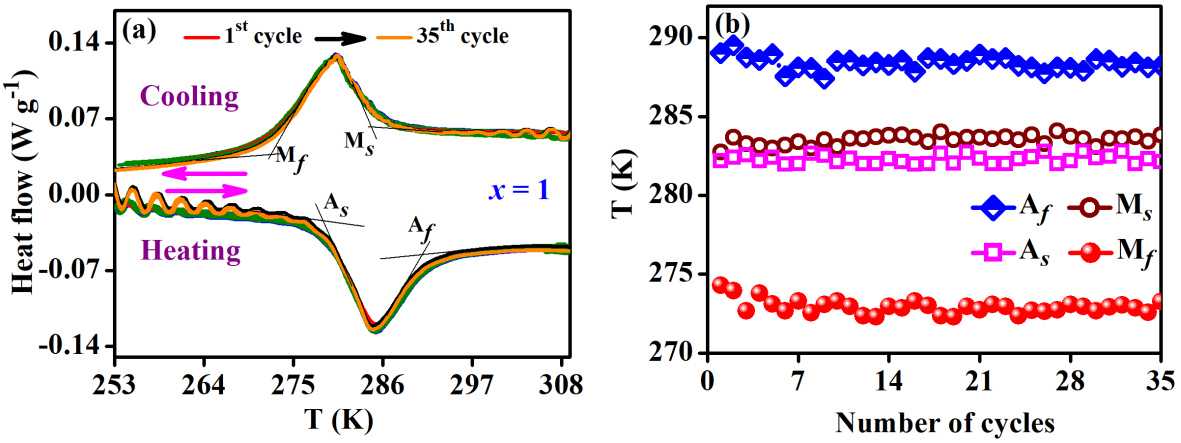

Figure 6.8: (a) DSC heat flow vs temperature curves measured during heating and cooling, and (b) the transformation temperatures for x = 1 sample.

6.3.6 Magnetoresistance

To evaluate the reversible magnetoresistance (MR) properties of the present system, the temperature and magnetic field dependent electrical resistivity are measured. **Fig. 6.9(a)** illustrates the temperature-dependent resistivity $\rho(T)$ under the magnetic field of 0 T and 5 T, measured using the same protocol as before. A large drop in resistivity is observed around the MST. This is ascribed to the change in the electronic density of state at the Fermi level due to the lattice distortion during the phase transformation [64]. Under 5 T, A_S is reduced by 11 K with $dT_A/d\mu_0 H$~2.2 K/T. From the CC equation, a certain temperature gap between the resistivity curve at 259.6 K (A_S) upon 5 T to 277.3 K (M_S) under 0 T, which suggests to get a partial reversible behaviour of MR in the abovementioned temperature range.

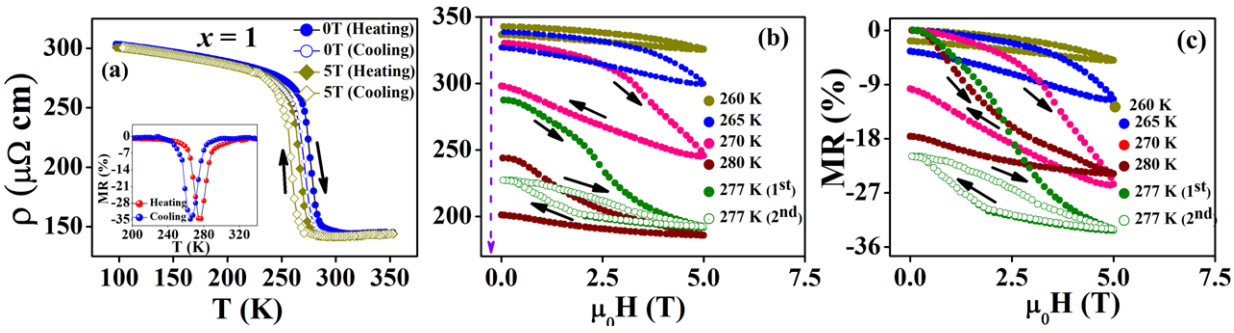

Figure 6.9: (a) Temperature-dependent electrical resistivity (ρ-T) curves measured of x = 1 sample upon heating and cooling, with 0 and 5 T. Inset shows the corresponding their temperature dependence of MR. (b) Field dependence resistivity (ρ- μ_0H) at various temperature upon heating mode across the transition temperatures under 35 thermal cycles for x = 1 sample and (c) corresponding MR. The green hollow circle and star represent 2nd cycle ρ-H at 277 K after 1st cycle of magnetic field.

The temperature dependence of MR under a magnetic field change of $\mu_0 H$ during heating is obtained from the following equation as plotted in the inset of **Fig. 6.9(a)**.

$$MR = \left[\frac{\{R(\mu_0 H) - R(0)\}}{R(0)}\right] \times 100\% \qquad (6.7)$$

Where, $R(\mu_0 H)$ and $R(0)$ are the electrical resistance under $\mu_0 H$ and zero field, respectively. A maximum MR value of -32.6% across the IMT is found due to the field change of 5T which is comparable to other Ni-Mn-based Heusler alloys [65–67]. This large negative MR is because the electrical resistance in the austenite state is much lower than that the martensite phase. When magnetic field produce the field-induced transformation from martensitic state to the cubic austenite state, leading to the large negative MR.

Figure 6.9(b) shows field dependent resistivity taken in the vicinity of IMT and the corresponding field dependence MR is exhibited in **6.9(c)**, respectively. It is observed that at 300 K, the sample is in the fully austenite phase with no significant change in the MR when a field is applied. Towards the transition on heating, for example, at 265, 270, and 277 K, the field-induced IMT is induced by the field. It is interesting to note that the peak value of MR increases with the measured temperature range due to the enhancement of the martensite volume fraction by the application of magnetic field of 5 T when the sample goes at the middle of the transition. Upon removal of the field from 5 T, the MR does not reverse entirely into the initial state. As a result, a reduced reversible MR of about 14% out of 32.6% is obtained at 277

K for the second and subsequent field cyclic measurements. In view of practical application, it would be essential to tailor the composition in this system so that a large reversible MR can be obtained near room temperature.

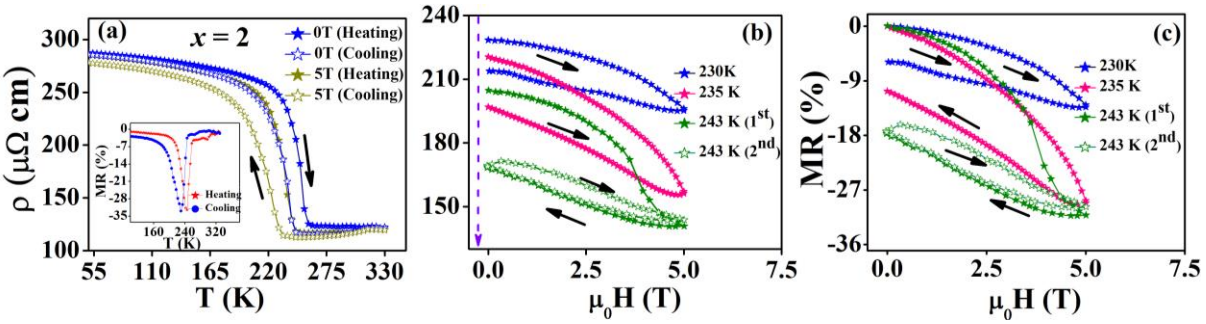

Figure 6.10: (a) (ρ-T) curves measured of *x* = 2 sample taken from heating and cooling sequence with 0 and 5 T. Inset shows the corresponding their temperature dependence of MR. (b) The field dependence resistivity (ρ- μ_0H) at various temperature upon heating mode across the transition temperatures under 35 thermal cycles for *x* = 1 sample and (c) corresponding MR of *x* =2 samples. The green hollow circle and star represent 2nd cycle ρ-H 243 K after 1st cycle of magnetic field.

To compare reversible MR of sample *x* = 1 with *x* = 2, the analogous $\rho(T)$ and ρ-μ_0H measurements are performed in **Fig. 6.10(a)-(c)**. The similar trend about the decrease of A_S by 17.1 K with $dT_A/d\mu_0 H$~3.4 K/T is observed, which is well agreement with the result from M-T curve. Like *x* = 1, a partial reversible field-induced IMT may occurs between 232.8 K (A_S) upon 5 T and 250.3 K (M_S) under 0 T. **Figure 6.10(b)** and **6.10(c)** shows field-dependent resistivity around the IMT temperature and corresponding MR in the reverse IMT region of *x* = 1 sample. It is observed from **Fig. 6.10(b)** that at 230K and 235 K, the resistivity is found to decrease with rising temperature and very weak field-induced transition occurs with increasing the magnetic field. So, for finding reversible MR, second cycle ρ-μ_0H curve are also record with the first one at 243 K.

Unfortunately, at the middle of the transition temperature~243 K, large fraction of residual austenite of the first field descending cycle persists for subsequent field cycling. Because of that, a relatively small reversible MR of about 13.1 % during the second cycle of the total MR ~31.2 % during first cycle at 243 K is obtained. Thus, this *x* = 2 sample require high magnetic field to induce a complete and reversible phase transformation which badly limit their practical utilization. Therefore, relatively large temperature window of the reversible MR and most

importantly near room temperature working temperature highly favors the sample x = 1 as magnetic actuator for technological application.

6.4 Conclusion

In this chapter, we have experimentally investigated the reversible magnetocaloric effect and magnetoresistance using different measurement protocols. The reversibility of magnetoresponsive properties relies on the two competing factors. Field-induced shift of the transformation temperatures is one factor and the other factor is the width of the hysteresis. We have optimised x = 1 sample through a systematically tuning of little at.% of Co substitution in Ni site in all-*d*-metal Heusler alloy, in which a small ΔT_{hys}, narrow ΔT_{int} and improved sensitivity 2.8 K/T is observed. The origin of the small ΔT_{hys}+ΔT_{int} is linked to the middle eigenvalue i.e., $\lambda_2 = 1.0065$ of the transformation stretch matrix **U** which is closed to one, confirming good geometrical compatibility between cubic austenite and monoclinic martensitic phases. Moreover, the minor hysteresis loop has been performed in order to reduce the thermal hysteresis as well as enhance reversibility of our system. A large reversible ΔS_M~17.78 Jkg^{-1}K^{-1} at 277 K over a broad temperature window ~ 12 K under 5 T has been obtained in the studied sample. This result represents 91% of the total magnetic entropy change of 19.78 Jkg^{-1}K^{-1}, obtained at the first magnetic field ramp at the same temperature. Moreover, due to partial reversible field-induced MST, a large reversible MR of 14% out of 32.6% is observed. Our results provide a feasible pathway to improve the reversible magnetoresponsive properties across the martensitic transition in all-*d*-Ni(Co)-Mn-Ti Heusler alloys. Therefore, these findings in all-*d*-metal Heusler alloys can explore a cyclically stable caloric material with small hysteresis for magnetic refrigeration and magnetic recording applications.

References:

[1] A. Gschneidner, V. K. Pecharsky, and A. O. Tsokol, *Recent Developments in Magnetocaloric Materials*, Reports Prog. Phys. **68**, 1479 (2005).

[2] V. K. Pecharsky and K. A. Gschneidner, Jr., *Giant Magnetocaloric Effect in Gd5(Si2Ge2)*, Phys. Rev. Lett. **78**, 4494 (1997).

[3] L. Jia, J. R. Sun, J. Shen, Q. Y. Dong, J. D. Zou, B. Gao, T. Y. Zhao, H. W. Zhang, F. X. Hu, and B. G. Shen, *Magnetocaloric Effects in the La (Fe,Si) 13 Intermetallics Doped by Different Elements*, J. Appl. Phys. **105**, 7 (2009).

[4] V. Franco, J. S. Blázquez, J. J. Ipus, J. Y. Law, L. M. Moreno-Ramírez, and A. Conde, *Magnetocaloric Effect: From Materials Research to Refrigeration Devices*, Prog. Mater. Sci. **93**, 112 (2018).

[5] O. Gutfleisch, T. Gottschall, M. Fries, D. Benke, I. Radulov, K. P. Skokov, H. Wende, M. Gruner, M. Acet, P. Entel, and M. Farle, *Mastering Hysteresis in Magnetocaloric Materials*, Philos. Trans. R. Soc. A **374**, 20150308 (2016).

[6] E. Liu, W. Wang, L. Feng, W. Zhu, G. Li, J. Chen, H. Zhang, G. Wu, C. Jiang, H. Xu, and F. de Boer, *Stable Magnetostructural Coupling with Tunable Magnetoresponsive Effects in Hexagonal Ferromagnets*, Nat. Commun. **3**, 873 (2012).

[7] T. Samanta, D. L. Lepkowski, A. U. Saleheen, A. Shankar, J. Prestigiacomo, I. Dubenko, A. Quetz, I. W. H. Oswald, G. T. McCandless, J. Y. Chan, P. W. Adams, D. P. Young, N. Ali, and S. Stadler, *Hydrostatic Pressure-Induced Modifications of Structural Transitions Lead to Large Enhancements of Magnetocaloric Effects in MnNiSi-Based Systems*, Phys. Rev. B **91**, 020401 (2015).

[8] C. Salazar-Mejía, P. Devi, S. Singh, C. Felser, and J. Wosnitza, *Influence of Cr Substitution on the Reversibility of the Magnetocaloric Effect in Ni-Cr-Mn-In Heusler Alloys*, Phys. Rev. Mater. **5**, 104406 (2021).

[9] X. He, Y. Zhang, S. Wei, Y. Cao, K. Xu, and Z. Li, *Achievement of a Reversible Giant Magnetocaloric Effect via Exerting External Hydrostatic Pressure on a Ni 45 Co 5 Mn 35 In 15 Metamagnetic Heusler Alloy*, J. Phys. D. Appl. Phys. **54**, 165001 (2021).

[10] Y. H. Qu, D. Y. Cong, X. M. Sun, Z. H. Nie, W. Y. Gui, R. G. Li, Y. Ren, and Y. D.

Wang, *Giant and Reversible Room-Temperature Magnetocaloric Effect in Ti-Doped Ni-Co-Mn-Sn Magnetic Shape Memory Alloys*, Acta Mater. **134**, 236 (2017).

[11] S. J. Kim, W. H. Ryu, H. S. Oh, and E. S. Park, *A Large Reversible Room Temperature Magneto-Caloric Effect in Ni-TM-Co-Mn-Sn (TM = Ti, V, Cr) Meta-Magnetic Heusler Alloys*, J. Appl. Phys. **123**, 1 (2018).

[12] T. Krenke, E. Duman, M. Acet, E. F. Wassermann, X. Moya, L. Manosa, and A. Planes, *Inverse Magnetocaloric Effect in Ferromagnetic Ni-Mn-Sn Alloys*, Nat. Mater. **4**, 450 (2005).

[13] J. Liu, T. Gottschall, K. P. Skokov, J. D. Moore, and O. Gutfleisch, *Giant Magnetocaloric Effect Driven by Structural Transitions*, Nat. Mater. **11**, 620 (2012).

[14] R. Kainuma, Y. Imano, W. Ito, Y. Sutou, H. Morito, S. Okamoto, O. Kitakami, K. Oikawa, A. Fujita, T. Kanomata, and K. Ishida, *Magnetic-Field-Induced Shape Recovery by Reverse Phase Transformation*, Nature **439**, 957 (2006).

[15] Z. H. Liu, M. Zhang, Y. T. Cui, Y. Q. Zhou, W. H. Wang, G. H. Wu, X. X. Zhang, and G. Xiao, *Martensitic Transformation and Shape Memory Effect in Ferromagnetic Heusler Alloy Ni2FeGa*, Appl. Phys. Lett. **82**, 424 (2003).

[16] D. Cong, W. Xiong, A. Planes, Y. Ren, L. Mañosa, P. Cao, Z. Nie, X. Sun, Z. Yang, X. Hong, and Y. Wang, *Colossal Elastocaloric Effect in Ferroelastic Ni-Mn-Ti Alloys*, Phys. Rev. Lett. **122**, 255703 (2019).

[17] R. Kainuma, Y. Imano, W. Ito, H. Morito, Y. Sutou, K. Oikawa, A. Fujita, K. Ishida, S. Okamoto, O. Kitakami, and T. Kanomata, *Metamagnetic Shape Memory Effect in a Heusler-Type Ni43Co7Mn39Sn11 Polycrystalline Alloy*, Appl. Phys. Lett. **88**, 192513 (2006).

[18] M. Khan, I. Dubenko, S. Stadler, and N. Ali, *Exchange Bias in Bulk Mn Rich Ni-Mn-Sn Heusler Alloys*, J. Appl. Phys. **102**, (2007).

[19] L. Chen, F. X. Hu, J. Wang, L. F. Bao, J. R. Sun, B. G. Shen, J. H. Yin, and L. Q. Pan, *Magnetoresistance and Magnetocaloric Properties Involving Strong Metamagnetic Behavior in Fe-Doped Ni 45(Co 1-XFe x) 5Mn 36.6In 13.4 Alloys*, Appl. Phys. Lett. **101**, (2012).

[20] Y. Song, X. Chen, V. Dabade, T. W. Shield, and R. D. James, *Enhanced Reversibility*

and Unusual Microstructure of a Phase-Transforming Material, Nature **502**, 85 (2013).

[21] R. Zarnetta, R. Takahashi, M. L. Young, A. Savan, Y. Furuya, S. Thienhaus, B. Maaß, M. Rahim, J. Frenzel, H. Brunken, Y. S. Chu, V. Srivastava, R. D. James, I. Takeuchi, G. Eggeler, and A. Ludwig, *Identification of Quaternary Shape Memory Alloys with Near-Zero Thermal Hysteresis and Unprecedented Functional Stability*, Adv. Funct. Mater. **20**, 1917 (2010).

[22] J. Cui, Y. S. Chu, O. O. Famodu, Y. Furuya, J. Hattrick-Simpers, R. D. James, A. Ludwig, S. Thienhaus, M. Wuttig, Z. Zhang, and I. Takeuchi, *Combinatorial Search of Thermoelastic Shape-Memory Alloys with Extremely Small Hysteresis Width*, Nat. Mater. **5**, 286 (2006).

[23] L. E. L. Silva, J. C. Patiño, and A. M. Gomes, *On the Structural and Thermo-Magnetic Study of the Magnetocaloric Heusler Alloy Ni 2 Mn 1-x Cu x Ga 0.8 Al 0.2*, J. Phys. Condens. Matter **33**, 235701 (2021).

[24] A. A. Mendonça, L. Ghivelder, P. L. Bernardo, H. Gu, R. D. James, L. F. Cohen, and A. M. Gomes, *Experimentally Correlating Thermal Hysteresis and Phase Compatibility in Multifunctional Heusler Alloys*, Phys. Rev. Mater. **4**, 114403 (2020).

[25] E. Stern-Taulats, A. Planes, P. Lloveras, M. Barrio, J.-L. Tamarit, S. Pramanick, S. Majumdar, S. Yüce, B. Emre, C. Frontera, and L. Mañosa, *Tailoring Barocaloric and Magnetocaloric Properties in Low-Hysteresis Magnetic Shape Memory Alloys*, Acta Mater. **96**, 324 (2015).

[26] Z. Wei, Y. Shen, Z. Zhang, J. Guo, B. Li, E. Liu, Z. Zhang, and J. Liu, *Low-Pressure-Induced Giant Barocaloric Effect in an All- d -Metal Heusler Ni 35.5 Co 14.5 Mn 35 Ti 15 Magnetic Shape Memory Alloy*, APL Mater. **8**, 051101 (2020).

[27] M. Ghorbani Zavareh, C. Salazar Mejía, A. K. Nayak, Y. Skourski, J. Wosnitza, C. Felser, and M. Nicklas, *Direct Measurements of the Magnetocaloric Effect in Pulsed Magnetic Fields: The Example of the Heusler Alloy Ni50Mn35In15*, Appl. Phys. Lett. **106**, 1 (2015).

[28] Z. Y. Wei, E. K. Liu, J. H. Chen, Y. Li, G. D. Liu, H. Z. Luo, X. K. Xi, H. W. Zhang, W. H. Wang, and G. H. Wu, *Realization of Multifunctional Shape-Memory Ferromagnets in All- d -Metal Heusler Phases*, Appl. Phys. Lett. **107**, 022406 (2015).

[29] Z. Y. Wei, E. K. Liu, Y. Li, X. L. Han, Z. W. Du, H. Z. Luo, G. D. Liu, X. K. Xi, H. W. Zhang, W. H. Wang, and G. H. Wu, *Magnetostructural Martensitic Transformations with Large Volume Changes and Magneto-Strains in All- d -Metal Heusler Alloys*, Appl. Phys. Lett. **109**, 071904 (2016).

[30] A. Taubel, B. Beckmann, L. Pfeuffer, N. Fortunato, F. Scheibel, S. Ener, T. Gottschall, K. P. Skokov, H. Zhang, and O. Gutfleisch, *Tailoring Magnetocaloric Effect in All-d-Metal Ni-Co-Mn-Ti Heusler Alloys: A Combined Experimental and Theoretical Study*, Acta Mater. **201**, 425 (2020).

[31] S. Samanta, S. Ghosh, and K. Mandal, *Observation of Giant Exchange Bias Effect in Ni–Mn–Ti All-d-Metal Heusler Alloy*, J. Phys. Condens. Matter **34**, 105801 (2022).

[32] A. Aznar, A. Gràcia-Condal, A. Planes, P. Lloveras, M. Barrio, J.-L. Tamarit, W. Xiong, D. Cong, C. Popescu, and L. Mañosa, *Giant Barocaloric Effect in All-d-Metal Heusler Shape Memory Alloys*, Phys. Rev. Mater. **3**, 044406 (2019).

[33] C. Salazar Mejía, M. Ghorbani Zavareh, A. K. Nayak, Y. Skourski, J. Wosnitza, C. Felser, and M. Nicklas, *Pulsed High-Magnetic-Field Experiments: New Insights into the Magnetocaloric Effect in Ni-Mn-In Heusler Alloys*, J. Appl. Phys. **117**, 17E710 (2015).

[34] E. Cesari, D. Salas, and S. Kustov, *Entropy Changes in Ferromagnetic Shape Memory Alloys*, Mater. Sci. Forum **684**, 49 (2011).

[35] T. Kihara, X. Xu, W. Ito, R. Kainuma, and M. Tokunaga, *Direct Measurements of Inverse Magnetocaloric Effects in Metamagnetic Shape-Memory Alloy NiCoMnIn*, Phys. Rev. B **90**, 214409 (2014).

[36] P. Devi, C. S. Mejía, M. G. Zavareh, K. K. Dubey, P. Kushwaha, Y. Skourski, C. Felser, M. Nicklas, and S. Singh, *Improved Magnetostructural and Magnetocaloric Reversibility in Magnetic Ni-Mn-In Shape-Memory Heusler Alloy by Optimizing the Geometric Compatibility Condition*, Phys. Rev. Mater. **3**, 062401 (2019).

[37] T. Krenke, M. Acet, E. F. Wassermann, X. Moya, L. Mañosa, and A. Planes, *Ferromagnetism in the Austenitic and Martensitic States of Ni-Mn-In Alloys*, Phys. Rev. B **73**, 174413 (2006).

[38] X. M. Sun, D. Y. Cong, Z. Li, Y. L. Zhang, Z. Chen, Y. Ren, K.-D. Liss, Z. Y. Ma, R. G. Li, Y. H. Qu, Z. Yang, L. Wang, and Y. D. Wang, *Manipulation of Magnetostructural*

Transition and Realization of Prominent Multifunctional Magnetoresponsive Properties in NiCoMnIn Alloys, Phys. Rev. Mater. **3**, 034404 (2019).

[39] Z. Guan, X. Jiang, J. Gu, J. Bai, X. Liang, H. Yan, Y. Zhang, C. Esling, X. Zhao, and L. Zuo, *Large Magnetocaloric Effect and Excellent Mechanical Properties near Room Temperature in Ni-Co-Mn-Ti Non-Textured Polycrystalline Alloys*, Appl. Phys. Lett. **119**, 051904 (2021).

[40] J. Liu, Y. Gong, Y. You, X. You, B. Huang, X. Miao, G. Xu, F. Xu, and E. Brück, *Giant Reversible Magnetocaloric Effect in MnNiGe-Based Materials: Minimizing Thermal Hysteresis via Crystallographic Compatibility Modulation*, Acta Mater. **174**, 450 (2019).

[41] T. Gottschall, E. Stern-Taulats, L. Mañosa, A. Planes, K. P. Skokov, and O. Gutfleisch, *Reversibility of Minor Hysteresis Loops in Magnetocaloric Heusler Alloys*, Appl. Phys. Lett. **110**, 223904 (2017).

[42] A. Diestel, R. Niemann, B. Schleicher, K. Nielsch, and S. Fähler, *Reducing Hysteresis Losses by Heating Minor Loops in Magnetocaloric Ni-Mn-Ga-Co Films*, Energy Technol. **6**, 1463 (2018).

[43] T. Gottschall, K. P. Skokov, B. Frincu, and O. Gutfleisch, *Large Reversible Magnetocaloric Effect in Ni-Mn-In-Co*, Appl. Phys. Lett. **106**, (2015).

[44] P. Devi, M. Ghorbani Zavareh, C. S. Mejía, K. Hofmann, B. Albert, C. Felser, M. Nicklas, and S. Singh, *Reversible Adiabatic Temperature Change in the Shape Memory Heusler Alloy Ni 2.2 Mn 0.8 Ga: An Effect of Structural Compatibility*, Phys. Rev. Mater. **2**, 1 (2018).

[45] K. K. Dubey, P. Devi, A. K. Singh, and S. Singh, *Improved Crystallographic Compatibility and Magnetocaloric Reversibility in Pt Substituted Ni2Mn1.4In0.6 Magnetic Shape Memory Heusler Alloy*, J. Magn. Magn. Mater. **507**, 1 (2020).

[46] V. Srivastava, X. Chen, and R. D. James, *Hysteresis and Unusual Magnetic Properties in the Singular Heusler Alloy Ni45Co5Mn40Sn10*, Appl. Phys. Lett. **97**, 014101 (2010).

[47] S. Singh, P. Kushwaha, F. Scheibel, H.-P. Liermann, S. R. Barman, M. Acet, C. Felser, and D. Pandey, *Residual Stress Induced Stabilization of Martensite Phase and Its Effect on the Magnetostructural Transition in Mn-Rich Ni-Mn-In/Ga Magnetic Shape-Memory*

Alloys, Phys. Rev. B **92**, 020105 (2015).

[48] R. D. James and K. F. Hane, *Martensitic Transformations and Shape-Memory Materials*, Acta Mater. **48**, 197 (2000).

[49] K. F. Hane and T. W. Shield, *Symmetry and Microstructure in Martensites*, Philos. Mag. A **78**, 1215 (1998).

[50] L. Caron, Z. Q. Ou, T. T. Nguyen, D. T. Cam Thanh, O. Tegus, and E. Brück, *On the Determination of the Magnetic Entropy Change in Materials with First-Order Transitions*, J. Magn. Magn. Mater. **321**, 3559 (2009).

[51] S. Ghosh, S. Samanta, J. Sinha, and K. Mandal, *Measurement Protocols Dependent Giant Magnetocaloric Effect in MnNiSi-Based System*, Appl. Phys. Lett. **119**, 183901 (2021).

[52] E. Stern-Taulats, P. O. Castillo-Villa, L. Mañosa, C. Frontera, S. Pramanick, S. Majumdar, and A. Planes, *Magnetocaloric Effect in the Low Hysteresis Ni-Mn-In Metamagnetic Shape-Memory Heusler Alloy*, J. Appl. Phys. **115**, 173907 (2014).

[53] J. Liu, N. Scheerbaum, J. Lyubina, and O. Gutfleisch, *Reversibility of Magnetostructural Transition and Associated Magnetocaloric Effect in Ni–Mn–In–Co*, Appl. Phys. Lett. **93**, 102512 (2008).

[54] K. Xu, Z. Li, Y.-L. Zhang, and C. Jing, *An Indirect Approach Based on Clausius–Clapeyron Equation to Determine Entropy Change for the First-Order Magnetocaloric Materials*, Phys. Lett. A **379**, 3149 (2015).

[55] G. J. Liu, J. R. Sun, J. Shen, B. Gao, H. W. Zhang, F. X. Hu, and B. G. Shen, *Determination of the Entropy Changes in the Compounds with a First-Order Magnetic Transition*, Appl. Phys. Lett. **90**, 032507 (2007).

[56] P. J. Shamberger and F. S. Ohuchi, *Hysteresis of the Martensitic Phase Transition in Magnetocaloric-Effect Ni-Mn-Sn Alloys*, Phys. Rev. B - Condens. Matter Mater. Phys. **79**, 1 (2009).

[57] S. Y. Dan'kov, A. M. Tishin, V. K. Pecharsky, and K. A. Gschneidner, *Magnetic Phase Transitions and the Magnetothermal Properties of Gadolinium*, Phys. Rev. B **57**, 3478 (1998).

[58] L. Huang, D. Y. Cong, L. Ma, Z. H. Nie, Z. L. Wang, H. L. Suo, Y. Ren, and Y. D. Wang, *Large Reversible Magnetocaloric Effect in a Ni-Co-Mn-In Magnetic Shape Memory Alloy*, Appl. Phys. Lett. **108**, 032405 (2016).

[59] J. Liu, X. You, B. Huang, I. Batashev, M. Maschek, Y. Gong, X. Miao, F. Xu, N. van Dijk, and E. Brück, *Reversible Low-Field Magnetocaloric Effect in Ni-Mn-In-Based Heusler Alloys*, Phys. Rev. Mater. **3**, 084409 (2019).

[60] J. A. Phys, *Large Reversible Entropy Change at the Inverse Magnetocaloric Effect in Ni-Co-Mn- Ga-In Magnetic Shape Memory Alloys*, **213905**, (2015).

[61] K. K. Dubey, P. Devi, A. K. Singh, and S. Singh, *Improved Crystallographic Compatibility and Magnetocaloric Reversibility in Pt Substituted Ni2Mn1.4In0.6 Magnetic Shape Memory Heusler Alloy*, J. Magn. Magn. Mater. **507**, 166818 (2020).

[62] A. Tekgül, M. Acet, F. Scheibel, M. Farle, and N. Ünal, *The Reversibility of the Inverse Magnetocaloric Effect in Mn2−Cr Sb0.95Ga0.05*, Acta Mater. **124**, 93 (2017).

[63] Y. H. Qu, D. Y. Cong, S. H. Li, W. Y. Gui, Z. H. Nie, M. H. Zhang, Y. Ren, and Y. D. Wang, *Simultaneously Achieved Large Reversible Elastocaloric and Magnetocaloric Effects and Their Coupling in a Magnetic Shape Memory Alloy*, Acta Mater. **151**, 41 (2018).

[64] M. D. Wilding and E. W. Lee, *Superzone Boundary Effects in the Electrical Resistivity of Dysprosium*, Proc. Phys. Soc. **85**, 955 (1965).

[65] S. Chatterjee, S. Giri, S. Majumdar, and S. K. De, *Giant Magnetoresistance and Large Inverse Magnetocaloric Effect in Ni 2 Mn 1.36 Sn 0.64 Alloy*, J. Phys. D. Appl. Phys. **42**, 065001 (2009).

[66] L. Chen, F. X. Hu, J. Wang, J. Shen, J. Zhang, J. R. Sun, B. G. Shen, J. H. Yin, and L. Q. Pan, *Magnetoresistance and Magnetocaloric Effect in Metamagnetic Alloys Ni45Co5Mn36.5In13.5*, J. Appl. Phys. **107**, 09A940 (2010).

[67] M. Khan, I. Dubenko, S. Stadler, J. Jung, S. S. Stoyko, A. Mar, A. Quetz, T. Samanta, N. Ali, and K. H. Chow, *Enhancement of Ferromagnetism by Cr Doping in Ni-Mn-Cr-Sb Heusler Alloys*, Appl. Phys. Lett. **102**, 112402 (2013).

Chapter 7 Giant Exchange bias in Ni-Mn-Ti all *d*-metal Heusler alloy

An observation of the giant EB under field cooled condition in all-d-metal Heusler alloy is presented. The study of magnetic memory effect and isothermal magnetic relaxation processes suggest that the giant EB field arises due to the strong exchange coupling between ferromagnetic (FM) and antiferromagnetic (AFM) phases in the studied system at temperatures below 55 K. A well-established training effect confirms the intrinsic nature of the observed EB behavior. The influence of temperature and field on EB has also been discussed in this Chapter.

Content of this chapter has been published in: **S. Samanta,** S. Ghosh and K. Mandal, "*Observation of giant exchange bias effect in Ni–Mn–Ti all-d-metal Heusler alloy*," **J. Phys.: Condens. Matter 34 (2022) 105801 (6pp).**

7 Giant Exchange bias in Ni-Mn-Ti all *d*-metal Heusler alloy

7.1 Preface

In recent years, Ni-Mn-Z (Z = In, Sn, Sb and Ga) Heusler alloys have attracted tremendous attention towards their potential multifunctional properties like magnetocaloric effect (MCE) [1,2], magnetic shape memory effect (MSMA) [3,4], magneto-resistance (MR) [5], and exchange bias (EB) effect [6,7]. In these functionalities, exchange bias is an always attractive research topic due to its high potential impact for many technological applications like magnetoresistive random access memory (MRRAM) [8,9], magnetic recording media [10], and spin-valve devices [11]. The essential intriguing properties of EB are; asymmetry of the hysteresis loop, the magnitude of loop shift and its sign, training effect and time dependence of thermoremanent magnetization. Hence, EB is generally observed to happen due to FM unidirectional anisotropy coupling formed at distinct type of interfaces, such as FM-AFM [12], FM-ferrimagnetic(FI) [13], FM-spin glass(SG) phases [14].

Generally, in Mn-rich Ni-Mn-Z (Z = In, Sn and Sb) ferromagnetic Heusler alloys, $Mn_{regular}$-Mn_{excess} exchange interaction at Ni/Z site form AFM ordering. [15] Thus, the competition of FM and AFM phases may generate frustrated magnetic behavior and thereby, exhibits a large EB effect when the material is field cooled (FC) or zero-field cooled (ZFC) at low temperature. Observation of large EB in these systems is attributed to different mechanisms [16,17]. For instance, Ma *et al*. reported a giant conventional EB of 1.17 kOe at 5 K in $Mn_2Ni_{1.6}Sn_{0.4}$ alloy which arises from the interface exchange interaction between reentrant SG phase and FM martensitic phase [18]. $Mn_{50}Ni_{42}Sn_8$ alloy exhibits a giant EB field of 3.25 kOe at 2 K due to the strong exchange coupling between the super SG cluster formed by FM embedded in an AFM matrix [19]. On the other hand, Wang *et al*. observed a large spontaneous EB of 1.3 kOe at 10 K after ZFC from an unmagnetized state in Ni-Mn-In bulk alloys. They proposed that such large EB originates from Super-FM unidirectional anisotropy during the initial magnetization process [20]. Moreover, EB is observed in various systems such as nanostructures, bulk oxides, alloys, and thin films due to different origins [11,20–22].

In the above-mentioned **chapter 5**, we have described that Ni-Mn-Ti all-*d*-metal Heusler system have become the focus of intensive research due to their versatilities including giant elastocaloric effect [23], giant barocaloric effect [24], magnetoresistance [25], and magnetocaloric effect [26]. However, Ni_2MnTi in stoichiometric form displays an antiferromagnetic (AFM)-like ordering at low temperature ~120 K in the austenite phase as this AFM is originated from $Mn_{regular}$-Mn_{excess} interaction. Substitution of a small amounts of FM elements such as Co and Fe in Ni-site could produce Mn-Co/Fe-Mn strong FM configuration [25]. As a result, EB could be expected in this system due to this coexistence of FM and AFM phase. However, there are various mechanism such as structural disorder, impurity induced random field, that form AFM domain in the bulk polycrystalline system. In this chapter, we report an observation of giant EB field of 3.68 kOe after field cooled process in the bulk polycrystalline $Ni_{40}(FeCo)_4Mn_{36}Ti_{20}$ all *d*-metal Heusler alloy system and the physical mechanism of the EB due to the interaction of AFM and FM phase at their interface is discussed in detail.

7.2 Experimental

The $Ni_{40}(FeCo)_4Mn_{36}Ti_{20}$ alloy is prepared utilizing a typical arc melting procedure in a 4 N purity Argon environment with high purity component elements from Sigma Aldrich. The as-cast sample is wrapped in tantalum foil and annealed at 1173 K in a high vacuum quartz tube to ensure structural and chemical homogeneity. The sample is quenched in liquid nitrogen after 96 hours of heat treatment. Energy-dispersive spectroscopy (EDS) is used to assess the final composition. The sample's X-ray diffraction (XRD) pattern is determined at various temperatures utilizing SmartLab9kW, Rigaku and Cu-Kα radiation. VSM (full name) uses a physical property measuring method to do magnetic measurements (PPMS, Quantum design).

7.3 Results

7.3.1 Temperature dependence magnetic properties

To characterize the magnetic properties in $Ni_{40}(FeCo)_4Mn_{36}Ti_{20}$ material, we have measured temperature dependence (M-T) curve in presence of 100 Oe under ZFC and FC protocol, as shown in **Fig.7.1**. The ZFC curve shows a peak at T_p ~ 55 K and the splitting between ZFC and FC curves started at T_{irr}~ 200 K, pointing to the presence of different magnetic phases at low temperature. This irreversibility may be attributed to different mechanisms such as the

coexistence of FM-AFM interaction, the existence of reentrant SG, super-paramagnetic (PM) or super-SG [27], FM ordering in AFM cluster [28], and a sequence of PM to FM phases [27].

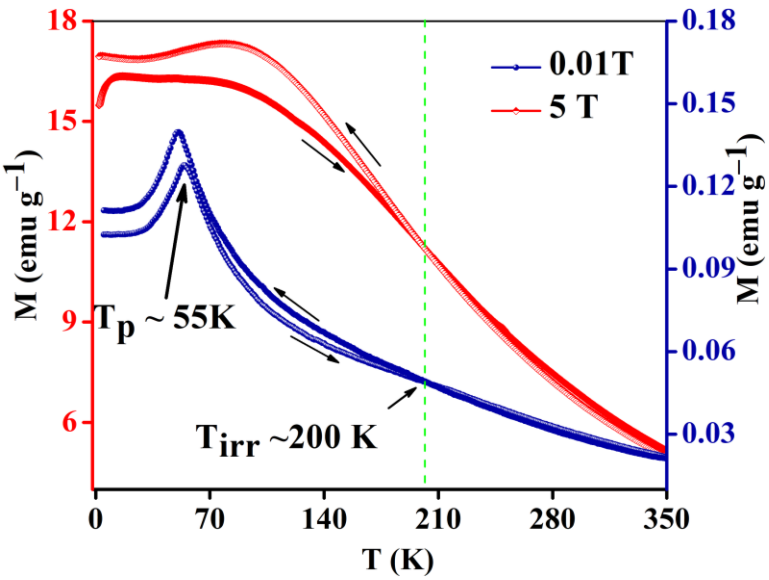

Figure 7.1: Temperature dependence magnetization in presence of 0.01T and 5 T magnetic field of Ni-Mn-Ti all-*d*-metal Heusler alloy.

To primary confirm, (*M*-*T*) curve is measured in presence of 50 kOe magnetic field. At lower field (100 Oe), ZFC curve exhibits like antiferromagnetic behaviour whereas, at large field (50 kOe), FC curve shows a signature of FM phase. We also observed that with increasing field the irreversibility increases, while irreversibility decreases in spin glass system with the field [29]. So we can suggest that the splitting of ZFC and FC curve in the austenite phase of the present system may be attributed to the FM and AFM phase coexistence.

To get about phase purity we have measured temperature dependent XRD pattern of our sample. The result shows B2-type cubic austenite phase (space group: Pm-3m) with lattice parameter a_c = 5.94 Å for the present alloy. Therefore, we can confirm that the sample does not exhibit any martensitic or secondary phases in the present system.

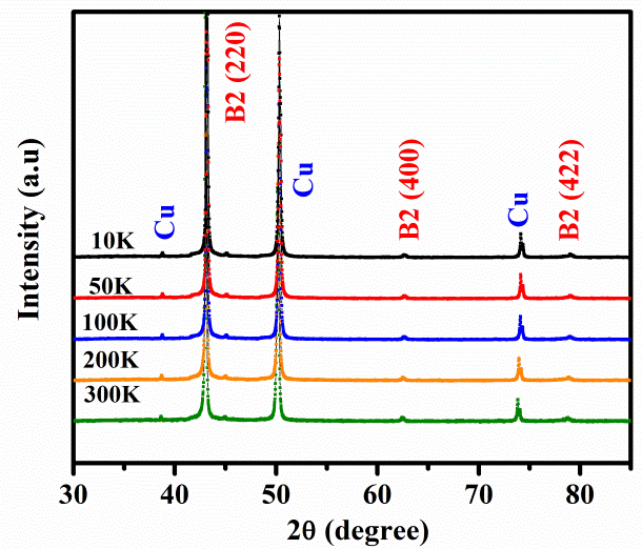

Figure 7.2: Temperature dependent XRD pattern for the present material.

7.3.2 Signature of exchange bias

At low temperatures, different magnetically inhomogeneous phases are present and subsequently, field cooling mode can yield a different magnetic domain structure than that of ZFC. For this, ZFC and FC hysteresis loops of the alloy are measured at 2 K within ± 3 T field as shown in **Fig. 7.3**. Two different measurement procedures are used to obtain a closed ZFC loop, namely **P1** and **P2**. First one is **P1** as 0→(+H)→(−H)→(+H), by which M-μ_0H loop is recorded after ZFC from zero magnetization state. From the **Fig. 7.3(a)** it is seen that the M = 0 at H = 0 of initial magnetization curve is the sign of initial un-magnetized state at 2 K [20].

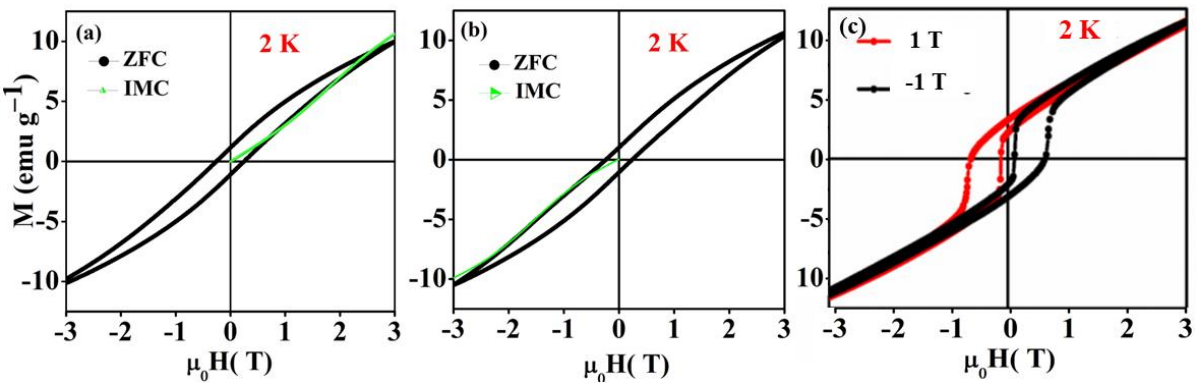

Figure 7.3: ZFC M-μ_0H loop at 2 K following (a) **P1** protocol (b) **P2** protocol. (c) FC M-μ_0H loop at 2 K, showing EB effect.

To further check, in **Fig. 7.3(b)**, ZFC M-μ_0H loop at the same temperature using second **P2** protocol (0→(−H)→(+H)→(−H)) are taken. It is further observed that ZFC M-μ_0H loops behaves symmetric behaviour i.e., do not show any loop shift along the field direction axis. Therefore, both the measurement procedures suggest that no spontaneous EB exist in the studied system like other Ni-Mn-X systems [30]. Nevertheless, the most fascinating behavior observed in FC M-μ_0H plot, which is measured during FC process in presence of +1 T and +1 T magnetic field. The shift of hysteresis loop is found towards field direction, leading to an EB effect which is displayed in **Fig. 7.3(c)**.

7.3.3 Cooling field dependence exchange bias

In order to optimize cooling field, cooling field (H_{FC}) dependence of M-μ_0H isotherms is measured at 2 K, as exhibited in **Fig. 7.4(a)**. The calculated H_{EB} and H_C at 2 K for the current alloy are plotted in **Fig. 7.4(b)**. Here, in the **Fig. 7.4(a)**, M-μ_0H loops are displayed in the field range of ± 1.5 T range for clarity. For the M-μ_0H loop measurement, a specific field is applied at RT before the measurement, and the sample is cooled to 2 K.

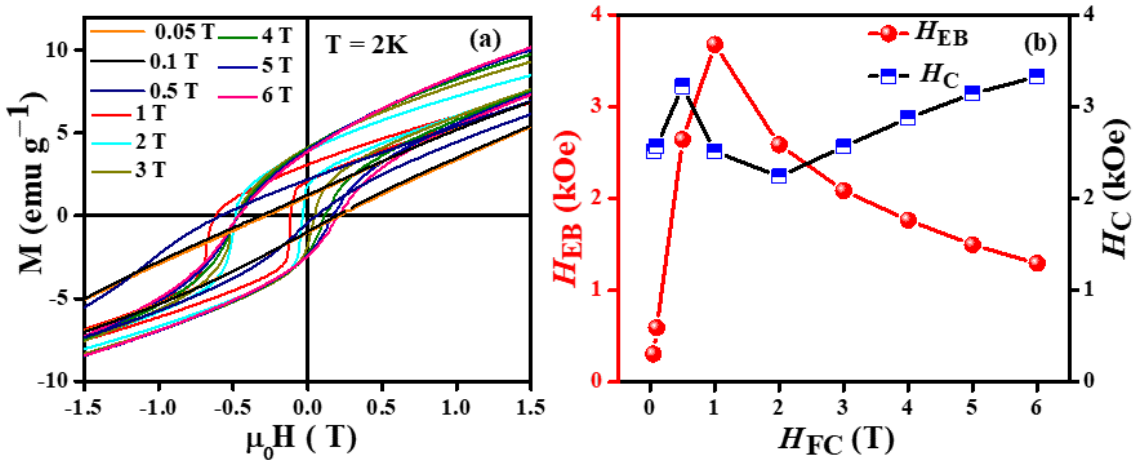

Figure 7.4. (a) M-μ_0H isotherm and (b) the obtained H_{FC} dependence of H_{EB} (left) and H_C (right) taken at 2 K for the present alloy.

Exchange bias (H_{EB}) and the coercivity (H_C) are calculated as, $H_{EB} = -|H_L + H_H|/2$ and $H_C = |H_L - H_H|/2$ where, H_L, H_H are the left and right cut-off field where magnetization becomes zero. Surprisingly, the magnitude of H_{EB} reveals a massive value of ~3.78 kOe at 2 K, which is around 3.1 times of Ni-Mn-Ti based all-*d*-metal Heusler thin film (H_{EB} ~ 1.2 kOe) [38] and also exceedingly unusual in other Ni-Mn based alloys and films [9,20,31,39,40].

The explanation might be related to the faster cooling (liquid N_2 quenching) used in our system to obtain giant EB [41].

It is noteworthy to note that H_{EB} increases substantially with H_{FC} and reaches a peak value of 3.78 kOe at H_{FC} ~ 1 T. Beyond 1T cooling field, H_{EB} decreases with increasing H_{FC} and approaches saturation for greater H_{FC}. When a modest cooling field (< 0.05 T) is applied, Zeeman coupling between FM and H_{FC} is insufficient to produce EB [19]. In the region of cooling field (0.05 < H_{FC} < 0.1 T), due to the degree of FM spin alignments increases with magnetic field in exchange interaction between FM and AFM phase increases and hence H_{EB} goes upward direction [20]. The peak of H_{EB} is observed at 1 T implying that the field is large enough to totally orient all FM spins across field direction. Beyond that H_{FC}, the rise in Zeeman coupling among FM spin and H_{FC} takes precedence over the exchange coupling, resulting in a reduction in H_{EB} at higher H_{FC}. Similar scenarios have been seen in other systems, and quantitative explanations have been offered in FM/SG matrix [42], AFM/FM phase coexisting system [32], and FM/glassy magnetic interface system [43]. Indeed, the appearance of such a peak in H_C-H_{FC} curve is not observed for SG systems [30]. Because of the increase in saturation magnetization in the FM region, H_C exhibits a rising tendency with H_{FC}.

7.3.4 Temperature dependence exchange bias

To check whether the interaction of FM cluster and AFM matrix surely occurred, **Fig. 7.5(a)** gives the M-μ_0H loop after FC protocol at different temperatures. In FC mode, the sample is cooled at 1 T from 300 K to the desired temperature. H_{EB} is found to behave a monotonic decrease with temperature and becomes almost zero above 25 K, whereas H_C approaches to zero at 35K. Similar observations are observed in other EB systems [31,32]. Different AFM grain models may explain the reduction in H_{EB} with increasing temperature [31,33,34]. In this above diagram, spheres of varying sizes indicate various AFM grain sizes, with bigger grains exhibiting less anisotropy and smaller grains exhibiting strong anisotropy. As the temperature rises from 2K to 5K, the comparatively large size AFM pinning phase is changed into the new pinned phase due to an increase in thermal activation energy, resulting in a drop in H_{EB} and an increase in H_C [31,35,37].

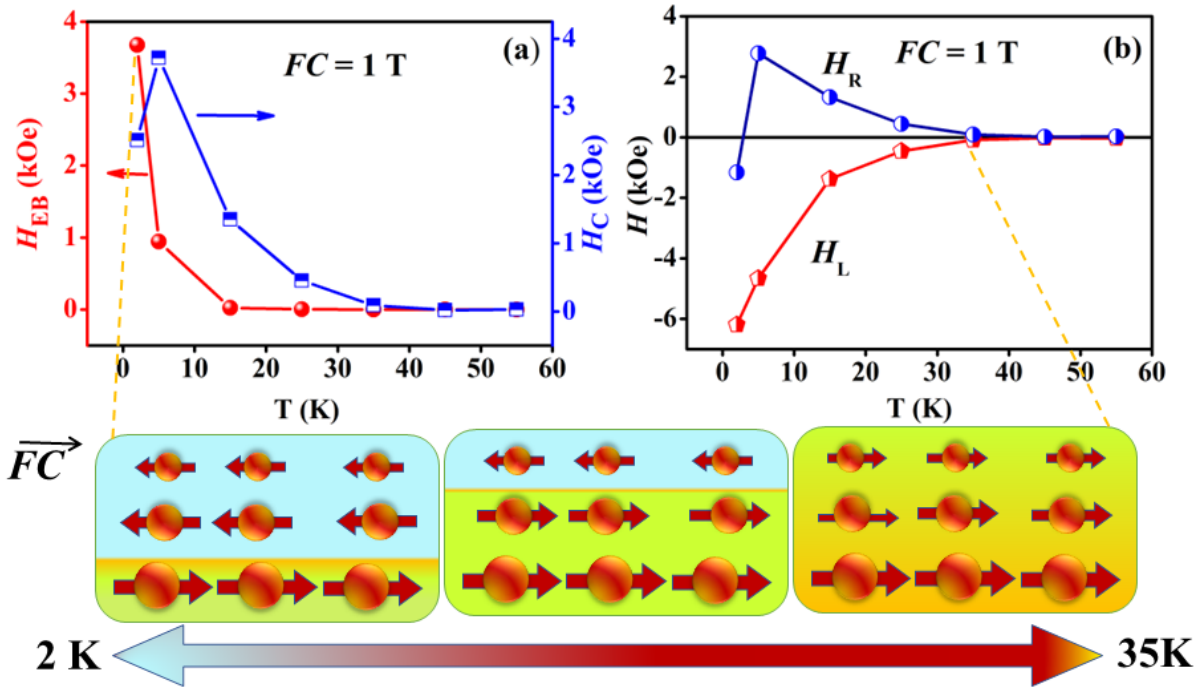

Figure 7.5: (a) H_{EB} (left) and H_C (right) are plotted at different temperatures after 1 T field cooling. (b) and corresponding the temperature dependence of left and right-side field shift. At below of the figure, a schematic diagram illustrates the movement of different AFM grain size with increasing temperature. FC and "→ n" represent the cooling field and direction of the field, respectively.

As the temperature rises, the thermal energy exceeds the pinning potential, and all magnetic pinning phases are converted to pinned phases. As a result, the hysteresis of the M-μ_0H loop associated with H_C approaches zero [28]. In contrast, H_C has a local maximum at 5 K and then drops rapidly. The maximum of H_C at 5 K might be caused by increased pinning of the propagating domain wall in the FM phases as a consequence of interfacial magnetic frustration [37]. In contrast, in the temperature range of 2 - 5 K, the H_R value crosses from – 1.17 kOe to + 2.77 kOe and subsequently falls with further temperature rise, but the H_L drops progressively with rising temperature up to 25 K and approaches zero at 35 K, as shown in **Fig. 7.5(b)**.

7.3.5 Magnetic memory effect

The fingerprint of SG and cluster SG states at low temperature in Ni-Mn based Heusler alloys are considered to be the memory effect and long-time relaxation of isothermal remanent magnetization [19,41,44,45].

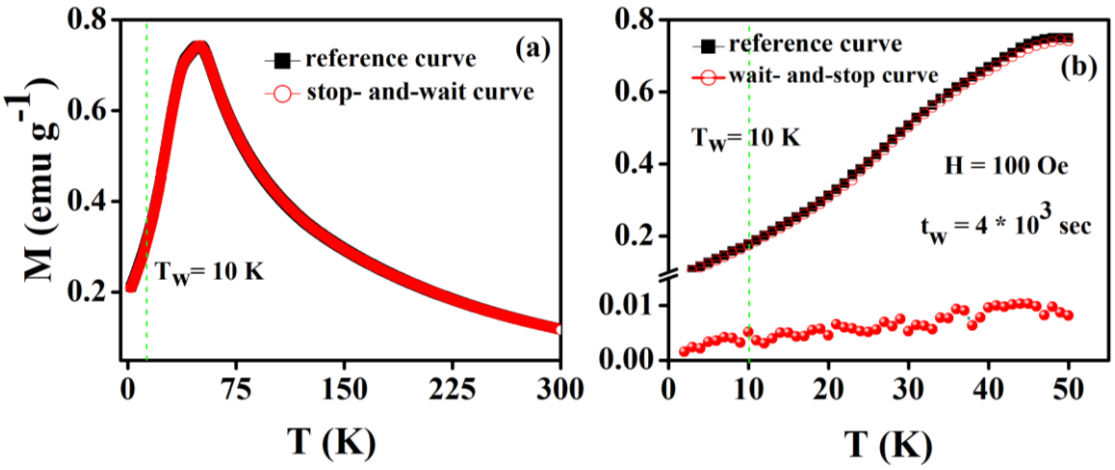

Figure 7.6: (a) Temperature dependence of ZFC magnetization curve between wait-and-stop (red opened symbol) protocol and reference curve (black solid symbol) is record in presence of 100 Oe field. (b) and their difference is plotted.

First, as seen in **Fig. 7.6**, we used the ***wait-and-stop protocol*** in the FC mode to evaluate memory effects. The sample is first cooled in ZFC mode from 300 K to 2 K, and then *M-T* (the reference curve) is recorded under 100 Oe during heating. This reference curve is levelled as the reference curve with a filled square sign in **Fig. 7.6(a).** In the ***wait-and-stop protocol***, the sample is cooled under ZFC from 300 K to an intermittent stop temperature T_w = 10 K (< T_p) and is then held for 4 x 10^3 secs before cooling to 2 K Subsequently, the *M-T* curve is recorded during heating using the same approach, as shown with open circle in **Fig. 7.6(a)**. The difference in magnetization of stop-and-wait and reference curves is also shown in **Fig. 7.6(b)**. Even after a considerable time of waiting, no change in magnetization at T_w = 10 K is detected. Thus, the sample does not recall measurement history when sample come back to the initial temperature, confirming no signature of memory effect, implying the absence of SG state at low temperature in the present system.

7.3.6 Isothermal remanent magnetization curves

In order to further elucidate the existence of SG state at low temperatures, we have measured isothermal remanent magnetization (M_{IRM}) at 10 K (< T_P) under FC protocol, as shown in **Fig. 7.7(a)**. To capture this, the sample is cooled down from RT to a waiting temperature, T_w = 10K under 500 Oe and then M_{IRM} as a function of time is measured after sudden switching off the field.

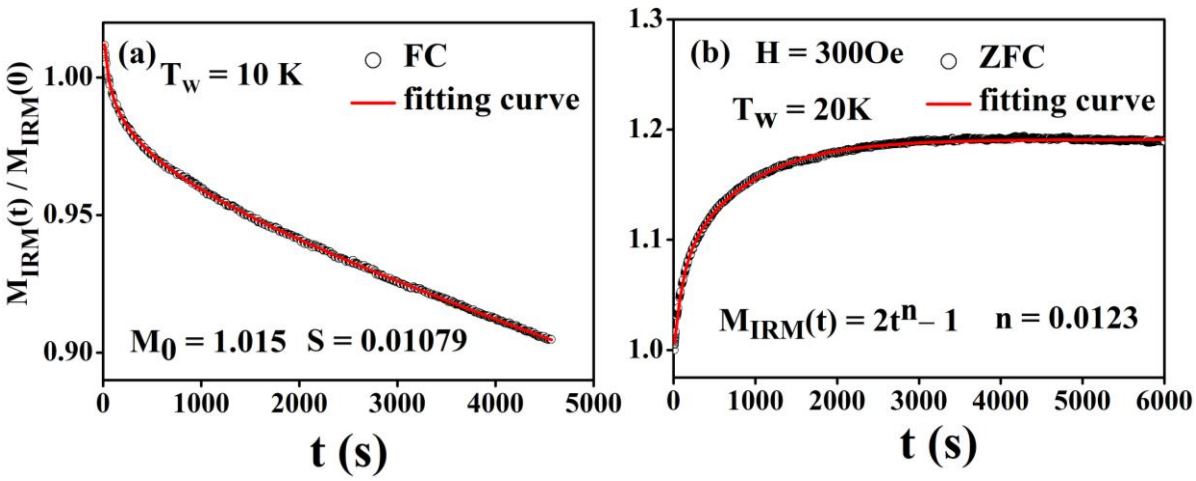

Figure 7.7: (a) Time dependent normalized isothermal remnant magnetization at 10 K in absence of magnetic field after FC (500 Oe) protocol. The red line is least square fitting using equation (**7.1**) (b) at 10K in presence of magnetic field of 300 Oe using ZFC protocols.

The experimental result reveals that the normalized isotherm curve of $M_{IRM}(t)/M_{IRM}(0)$ is well fitted by the logarithmic magnetic-viscosity law as [47],

$$M_{IRM}(t) = M_{IRM}(0) - S \ln(1 + \frac{t}{t_0}) \quad (7.1)$$

where, M_{IRM} (0) is the initial magnetization at t = 0 and S is the magnetic viscosity constant. The time dependence of remanent magnetization is known as magnetic viscosity. The coefficient t_o is dependent on the magnetometer's measurement circumstances and has a physical relevance constraint. Within a short time period, the magnitude of the normalized isotherm decays by ~ 10% from the M_{IRM} (0) value. Furthermore, S = 0.0108 was found from the fitting curve, which is extremely near to S = 0.0172 in Gd_2PdSi_3 alloy where no SG state is observed at low temperature [47].

To rule out the SG state even further, we measured ZFC relaxation in the presence of 300 Oe at the same temperature ~10 K (< T_p) for 7 × 10^3 s, as shown in **Fig. 7.7(b)**. It is seen that the magnetization value reaches its saturation in a very short time frame (~2400 s). The experimental data are fitted to the following equation,

$$M_{IRM}(t) = 2t^n - 1 \quad (7.2)$$

where, n denotes the strength of dipolar interaction among the magnetic clusters involved in the relaxation process. The lower value of n (= 0.0123) suggests weak dipolar interaction at low temperatures, confirming the lack of an SG state in the current system [45,47].

7.3.7 Training effect

Training effect is the inherent characteristic of the exchange bias effect that has been also examined through repetitive field cycling after FC condition. Because EB has several technical applications, a thorough knowledge of the training effect may result in technological benefits. For this purpose, cyclic M-μ_0H hysteresis loops are recorded at 2 K in sequential n = 8 cycles during FC in the presence of H_{FC} =1 T, as illustrated in **Fig. 7.8(a)**.

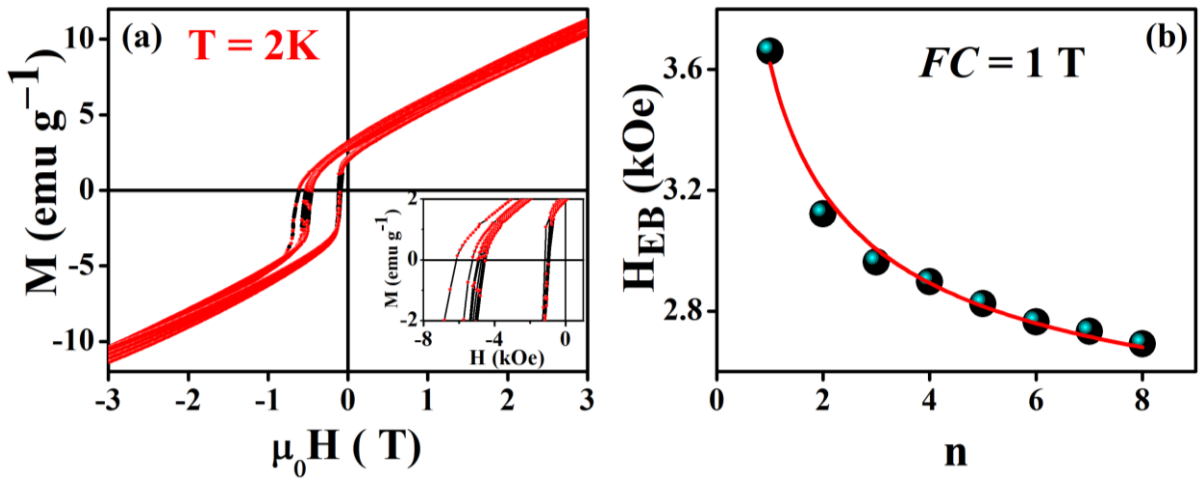

Figure 7.8: (a) Variation of H_{EB} with number of field cycle n. The green sphere circle shows the experimental data and solid red line is the fitting line giving in equation (7.3). The inset shows training effect on the M-μ_0H loops.

The nonequilibrium character of the spin in AFM domains causes the training effect [40,48,49]. When the FM domain switches back and forth under the field cycling, a relaxation of spin configurations of AFM domain towards the equilibrium is occurred due to the surface drag of the exchange interaction. In our system, the gradual decrease in H_{EB} with n is observed. Indeed, for the FM/AFM interface system, magnetic frustrations are necessary for the existence of training effect [49], and the data for the number of cycles, is fitted using the empirical model.

$$(H_{EB}^{1} - H_{EB}^{n}) \propto \sqrt{n} \qquad \textbf{(7.3)}$$

where, H_{EB}^{n} is the EB field at nth number of cycle. It is seen that the data for n > 1 is well fitted in our system and also other EB systems [7,50]. Therefore, the EB associated with a well-defined training impact has been developed.

7.4 Conclusion

In summary, a magnitude of giant exchange bias field of about 3.68 kOe in all-*d*-metal $Ni_{40}(FeCo)_4Mn_{36}Ti_{20}$ Heusler alloy at 2 K has been observed which is higher than that of reported other Ni-Mn-based alloys and thin films. The giant EB field is caused due to the unidirectional anisotropy between FM and AFM interaction at their interface which is examined through the magnetic measurement including magnetic relaxation using ZFC and FC procedure and magnetic memory effect. In addition, the observation of training effect further verified the intrinsic nature of EB phenomenon in the present system. Therefore, the present result provides a pathway to the development of rare-earth free exchange-biased hard magnet and this inexpensive all 3*d*-metal Heusler alloys are found to be potential candidate for various applications due to their giant exchange bias properties.

References:

[1] J. Liu, T. Gottschall, K. P. Skokov, J. D. Moore, and O. Gutfleisch, *Giant Magnetocaloric Effect Driven by Structural Transitions*, Nat. Mater. **11**, 720 (2012).

[2] A. Ghosh and K. Mandal, *Effect of Fe Substitution on the Magnetic and Magnetocaloric Properties of Mn-Rich Mn-Ni-Fe-Sn off-Stoichiometric Heusler Alloys*, J. Appl. Phys. **117**, 093909 (2015).

[3] Z. H. Liu, M. Zhang, Y. T. Cui, Y. Q. Zhou, W. H. Wang, G. H. Wu, X. X. Zhang, and G. Xiao, *Martensitic Transformation and Shape Memory Effect in Ferromagnetic Heusler Alloy Ni2FeGa*, Appl. Phys. Lett. **82**, 424 (2003).

[4] C. Salazar Mejía, R. Küchler, A. K. Nayak, C. Felser, and M. Nicklas, *Uniaxial-Stress Tuned Large Magnetic-Shape-Memory Effect in Ni-Co-Mn-Sb Heusler Alloys*, Appl. Phys. Lett. **110**, 0 (2017).

[5] L. Chen, F. X. Hu, J. Wang, L. F. Bao, J. R. Sun, B. G. Shen, J. H. Yin, and L. Q. Pan, *Magnetoresistance and Magnetocaloric Properties Involving Strong Metamagnetic Behavior in Fe-Doped Ni 45(Co 1-XFe x) 5Mn 37.7In 13.4 Alloys*, Appl. Phys. Lett. **101**, 1 (2012).

[7] C. Hou, H. Fujiwara, K. Zhang, A. Tanaka, and Y. Shimizu, *Temperature Dependence of the Exchange-Bias Field of Ferromagnetic Layers Coupled with Antiferromagnetic Layers*, Phys. Rev. B - Condens. Matter Mater. Phys. **73**, 1 (2001).

[7] J. F. Qian, A. K. Nayak, G. Kreiner, W. Schnelle, and C. Felser, *Exchange Bias up to Room Temperature in Antiferromagnetic Hexagonal Mn 3 Ge*, J. Phys. D. Appl. Phys. **47**, 305001 (2014).

[8] S. N. Piramanayagam, *Perpendicular Recording Media for Hard Disk Drives*, J. Appl. Phys. **102**, 011301 (2007).

[9] S. S. P. Parkin, K. P. Roche, M. G. Samant, P. M. Rice, R. B. Beyers, R. E. Scheuerlein, E. J. O'Sullivan, S. L. Brown, J. Bucchigano, D. W. Abraham, Y. Lu, M. Rooks, P. L. Trouilloud, R. A. Wanner, and W. J. Gallagher, *Exchange-Biased Magnetic Tunnel Junctions and Application to Nonvolatile Magnetic Random Access Memory (Invited)*, J. Appl. Phys. **85**, 5828 (1999).

[10] A. López-Ortega, M. Estrader, G. Salazar-Alvarez, A. G. Roca, and J. Nogués, *Applications of Exchange Coupled Bi-Magnetic Hard/Soft and Soft/Hard Magnetic Core/Shell Nanoparticles*, Phys. Rep. **553**, 1 (2015).

[11] J. Nogués and I. K. Schuller, *Exchange Bias*, J. Magn. Magn. Mater. **192**, 203 (1999).

[12] M. Khan, I. Dubenko, S. Stadler, and N. Ali, *Exchange Bias in Bulk Mn Rich Ni–Mn–Sn Heusler Alloys*, J. Appl. Phys. **102**, 113914 (2007).

[13] S. M. Watson, T. Hauet, J. A. Borchers, S. Mangin, and E. E. Fullerton, *Interfacial Magnetic Domain Wall Formation in Perpendicular-Anisotropy, Exchange-Spring Films*, Appl. Phys. Lett. **92**, 1 (2008).

[14] R. Pradheesh, H. S. Nair, V. Sankaranarayanan, and K. Sethupathi, *Exchange Bias and Memory Effect in Double Perovskite Sr 2FeCoO 7*, Appl. Phys. Lett. **101**, 1 (2012).

[15] S. Singh, L. Caron, S. W. D'Souza, T. Fichtner, G. Porcari, S. Fabbrici, C. Shekhar, S. Chadov, M. Solzi, and C. Felser, *Large Magnetization and Reversible Magnetocaloric Effect at the Second-Order Magnetic Transition in Heusler Materials*, Adv. Mater. **28**, 3321 (2017).

[17] R. Machavarapu and G. Jakob, *Exchange Bias Effect in the Martensitic State of Ni-Co-Mn-Sn Film*, Appl. Phys. Lett. **102**, 232407 (2013).

[17] Z. Li, C. Jing, J. Chen, S. Yuan, S. Cao, and J. Zhang, *Observation of Exchange Bias in the Martensitic State of Ni50Mn37Sn14 Heusler Alloy*, Appl. Phys. Lett. **91**, 112505 (2007).

[18] L. Ma, W. H. Wang, J. B. Lu, J. Q. Li, C. M. Zhen, D. L. Hou, and G. H. Wu, *Coexistence of Reentrant-Spin-Glass and Ferromagnetic Martensitic Phases in the Mn 2 Ni 1.7 Sn 0.4 Heusler Alloy*, Appl. Phys. Lett. **99**, 182507 (2011).

[19] J. Sharma and K. G. Suresh, *Observation of Giant Exchange Bias in Bulk Mn50Ni42Sn8 Heusler Alloy*, Appl. Phys. Lett. **107**, 0 (2015).

[20] B. M. Wang, Y. Liu, P. Ren, B. Xia, K. B. Ruan, J. B. Yi, J. Ding, X. G. Li, and L. Wang, *Large Exchange Bias after Zero-Field Cooling from an Unmagnetized State*, Phys. Rev. Lett. **107**, 077203 (2011).

[21] M. Estrader, A. López-Ortega, S. Estradé, I. V. Golosovsky, G. Salazar-Alvarez, M.

Vasilakaki, K. N. Trohidou, M. Varela, D. C. Stanley, M. Sinko, M. J. Pechan, D. J. Keavney, F. Peiró, S. Suriñach, M. D. Baró, and J. Nogués, *Robust Antiferromagnetic Coupling in Hard-Soft Bi-Magnetic Core/Shell Nanoparticles*, Nat. Commun. **4**, 1 (2013).

[22] M. Perzanowski, M. Marszalek, A. Zarzycki, M. Krupinski, A. Dziedzic, and Y. Zabila, *Influence of Superparamagnetism on Exchange Anisotropy at CoO/[Co/Pd] Interfaces*, ACS Appl. Mater. Interfaces **8**, 28159 (2017).

[23] D. Cong, W. Xiong, A. Planes, Y. Ren, L. Mañosa, P. Cao, Z. Nie, X. Sun, Z. Yang, X. Hong, and Y. Wang, *Colossal Elastocaloric Effect in Ferroelastic Ni-Mn-Ti Alloys*, Phys. Rev. Lett. **122**, 255703 (2019).

[24] A. Aznar, A. Gràcia-Condal, A. Planes, P. Lloveras, M. Barrio, J.-L. Tamarit, W. Xiong, D. Cong, C. Popescu, and L. Mañosa, *Giant Barocaloric Effect in All-d-Metal Heusler Shape Memory Alloys*, Phys. Rev. Mater. **3**, 044407 (2019).

[25] Z. Y. Wei, E. K. Liu, J. H. Chen, Y. Li, G. D. Liu, H. Z. Luo, X. K. Xi, H. W. Zhang, W. H. Wang, and G. H. Wu, *Realization of Multifunctional Shape-Memory Ferromagnets in All- d -Metal Heusler Phases*, Appl. Phys. Lett. **107**, 022407 (2015).

[27] A. Taubel, B. Beckmann, L. Pfeuffer, N. Fortunato, F. Scheibel, S. Ener, T. Gottschall, K. P. Skokov, H. Zhang, and O. Gutfleisch, *Tailoring Magnetocaloric Effect in All-d-Metal Ni-Co-Mn-Ti Heusler Alloys: A Combined Experimental and Theoretical Study*, Acta Mater. **201**, 425 (2020).

[27] P. Liao, C. Jing, X. L. Wang, Y. J. Yang, D. Zheng, Z. Li, B. J. Kang, D. M. Deng, S. X. Cao, J. C. Zhang, and B. Lu, *Strongly Enhanced Antiferromagnetism and Giant Spontaneous Exchange Bias in Ni50Mn37Co4Sn10 Heusler Alloy*, Appl. Phys. Lett. **104**, (2014).

[28] A. K. Nayak, M. Nicklas, S. Chadov, C. Shekhar, Y. Skourski, J. Winterlik, and C. Felser, *Large Zero-Field Cooled Exchange-Bias in Bulk Mn 2 PtGa*, Phys. Rev. Lett. **110**, 127204 (2013).

[29] A. K. Nayak, M. Nicklas, S. Chadov, P. Khuntia, C. Shekhar, A. Kalache, M. Baenitz, Y. Skourski, V. K. Guduru, A. Puri, U. Zeitler, J. M. D. Coey, and C. Felser, *Design of Compensated Ferrimagnetic Heusler Alloys for Giant Tunable Exchange Bias*, Nat.

Mater. **14**, 779 (2015).

[30] Z. D. Han, B. Qian, D. H. Wang, P. Zhang, X. F. Jiang, C. L. Zhang, and Y. W. Du, *Magnetic Phase Separation and Exchange Bias in Off-Stoichiometric Ni-Mn-Ga Alloys*, Appl. Phys. Lett. **103**, 0 (2013).

[31] H. Pan, L. Ma, G. K. Li, L. Y. Jia, C. M. Zhen, D. L. Hou, W. H. Wang, E. K. Liu, J. L. Chen, and G. H. Wu, *Large Exchange Bias Effect in the Super Spin Glass State of Mn 50 Ni 38 Al 12 Alloy*, Intermetallics **87**, 117 (2017).

[32] P. Song, L. Ma, G. K. Li, C. M. Zhen, C. Wang, E. K. Liu, W. H. Wang, J. L. Chen, G. H. Wu, Y. H. Xia, J. Zhang, C. M. Xie, H. Li, and D. L. Hou, *Dynamic Magnetic-Transformation-Induced Exchange Bias in [α-Fe2O3]0.1[FeTiO3]0.9*, Phys. Rev. Appl. **11**, 054018 (2019).

[33] K. Younsi, V. Russier, and L. Bessais, *Structure and Magnetic Properties of Nanocrystalline PrCo3*, J. Appl. Phys. **107**, 083917 (2010).

[34] A. K. Nayak, R. Sahoo, K. G. Suresh, A. K. Nigam, X. Chen, and R. V. Ramanujan, *Anisotropy Induced Large Exchange Bias Behavior in Ball Milled Ni–Co–Mn–Sb Alloys*, Appl. Phys. Lett. **98**, 232502 (2011).

[35] L. Ma, W. H. Wang, J. B. Lu, J. Q. Li, C. M. Zhen, D. L. Hou, and G. H. Wu, *Coexistence of Reentrant-Spin-Glass and Ferromagnetic Martensitic Phases in the Mn 2 Ni 1.7 Sn 0.4 Heusler Alloy*, Appl. Phys. Lett. **99**, 182507 (2011).

[37] P. Liao, C. Jing, X. L. Wang, Y. J. Yang, D. Zheng, Z. Li, B. J. Kang, D. M. Deng, S. X. Cao, J. C. Zhang, and B. Lu, *Strongly Enhanced Antiferromagnetism and Giant Spontaneous Exchange Bias in Ni 50 Mn 37 Co 4 Sn 10 Heusler Alloy*, Appl. Phys. Lett. **104**, 092410 (2014).

[37] C. Leighton, J. Nogués, B. J. Jönsson-Åkerman, and I. K. Schuller, *Coercivity Enhancement in Exchange Biased Systems Driven by Interfacial Magnetic Frustration*, Phys. Rev. Lett. **84**, 3477 (2000).

[38] K. Liu, S. C. Ma, Z. S. Zhang, X. W. Zhao, B. Yang, D. H. Wang, S. Ur Rehman, and Z. C. Zhong, *Giant Exchange Bias Effect in All-3 d -Metal Ni 38.8 Co 2.9 Mn 37.9 Ti 20.4 Thin Film*, Appl. Phys. Lett. **117**, 022412 (2020).

[39] D. W. Zhao, G. K. Li, S. Q. Wang, L. Ma, C. M. Zhen, D. L. Hou, W. H. Wang, E. K.

Liu, J. L. Chen, and G. H. Wu, *Tuning Exchange Bias by Co Doping in Mn 50 Ni 41− x Sn 9 Co x Melt-Spun Ribbons*, J. Appl. Phys. **117**, 103910 (2014).

[40] A. K. Nayak, K. G. Suresh, and A. K. Nigam, *Observation of Enhanced Exchange Bias Behaviour in NiCoMnSb Heusler Alloys*, J. Phys. D. Appl. Phys. **42**, 115004 (2009).

[41] L. Ma, W. H. Wang, J. B. Lu, J. Q. Li, C. M. Zhen, D. L. Hou, and G. H. Wu, *Coexistence of Reentrant-Spin-Glass and Ferromagnetic Martensitic Phases in the Mn2Ni1.7Sn0.4 Heusler Alloy*, Appl. Phys. Lett. **99**, 2009 (2011).

[42] M. Patra, S. Majumdar, and S. Giri, *Grain Size Effect on the Magnetic Cluster-Glass Properties of La 0.88 Sr 0.12 CoO 3*, J. Phys. Condens. Matter **22**, 117001 (2010).

[43] M. Patra, K. De, S. Majumdar, and S. Giri, *Exchange Bias with Fe Substitution in LaMnO3*, Eur. Phys. J. B **58**, 377 (2007).

[44] Y. Sun, M. B. Salamon, K. Garnier, and R. S. Averback, *Memory Effects in an Interacting Magnetic Nanoparticle System*, Phys. Rev. Lett. **91**, 177207 (2003).

[45] A. Kumar and D. Pandey, *Study of Magnetic Relaxation, Memory and Rejuvenation Effects in the Cluster Spin-Glass Phase of B-Site Disordered Ca(Fe1/2Nb1/2)O3 Perovskite: Experimental Evidence for Hierarchical Model*, J. Magn. Magn. Mater. **511**, 177974 (2020).

[47] S. Majumdar, R. Mallik, E. V Sampathkumaran, P. L. Paulose, and K. V Gopalakrishnan, *Unexpected Modification of Magnetic Properties by Y Substitution in Eu2PdSi3*, Phys. Rev. B **59**, 4244 (1999).

[47] S. Pakhira, C. Mazumdar, R. Ranganathan, and S. Giri, *Magnetic Phase Inhomogeneity in Frustrated Intermetallic Compound Sm2Ni0.87Si2.87*, J. Alloys Compd. **742**, 391 (2018).

[48] A. Hoffmann, *Symmetry Driven Irreversibilities at Ferromagnetic-Antiferromagnetic Interfaces*, Phys. Rev. Lett. **93**, 097203 (2004).

[49] D. Niebieskikwiat and M. B. Salamon, *Intrinsic Interface Exchange Coupling of Ferromagnetic Nanodomains in a Charge Ordered Manganite*, Phys. Rev. B **72**, 174422 (2005).

[50] A. Hochstrat, C. Binek, and W. Kleemann, *Training of the Exchange-Bias Effect in NiO-*

Fe Heterostructures, Phys. Rev. B - Condens. Matter Mater. Phys. **77**, 1 (2002).

Chapter 8 Conclusion and Scope for future work

Here, we summarize the overall conclusions from this thesis. Depending on this work, the scope of future development is also discussed.

8 Summary and Scope for future work

8.1 Summary

This thesis is emphasized on experimental investigations performed on the novel material design and enhanced the magnitude of multifunctional properties, such as magnetocaloric effect, magnetoresistance and exchange bias from the viewpoint of competition between ferromagnetic and other structural, electronic, and other magnetic interactions in strongly correlated Mn*M'X* hexagonal system and all-*d*-metal Heusler alloys. As mentioned in the chapter 1, Mn*M'X* hexagonal system (where M, M′= transition metals, and X= boron or carbon group elements) exhibit giant magnetocaloric responses across first-order coupled magnetic and structural transition (MST) where spin and lattice degrees of freedom strongly competed.

First, we have delivered a correct and preferred measurement protocol to determine the MCE response of these MnNiSi system accurately using Maxwell relation. For this we have systematically explored MCE of $(MnNiSi)_{0.835}(FeCoGa)_{0.165}$ material across its MST (~265 K) under various measurement protocols; namely Clausius Clapeyron relation, transformation fraction method, and Maxwell equation. The overall outcomes suggest that the discontinuous heating mode can overestimate the entropy change across the MST as this mode breakdown for the case of MT, DSC and M-μ_0H curve. In the case of discontinuous cooling and field increasing mode using of Maxwell equation, MCE values are stable and accurate. Because, it exhibits field-induced metamagnetic transition across MST which implies the nature of first-order phase transition. Moreover, breakdown of universal scaling behavior calculated from temperature dependent magnetic entropy graph support this conclusion.

Based on the aforesaid measurement protocol, we have conducted our next work towards the design of the giant magnetic refrigerant materials using low-cost, rare-earth free, and non-toxic element for room-temperature solid-state-based MR technology. For this we have substituted isostructural alloy $(FeNiGa)_x$ (x = 0.16, 0.17, and 0.18) in $(MnNiSi)_{1-x}$ system and systematically study their magnetic and magnetocaloric properties. Our result shown that the

MST is pretty much reduced to room temperature from a very high temperature~ 1210 K. From the temperature dependent XRD analysis conclusively prove that structural transition, from a high temperature Ni_2In-type hexagonal (space group $P6_3/mmc$) to a low temperature TiNiSi-type orthorhombic structure (space group *Pnma*), is associated with a large change unit cell volume change 2.6% for $x = 0.17$. Therefore, the sample 0.16 and 0.17 exhibits giant isothermal magnetic entropy change of 26.2 and ~ 63.2 $Jkg^{-1}K^{-1}$, associated with a large relative cooling power (RCP) of ~ 268.8 and ~ 357.1 J/kg respectively in the vicinity of room temperature due to field change of 5 T.

Next **chapter 5**, the effect of substituting FeCo in Ni site with maintaining the same ratio in Ni site on structural, magnetocaloric, and magneto-transport properties in all-*d*-metal $Ni_{50-x}(FeCo)_xMn_{37}Ti_{13}$ (x = 16, 18, and 20) novel Heusler alloys has been investigated. Ni-Mn-Ti all-*d*-metal Heusler alloy is one of the novel system for technological application and hence related to one of the most demanding area of magnetic refrigeration based research. The result of magnetic measurement confirms that, although parent Ni_2MnTi is antiferromagnetic (AFM), the substitution of FeCo in Ni site can significantly alter AFM into ferromagnetic phase in the vicinity of MST. The MST temperature is observed to shift towards the lower temperature with increasing $(FeCo)_x$ content. These alloys display higher sensitivity and large magnetic entropy change as well as large refrigerant capacity which is almost identical over a extend temperature region. FeCo- incorporation not only changes the nature of magnetic interaction but also significantly changes their magneto-transport behaviour. Large negative magnetoresistance (MR) up to 26.1% is achieved at the field of 5 T over a broad temperature range.

Next, we have investigated magneto functional properties at first-order MST under field cycling in the aforesaid system. It has been demonstrated how thermal hysteresis and martensitic transformation can be manipulated through chemical composition tuning, magnetic field, minor hysteresis loop, and crystallographic compatibility in order to get reversible MCE properties. We first time have investigated and discussed the reversible behavior of magneto-responsive properties in little at. % of Co variation on all-*d*-metal Heusler alloys in a detailed way. The experimental findings conclude that small at.% of Co doping and minor hysteresis loop is an effective way to reduce hysteresis in order to achieve large reversible MCE parameters in all-*d*-Heusler alloys.

Since, Ni_2MnTi alloy in the stchoichiometric form, usually displays an antiferromagnetic (AFM)-like ordering at low temperature ~120 K in the austenite phase, originating from

Mn(B)-Mn(D) interaction. Ni_2MnTi material possesses strong local anisotropy due to AFM interaction in this system. Such anisotropy can create exchange interaction with FM element at the FM/AFM interface under external magnetic field when some ferromagnetic elements are substituted and hence exchange bias (EB) could be realised. Here, we doped 4% of Fe-Co in $Ni_{40}Mn_{36}Ti_{20}$ alloy. The temperature dependence of magnetic hysteresis, and training effect measurements suggest that EB is due to the to the coexistence FM and AFM phase. In order to probe further the absence of any spin-glass like phases we provided supportive experiments like memory effect, magnetic relaxation effect.

8.2 Future Scope

As mentioned in the preface, there are indeed very less investigation on this novel all-*d*-metal Heusler alloy compared to the other promising Heusler system. Hence, two branch of possible future works are briefly discussed below.

(1) In one branch of the thesis we have rigorously searched and investigated only MCE properties for the MnNiSi of the Mn*M'X* hexagonal system. As vividly mentioned in the **chapter 3** and **4**, the system exhibiting strong coupled magnetic and structural phase transition is subjected to the issue of highly brittleness properties. One can overcome this issue by introducing interstitial atom with small atomic radius, such as boron doping which would be preferable choice for future work. In the similar way, hydrostatic pressure can be added with magnetic field to tune hysteresis and magnetocaloric effect further.

(2) In the second branch of the thesis, how MST, its width, and hysteresis can be manipulated by fine tuning of chemical composition, magnetic field and minor hysteresis loop that has been explained in all-*d*-metal Ni-Mn-Ti Heusler alloys. Over the last seven years from the invention, Ni(Co)-Mn-Ti is the best caloric material so far. Even though this Heusler compound express outstanding multi-functional properties like large reversible MCE, large magnetoresistance and giant exchange bias elaborated in **chapter 5, 6,** and **7**, the versatile investigation on this material for the large-scale application is under lengthen field. By considering different combinations of external fields, one can think about multicaloric cooling in this system which is an emerging trend now a days. We can consider multiple responses of the system to various fields (magnetic, electric, pressure, and stress). For example, one external field is varied while other external fields are kept nonzero value, two are varied and others are zero or multiple external fields are simultaneously varied. The advantage of multicaloric materials could possibly improve the

materials properties and optimise the magnitude of those multifield external field. Therefore, all-*d*-metal Ni(Co)-Mn-Ti Heusler alloys as multicaloric cooling system will become more popular and viable with the potential to penetrate the commercial application.